Advanced Predictive Control Strategies for More Electric Aircraft

by

William D. Dunham

A dissertation submitted in partial fulfillment
of the requirements for the degree of
Doctor of Philosophy
(Aerospace Engineering)
in the University of Michigan
2019

Doctoral Committee:

Associate Professor Anouck R. Girard, Co-Chair
Professor Ilya V. Kolmanovsky, Co-Chair
Doctor Brandon Hencey, Air Force Research Laboratory
Professor Jing Sung

William D. Dunham
wdunham@umich.edu
ORCID iD: 0000-0002-5006-8041

©William D. Dunham 2019

This work is dedicated to my family and friends.

ACKNOWLEDGMENTS

Everything I've accomplished during my time at the University of Michigan was only possible due to the guidance and support of countless people, unfortunately I only have space to thank a fraction of them here.

To my advisers, Professor Ilya Kolmanovsky and Professor Anouck Girard, thank you for all that you have done for me, for passing on your insight as both researchers and teachers, and for setting an example I aspire to reach. To Professor Kolmanovsky, half a decade ago a masters student in your astrodynamics course asked to do research with you, thank you for taking a chance on me.. To Professor Girard, thank you for helping me to focus on the big picture when I got bogged down in the details and for your wit to help cut through some of the absurdities of academia.

I would also like to thank the members of my committee: Dr. Brandon Hencey and Professor Jing Sun. To Brandon, thank you for helping me in all stages of my thesis work and for your guidance and support, especially during my Summer at AFRL. To Professor Jing Sun, thank you for taking the time out of your busy schedule to review my dissertation and for your perspective on vehicle electrification.

To my lab mates, thanks for the comaraderie, advice, and occasional dinners to decompress after a long day. Dr. Chris Petersen, Dr. Greg Frey, Dominic Liao-McPherson, and Richard Sutherland thanks for the collaborations on homework and research along with the invaluable preparations for prelims, without you guys I surely would have failed. Thanks also to Dr. Robert Zidek, Nan Li, Dr. Jinwoo Seok, Huayi Li, AJ Berning, and many others. I look forward to seeing all the great things we will accomplish.

To my friends, thank you for the laughs, life advice, and fun. Thanks to those who've been with me since the start of grad school; in particular Marcel Georgin, Sarah Cusson, Malik Hassanaly, Lakshay Chauhan, and Greg Miller. Thanks also to all my friends from Maryland for giving me somewhere to recharge outside of Michigan, thanks Pat, Greg, Nate, James, Dan (both of you), Luke, Adam, Architha, and fortunately many more.

To my parents, Dr. Joan and Dr. David Dunham. Your love, support, and anecdotes from your time in grad school helped me get through some tough times. All I can says is thanks for everything.

TABLE OF CONTENTS

Dedication . . . . . **ii**

Acknowledgments . . . . . **iii**

List of Figures . . . . . **vi**

List of Tables . . . . . **xii**

List of Appendices . . . . . **xiii**

List of Abbreviations . . . . . **xiv**

Abstract . . . . . **xvi**

Chapter

1 Introduction **1**

1.1 Motivation 2
1.2 Problem Statement 5
1.3 Literature Review 6
1.4 Contributions 8
1.5 Outline 9

2 System Description and Control Problems **11**

2.1 Detailed Model 12
2.1.1 The JT9D Engine 12
2.1.2 Electrical Microgrid 16
2.2 Simplified Model 20
2.2.1 The AGTF30 Engine 21
2.2.2 Electrical Power Flow 22
2.3 Control Summary 26
2.4 Linearized Discrete-Time Models 26

3 Predictive Control Strategies for MEA Engine-Power Control **29**

3.1 Model Predictive Control 30
3.2 Rate-Based MPC 32
3.3 Coordination 34
3.3.1 Under-Actuated Engine 45
3.4 Anticipation of Power Load 48

3.5 Detailed Model Results . . . 54
3.6 Discussion . . . 59

4 Multiple Time-Scales D-MPC . . . 60

4.1 Background . . . 62
4.1.1 Privacy . . . 62
4.1.2 Interaction Rate-Based Model . . . 63
4.1.3 Multiple Time-Scales . . . 64
4.2 Centralized and Decentralized Solutions . . . 65
4.3 Multiple Time-Scales D-MPC . . . 70
4.3.1 Properties of the Algorithm . . . 76
4.4 Down-Sampled Multiple Time-Scales D-MPC . . . 78
4.5 Detailed Model . . . 86
4.5.1 Robustness to Un-coordinated Reference Changes . . . 90
4.6 Discussion . . . 94

5 Markov Chain Mission Paths and Stochastic MPC . . . 95

5.1 Scenario Based S-MPC . . . 97
5.2 Mission Profile . . . 98
5.2.1 Reference Trajectory Generation . . . 99
5.3 Simulations . . . 101
5.4 Discussion . . . 111

6 Conclusions and Future Work . . . 112

6.1 Conclusions . . . 112
6.2 Future Work . . . 113
6.2.1 Distributed Control . . . 114
6.2.2 Stochastic Control . . . 114
6.2.3 Alternative Power Architectures . . . 114
6.2.4 Alternative Propulsion Architectures . . . 114
6.2.5 Hardware Testing . . . 115

Appendices . . . 116

Bibliography . . . 122

LIST OF FIGURES

1.1 Systems and components typically considered in the electrification of aircraft designs. Image credit to [1]. . . . 3
1.2 The power pathways envisioned by MEA designs move traditionally hydraulic and bleed air driven applications onto the electrical distribution. . . . 4
1.3 Rising power loads in aircraft with each generation. Image credit to [2]. . . . 4

2.1 The Detailed model consisting of the JT9D engine, whose shafts share a geared connection with the generators of a hybrid-sourced electrical power distribution, represented as a one-line bus diagram. The key components of both subsystems are labeled. . . . 13
2.2 Actuation loop and basic circuit diagram for the CPL, as implemented in the Detailed model electrical power subsystem. . . . 16
2.3 Actuation loop and basic circuit diagram for the battery pack, as implemented in the electrical power subsystem of the Detailed model. . . . 17
2.4 Actuation loop and basic circuit diagram for the generator in the electrical power subsystem with bridge rectifiers and LC filter shown. . . . 17
2.5 The Simplified model with the AGTF30 engine and hybrid-sourced electrical power, represented as a one-line diagram, with key components labeled. The subsystems are coupled through a geared connection between the engine shafts and generators. . . . 21
2.6 Power flow representation of the electrical microgrid with components and key states labeled. . . . 23
2.7 Diagram of the Detailed model control problem with input, output, and reference signals labeled. . . . 27
2.8 Diagram of the Simplified model control problem with input, output, and reference signals labeled. . . . 27

3.1 Overview of the predictive control method. Image credit to [3]. . . . 31
3.2 Diagram of the Decentralized MPC as applied to the Simplified model of the MEA with states, references, inputs, and outputs labeled. . . . 35
3.3 Power load reference and CPL response by the Decentralized MPC on the Simplified model. . . . 37
3.4 Time history of the HVDC bus voltage responses from the Decentralized MPC on the Simplified model with the soft constrained Mil-Specs in black. . . . 37
3.5 Battery usage and state of charge resulting from the Decentralized MPC on the Simplified model. . . . 38

3.6 Time history of the split factor command from the Decentralized MPC on the Simplified model. 38
3.7 Time histories for the commanded and actual net thrust of the AGTF30 engine with the Decentralized MPC simulated on the Simplified model. 39
3.8 Results for the surge margins of the AGTF30 compressors during the Decentralized MPC run with LP constraint. 39
3.9 The time histories of the fueling rate, VAFN area, and VBV position with the Decentralized MPC simulated on the Simplified model. VAFN reference is shown as a dashed black line. 40
3.10 Power load reference and response from the Centralized MPC applied to the Simplified model. 41
3.11 Bus voltage response with the Centralized MP, the constraint is shown as black lines. 41
3.12 Time histories of the battery power and state of charge with the Centralized MPC. 42
3.13 The time history of the split factor command with the Centralized MPC on the Simplified model. 43
3.14 Time histories of the net thrust and thrust reference with the Centralized MPC simulated on the Simplified model. 43
3.15 Surge margin time histories for the engine compressor surge margins from the Centralized MPC applied to the Simplified model. 44
3.16 Engine actuation time histories from the Centralized MPC on the Simplified model. VAFN reference is shown in black. 44
3.17 Simulated results for the CPL (left) and HVDC bus voltage responses (right) from the Centralized (red) and Decentralized (blue) MPCs Simulated on the Simplified model with fixed VBV. Voltage Mil-Spec is shown in black. 46
3.18 Time histories of the battery power (top, left), battery state of charge (bottom, left), and split factor command (right) with the Centralized (red) and Decentralized (blue) MPCs on the Simplified model with fixed VBV. 46
3.19 Thrust responses from the Centralized MPC (Red) and Decentralized MPC (Blue) with the VBV locked. 46
3.20 Time histories of the compressor surge margins with the Centralized MPC (red) and Decentralized MPC (blue) on the Simplified model. 47
3.21 Engine actuations with the Centralized MPC (red) and Decentralized MPC (blue) on the Simplified model with fixed VBV. 47
3.22 Current through the PL resistor around the increase in power load request at 25 seconds for the Centralized MPC with (Red) and without (Blue) load preview on the Simplified model. The reference profile is shown as a dashed black line. 49
3.23 Current through the PL resistor around the ramped decrease in the power load request between 80 and 100 seconds for the Centralized MPC with (Red) and without (Blue) load preview on the Simplified model. The reference profile is shown as a dashed black line. 50
3.24 Time histories for the bus voltages with (red) and without (blue) anticipation of the power load, inset is a blow up of the responses between 22 and 28 seconds. The Mil-Spec constraints are shown in black. 50

3.25 Responses from the battery pack of the Simplified model with the Centralized MPC with (red) and without (blue) load anticipation. 51
3.26 Time history of the split factor commands with (red) and without (blue) anticipation of the power load in the Centralized MPC. 51
3.27 Thrust reference and simulated responses from the engine by the Centralized MPC with (red) and without (blue) load anticipation. 52
3.28 Time histories of the engine inputs from the Centralized MPC with (red) and without (blue) anticipation of the power load. 52
3.29 Surge margin time histories from the Centralized MPC with (red) and without (blue) anticipation of the power load. 52
3.30 Spread of results for the length of time power load changes are given anticipation. From left to right, top to bottom: 1 s, 0.8 s, 0.6 s, 0.4 s, 0.2 s, and no anticipation. 53
3.31 Thrust time histories from the Detailed model with the four MPC controllers. Reference given as a dashed black line. 55
3.32 Time history of the high pressure compressor surge margin responses from the MPC strategies with constraint, as applied to the Detailed model. 56
3.33 Time history of the low pressure compressor surge margin responses from the MPC strategies with constraint, as applied to the Detailed model. 56
3.34 Fuel-to-air ratio time histories with the four MPC strategies on the Detailed model. 57
3.35 Time history of the CPL responses from the MPC strategies as applied to the Detailed model. 57
3.36 Bus voltage time histories from the four MPC strategies as applied to the Detailed model. 58
3.37 Battery command time histories from the four MPC strategies as applied to the Detailed model. 58
3.38 Time histories of the generator power splits from the four MPC strategies. . . . 58

4.1 Diagram of the control approach taken in the distributed algorithms of this chapter. 63
4.2 Visualization of the multi-rate updates of the power and engine subsystems. The controllers perform an iterative consensus update at times when the coarse T_e and fine T_p steps coincide. In this example, $\kappa = 3$. 65
4.3 Simulation results for the CPL power load current (Left) and HVDC bus voltage (Right) responses from the multiple time-scales Centralized (Blue) and Decentralized (Red) MPCs on the Simplified model. 68
4.4 Time histories of the split factor command (Left) and battery responses (Right) from the multiple time-scales Centralized (Blue) and Decentralized (Red) MPCs on the simplified model. 68
4.5 Simulation results for the net engine thrust and surge margin responses from the multiple time-scales Centralized (Blue) and Decentralized (Red) MPCs on the Simplified model. The LP surge safety constraint is shown in black. 69

4.6 Histories for the engine control inputs from the multiple time-scales Centralized (Blue) and Decentralized (Red) MPCs on the Simplified model. The VAFN reference signals are omitted for clarity. 69
4.7 Simulation results for the CPL power load and HVDC bus voltage responses from the Centralized (Blue) and MT D-MPC (Red) MPCs on the Simplified model. 73
4.8 Time histories of the battery current from the four controllers on the Simplified model with upper and lower limits shown in black. 74
4.9 Split factor commands from the Centralized MPC (Blue) and MT D-MPC (Red) on the Simplified model. 74
4.10 Simulation responses for the net engine thrust and the compressor surge margins by the Centralized (Blue) and MT D-MPC (Red) MPCs on the Simplified model. 75
4.11 Engine inputs by both the Centralized (Blue) and MT D-MPC (Red) MPCs on the Simplified model. The VAFN references are omitted for clarity. 75
4.12 Time history for the number of iterations required until convergence in the MT D-MPC. 76
4.13 Visualization of matching the rate of change in an interaction between the finer time-steps of the power controller and the coarser engine controller. 80
4.14 The Simplified model power load and bus voltage responses to the DMT (b) and MT (r) D-MPCs. 81
4.15 Battery usage of the MT and DMT D-MPCs in response to the given profile. . 82
4.16 Split factor command across the four control architectures as applied to the Simplified model. 82
4.17 Thrust responses from the Simplified model as actuated by the MT (red) and DMT (blue) D-MPCs. 83
4.18 The compressor surge margin responses from the Simplified model in response to the MT (red) and DMT (blue) D-MPCs. 84
4.19 The engine control inputs from the MT (red) and DMT (blue) D-MPCs as applied to the Simplified model profile. 84
4.20 Time histories of the iterations required to reach consensus at each coordinated update by the MT (red) and DMT (blue) D-MPC algorithms. 85
4.21 Histograms of computational times per consensus update of the MT (red) and DMT (blue) D-MPC algorithms, as applied to the Simplified model. 85
4.22 Time histories of the computation times per consensus update of the MT (red) and DMT (blue) D-MPC algorithms, as applied to the Simplified model. 85
4.23 Thrust time histories from the four control strategies on the Detailed model. . . 87
4.24 The HP compressor surge margin responses from the Detailed model to all four control architectures, with constraint shown in black. 87
4.25 The FAR commands from the four MPC strategies on the Detailed model. . . . 88
4.26 The split factor commands from the four MPC strategies on the Detailed model. 88
4.27 The power load current and HVDC voltage responses from the four control strategies. The MIL-SPEC voltage constraints are given in black. 89
4.28 The battery commands from the four MPC strategies on the Detailed model. . . 89

4.29 Time history for the iterations required for convergence of the distributed algorithms applied to the Detailed model. 90
4.30 Histogram of the ADMM coordinating computation times over the simulation with average computation times for both algorithms shown as a vertical line. . 90
4.31 Time histories of the CPL of the four controllers on the Detailed model with an unexpected reference drop. The results all coincide thus appear as one signal. 91
4.32 Voltage responses of the four controllers on the Detailed model with an unexpected reference drop. 91
4.33 Battery current (Left) and generator power split factor (Right) commands from the four architectures during the reference drop case on the Detailed model. . . 92
4.34 Reference drop case responses on the engine thrust and high pressure compressor surge margin by the four controllers on the Detailed model. 92
4.35 Fuel-to-air ratio inputs from all architectures on the Detailed model with reference drop. 93
4.36 Iterations required for convergence of the D-MPC algorithms during the Detailed model reference drop case. 93

5.1 Control strategy presented in this chapter. Scenario trees are generated from the Markov chain mission model as a set of references, r^s, with associated probabilities, Π^s. The Scenario Based S-MPC optimizes for the control input, u, while accounting for the current system state, x, and the potential mission pathways. 96
5.2 The Markov chain representation of the MEA mission with states labeled and transitions shown. States within the dotted square are considered in this work and those within the solid square occur during engagement with a hostile area. 99
5.3 Illustration of a Scenario Tree generated from a discrete Markov chain with three potential transitions at the current state. The tree is then passed to the S-MPC where portions of it are considered over the horizon of the optimization problem at each time step, displayed as a box on the tree. The horizon advances one node of the tree at each controller update. 102
5.4 Mission states for the twenty seeded runs starting from state 1 (Cruise in) until having reach state 6 (Cruise Out) for two seconds. 103
5.5 Power load reference time histories from the twenty seeded mission trajectories. 103
5.6 Thrust reference realization traces from the twenty seeded mission trajectories. 104
5.7 Time histories for the CPL current for all three controllers for the examined seed on the Detailed model. 107
5.8 Bus voltage responses from all three controllers during the examined scenario on the Detailed model. 107
5.9 The thrust responses of the considered controllers during the examined seed on the Detailed model. The reference trajectory is shown as a dashed black line. 108
5.10 Low Pressure compressor surge margin response from the three controllers during the examined scenario. 108
5.11 High Pressure compressor surge margin response from the three controllers during the examined scenario. 109

5.12 Time histories of the split factor commands from the controllers during the examined scenario on the Detailed model. 109
5.13 Time histories for the battery responses from the three controllers throughout the examined case. 110
5.14 The torques applied to the shafts by the generators in response to the three controllers during the examined seed. 111

LIST OF TABLES

3.1 Review of key variables. 30
3.2 Penalties and parameters for the Centralized and Decentralized MPCs on the Simplified model. 35
3.3 Penalties and parameters for the Centralized and Decentralized MPCs on the Detailed model. 54

4.1 Key variables for Chapter 4. 64
4.2 Trajectory vector definitions over the horizon n_h used in formulating the MT D-MPC. The Δ is dropped for the interaction vectors to simplify notation. . . . 72
4.3 Parameter values for the ADMM related terms in the MT D-MPC simulation. . 73
4.4 Parameter values for the ADMM related terms in the DMT D-MPC simulation. 81
4.5 Statistical results of the timing studies done on the MT and DMT D-MPC algorithms. 83
4.6 Tunings and key parameters for the Detailed model predictive controllers. . . . 86
4.7 Parameter values for the ADMM related terms in the MT (left) and DMT (right) D-MPC strategies, as applied to the Detailed model. 86
4.8 Statistical information of the timing studies done on the distributed architectures for the Detailed model. 89

5.1 Key variables for Chapter 5. 97
5.2 Transition probabilities from current state (row) to next state (column) at transition step. 100
5.3 Dwell times enforced for transitions from previous state (row) to current state (column), in seconds. 100
5.4 Key parameters and tunings for the mission stages and the S-MPC 105
5.5 Statistical data on the tracking error RMS for the three controllers over the twenty seeded simulations. 106
5.6 Statistical data on the largest violation in response to the three controllers over the twenty seeded simulations. 106

A.1 Parameters for the Engine Subsystem. 116
A.2 Parameters for the Electrical Subsystem. 116
A.3 Parameters for the Engine Subsystem. 117
A.4 Parameters for the Electrical Subsystem. 117

LIST OF APPENDICES

A MEA Model Parameters **116**

B Linear Models **118**

LIST OF ABBREVIATIONS

ADMM Alternating Direction Method of Multipliers

AEA All Electric Aircraft

AGTF30 Advanced Geared Turbo-Fan 30,000 (AGTF30)

APU Auxiliary Power Unit

AVEM Air Vehicle Energy Management

CPL Constant Power Load

D-MPC Distributed Model Predictive Control

DARE Discrete Algebraic Ricatti Equation

DMT D-MPC Down-Sampled Multiple Time-Scales D-MPC

DoD Department of Defense

EOA Energy Optimized Aircraft

HP High Pressure

HVDC High Voltage DC

IP Intellectual Property

LP Low Pressure

LQR Linear Quadratic Regulator

MEA More Electric Aircraft

MPC Model Predictive Control

MT D-MPC Multiple Time-Scales D-MPC

NPSS Numerical Propulsion System Simulation

RMS Root Mean Square

S-MPC Stochastic Model Predictive Control

SM Surge Margin

STARC-ABL Single-aisle Turboelectric Aircraft with an Aft Boundary-Layer Propulsor

UAV Unmanned Aerial Vehicles

ABSTRACT

Next generation aircraft designs are incorporating increasingly complex electrical power distribution systems to address growing demands for larger and faster electrical power loads. This dissertation develops advanced predictive control strategies for coordinated management of the engine and power subsystems of such aircraft. To achieve greater efficiency, reliability and performance of a More Electric Aircraft (MEA) design static and dynamic interactions between its engine and power subsystems need to be accounted for and carefully handled in the control design. In the pursued approach, models of the subsystems and preview of the power loads are leveraged by predictive feedback controllers to coordinate subsystem operation and achieve improved performance of the MEA system while enforcing state and input constraints. More specifically, this dissertation contains the following key developments and contributions.

Firstly, models representing the engine and power subsystems of the MEA, including their interactions, are developed. The engine is a dual-spool turbojet that converts fuel into thrust out of the nozzle and mechanical power at the shafts. Electrical generators extract some of this power and convert it into electricity that is supplied to a High Voltage DC bus to support connected loads, with the aid of a battery pack for smoothing voltage transients. The control objective in this MEA system is to actuate the engine and power subsystem inputs to satisfy demands for thrust and electrical power while enforcing constraints on compressor surge and bus voltage deviations.

Secondly, disturbance rejection, power flow coordination, and anticipation of the changes in power loads are considered for effective MEA control. A rate-based formulation of

Model Predictive Control (MPC) allowing for offset free tracking is proposed. Centralized control is demonstrated to result in better thrust tracking performance in the presence of compressor surge constraints as compared to decentralized control. Forecast of changes in the power load allows the control to act in advance and reduce bus voltage excursions.

Thirdly, distributed MPC strategies are developed which account for subsystem privacy requirements and differences in subsystem controller update rates. This approach ensures coordination between subsystem controllers based on limited information exchange and exploits the Alternating Direction Method of Multipliers. Simulations demonstrate that the proposed approach outperforms the decentralized controller and closely matches the performance of a fully centralized solution.

Finally, a stochastic approach to load preview based on a Markov chain representation of a military aircraft mission is proposed. A scenario based MPC is then exploited to minimized expected performance cost while enforce constraints over all scenarios. Simulation based comparisons indicate that this scenario based MPC performs similarly to an idealized controller that exploits exact knowledge of the future and outperforms a controller without preview.

CHAPTER 1

Introduction

The electrification of aircraft designs has the potential for many benefits including improved energy efficiency, scalability of the power distribution, and maintainability of major components. However, these benefits will require improvements in both technology and design paradigms in order to be fully realized. A key issue is the integration and coordination of subsystems of the aircraft such as the jet engine and electrical microgrid as rising power loads impact their dynamics and interactions.

This dissertation seeks to develop coordinated and predictive control strategies for More Electric Aircraft (MEA) designs, with a focus on control of the jet engine and electrical power distribution. One requirement for the aircraft is the ability to meet key power loads such as flight surface actuations rapidly, dependably, and without violation of safety limits. Stressing mission profiles that require large, transient power load demands that can destabilize the voltage bus and high thrust levels that push the engine compressors to their stall margins are considered.

The proposed solutions in this dissertation focus on advanced predictive control frameworks. Firstly, a variant of offset free MPC that uses rate-based models is considered as it allows for linear models to be used in controlling the highly non-linear engine-power system while still achieving the goals of constraint enforcement and reference tracking. Secondly, the centralization of control is demonstrated to improve reference tracking by coordinating the variables coupling the subsystem dynamics. Thirdly, the incorporation of electrical load preview is considered to enhance control and coordination by mitigating the excitation of the negative impedance effect in the power converters. Fourthly, two distributed control solutions are formulated to ensure coordination among the subsystems by allowing local controllers to reach a consensus based on limited communication. Finally, a scenario based control strategy is demonstrated to be robust to stochastic power and thrust references generated by a mission level model.

This chapter covers the motivations for and a brief history of the development of MEA designs in Section 1.1. The scope of the problem addressed in this work is discussed in

Section 1.2. A brief survey of the relevant literature is presented in Section 1.3. The contributions of this work are summarized in Section 1.4. Finally, an outline for the remainder of the thesis is given in Section 1.5.

1.1 Motivation

Improvements in electrical distribution technologies and industry pressure to increase fuel efficiency are driving aircraft designs to become more electrified. Consequently, aircraft electrical distributions are growing in size and complexity as more flight critical components draw power from them. Advances in solid-state power electronics, electromechanical actuators, and high power-to-weight components are increasingly exploited in order to improve the energy efficiency, reliability, maintainability, and survivability of aircraft designs [4]. For example, hydraulic flight surface actuators are being replaced by electromechanical alternatives that are more efficient, eliminate the need for heavy tubing, and are easier to perform diagnostics on [5, 6]. Some components commonly included in MEA designs are labeled in Figure 1.1. Directed energy weapons (DEW) are also being considered for military aircraft and would potentially add multiple large transient power loads to the electrical distribution that could reach the megawatt range [7, 8]. Civil applications such as radar mapping of glaciers and airborne ice would also require power management considerations to function properly [9, 10].

Most of the power in an aircraft originates from the burning of fuel to drive the engines and is often supported by batteries and auxiliary power units (APUs). In conventional designs, power is transferred from the engines through mechanical connections (e.g., gear boxes and constant speed drives) and bleed air [5]. Mechanical gearing from the engine shafts drive hydraulic pumps to pressurize tubing and electrical power generators to support electrical power distribution. Hydraulically pressurized fluids are used for applications such as flight surface actuation and wheel braking, but the fluid is a potential fire hazard [11]. Bleed air is typically used for thermal operations such as environmental control and wing de-icing but comes at the cost of reduced fuel efficiency and maintenance difficulties as line punctures can be challenging to locate [12]. Lighting, communication equipment, and avionics are all powered by the electrical distribution, along with many application specific loads such as in-flight entertainment for commercial flights or targeting computers for military flights. In MEA designs, the electrification of the environmental and flight controls condenses the power pathways to the electrical generator connection, removing the need for extraction through bleed air and hydraulic pumps, see Figure 1.2. This progression to power-by-wire, in addition to the inclusion of more complex avionics and computers, is

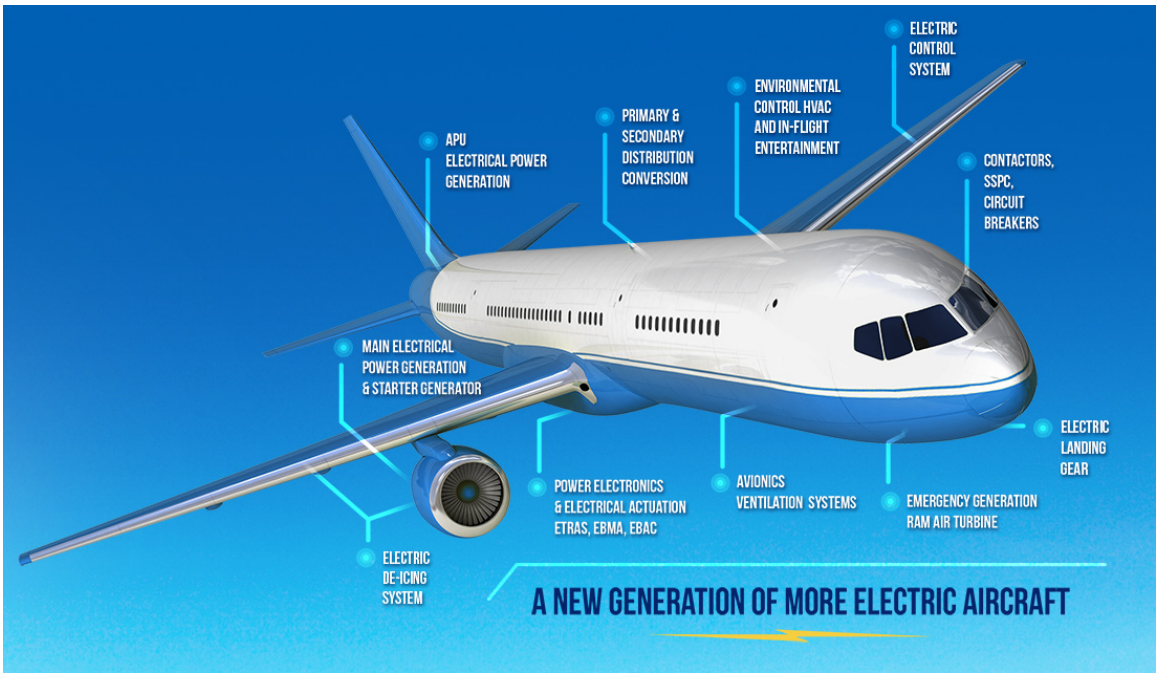

Figure 1.1: Systems and components typically considered in the electrification of aircraft designs. Image credit to [1].

pushing the power loads required to be handled by the electrical distribution to rise rapidly, a trend shown in Figure 1.3. This increase in both the power requirements of the electrical generation and the variety of power loads needed to be satisfied balloons the complexity and breadth of the electrical distribution designs while the importance of maintaining power quality to flight critical components reduces the margins for error.

These trends will not only have a substantial impact on the dynamics local to the electrical subsystem, but also on those of connected neighboring subsystems. If left unaccounted for in neighboring subsystems, these interactions can cause a loss of set-point tracking or safety constraint violations[13]. For instance, an increase in generator power production will cause a corresponding increase in the resistive torque load on the engine shaft driving it. This will slow down the shaft rotation speed, impacting the thrust produced by the engine and the surge margins of the compressors [14, 15].

Another challenge in MEA designs is the negative impedance instability inherent to solid-state power load regulation [16, 17]. Modern power electronics are designed and controlled such that the output of a digital converter is not impacted by changes in the input, so long as conditions on the input terminals are within the bandwidth of the converter. This behavior is seen as a negative impedance to the input connected electrical bus as any drop in voltage would produce a rise in current draw and vice versa. This phenomenon has a well-

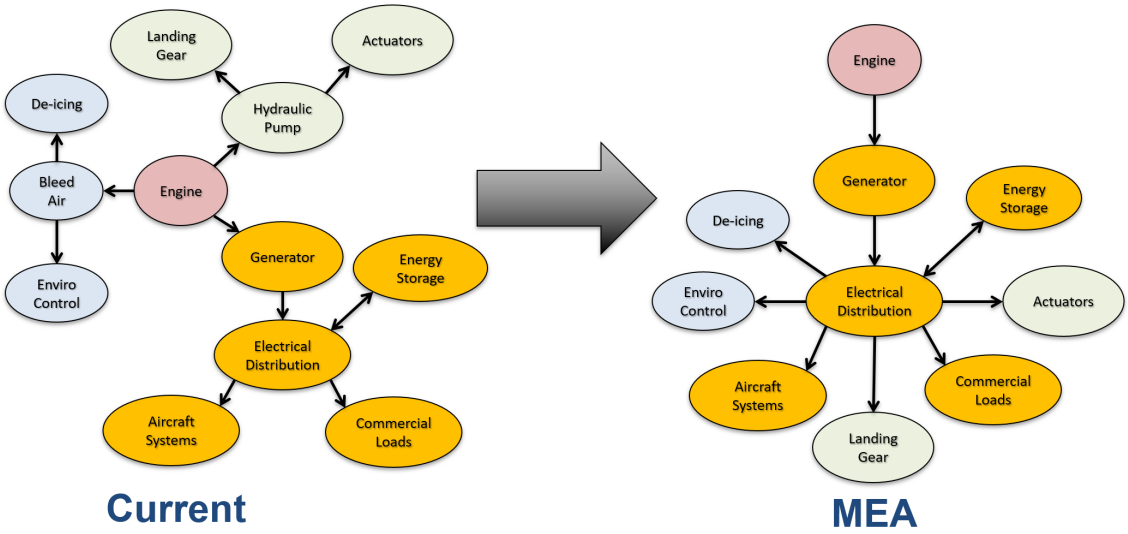

Figure 1.2: The power pathways envisioned by MEA designs move traditionally hydraulic and bleed air driven applications onto the electrical distribution.

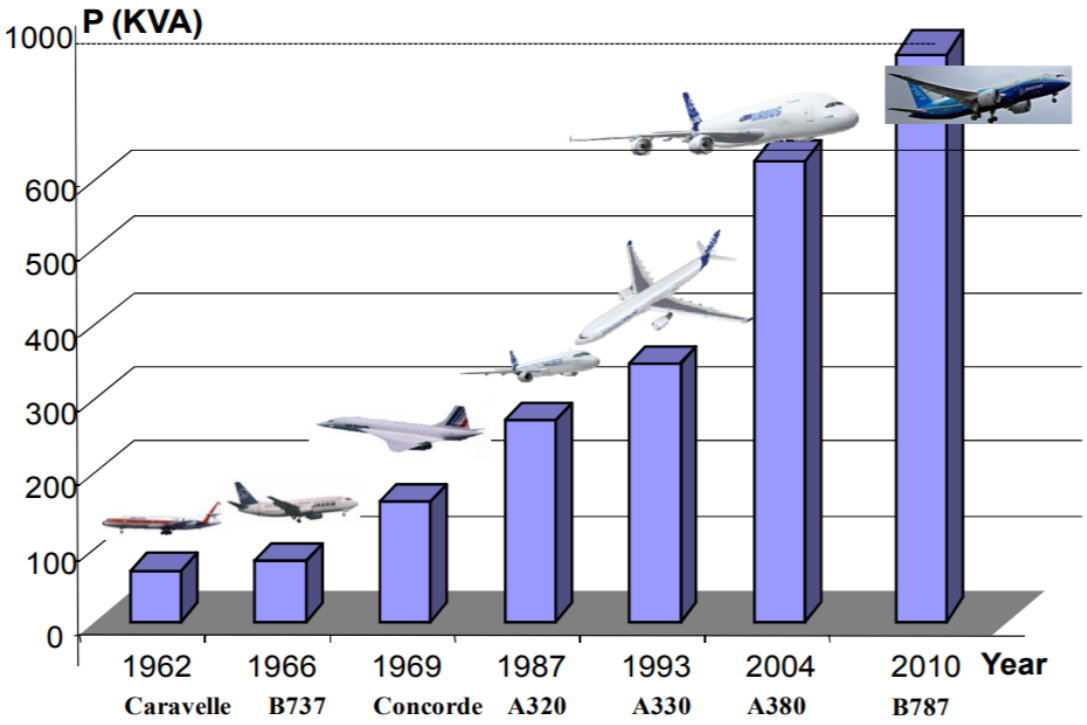

Figure 1.3: Rising power loads in aircraft with each generation. Image credit to [2].

known potential to destabilize voltage buses [18]. The low inertia of an airplane's microgrid combined with the potential for large stepped loads will require MEA control architectures to have functionality to counteract this instability [19]. One suggested solution is to use a hybrid power architecture where the bus voltage is supported by energy storage such as batteries or ultra-capacitors to smooth out fast transients while the base load is handled by slower moving generators [20]. Similar issues were considered for automotive applications in [21] where sliding mode control, feedback linearization, and large-signal phase plane analysis have been considered as potential solutions.

The complexity and scale of modern and future aircraft designs has led to the engineering process being distributed over multiple subcontractors [22]. These companies often use in house legacy tools and intellectual property (IP) for their designs and will resist efforts to integrate the process with companies that compete for similar work. This can lead to conservative and inefficient designs as rising requirements are placed on subsystems and interactions play a larger role in the system wide dynamics. Coordination is currently done in a mainly static fashion during the component sizing and requirement origination while interactions are largely treated as exogenous disturbances to be rejected by local controllers. In this work, a subsystem is defined as an element of a larger system that is operated by a single, model-based controller and is built by a single design entity. Control architectures that coordinate the evolution of the interactions during aircraft operations would alleviate the conservative use of these subsystem controllers while still allowing for privacy.

Another challenge is that the dynamics in an MEA have large differences in time-scales. For instance, the voltage and power electronics dynamical modes are on the order of milliseconds while the engine shaft rotation rates are on the order of seconds. This separation of the dynamics complicates the development of prediction-based controllers as short time steps with a long prediction horizon are required to cover the range of dynamics, increasing the number of variables required to be optimized. Hierarchical control schemes can alleviate this by stabilizing the fastest modes and allowing for predictive control to be coordinated on the slower modes.

1.2 Problem Statement

The core problem considered in this dissertation is the development of advanced predictive control strategies to enable the benefits of MEA designs. The focus is on management of the engine and electrical power subsystems as they closely interact and have dynamics that encompass a broad range of time-scales. The control objectives are summarized as:

- Leverage models of the system for optimal control,

- Track references for power loads and engine thrust,
- Exploit interactions between subsystems,
- Enforce safety constraints,
- Integrate scenario-based preview of power loads and thrust references to improve performance.

More specific requirements such as distributed control with privacy are introduced within the relevant chapters.

1.3 Literature Review

The challenges and technologies for MEA or All Electric Aircraft (AEA) have been topics of research for at least three decades [4]. Surveys of the technologies enabling MEAs along with the barriers to implementation can be found in [6], [5], and [15]. Similar electrification efforts are also occurring in marine [23, 24, 25, 26, 27] and automotive [28, 29, 30, 21] applications. However, differences inherent to the scales of these vehicles and in reliability requirements reduces the applicability of solutions between them. Ships can have far greater power requirements than aircraft but also do not have the pressure to minimize weight, allowing for some of the largest ships to have nuclear reactors and redundant power equipment available. Electric and hybrid automotive vehicles have lower power requirements than an MEA, allowing for relatively simpler power management.

Development of control strategies for mobile systems with couplings in subsystem dynamics has typically focused on the slower thermal modes. A decentralized method for controlling power flow systems motivated by thermal management is presented in [31] and [32]. The negative feedback nature of the connections between subsystems are exploited using passivity constraints in order to allow for constraint satisfaction without requiring communication. A hierarchical MPC methodology for control of thermal and electrical components using a graph based method was developed by the authors of [33, 34]. However, a top down approach was taken where the faster dynamical modes in the electrical components do not inform the slower controllers, such as the bus voltage dynamics are assumed to be static. In [35], an upper level optimization layer was incorporated, providing references to the MPC layer for fuel optimal power splitting between the two generators connected to a single turbojet engine, although voltage dynamics were not addressed.

The development of MEA architectures through modeling and experimental testing is an active area of research. The Air Force launched the Energy Optimized Aircraft (EOA)

initiative [36] that falls under a greater energy efficiency plan for its operations [37]. In support of the EOA, the Air Force Research Laboratory (AFRL) launched the Integrated Vehicle Energy Technology (INVENT) Program, with the goal of creating tools for tip-to-tail simulations of aircraft designs with a focus on thermal management [22, 38, 39]. These tools are developed with the goal of not only improving thermal management architectures and technologies but also to enable designers to improve system integration and optimization approaches. Another goal of the Air Force is to develop and implement Directed Energy Weapons (DEW) onto flight platforms, which will require improvements to power and thermal management on their aircraft [40]. AFRL initiatives have also led to methods for using fuel based cooling loops to improve aircraft thermal endurance [41, 42], studies of the stability of microgrids with hybrid power sources and controlled power loads [20, 43], designs for distributed engine control systems [44, 45], and the development of tools for analyzing power stability during large transients [46].

The National Aeronautics and Space Administration (NASA) is exploring MEA designs with the goal of improving the efficiency of commercial aircraft [47]. Specifically, NASA is examining distributed hybrid-electric propulsion configurations that have the potential to reduce emissions [48, 49]. One proposed concept is the Single-aisle Turboelectric AiRCraft - Aft Boundary Layer (STARC-ABL) [50]. The STARC-ABL design has a hybrid propulsion system with most of the thrust provided by two turbo-jet engines on the wings supplemented by a boundary layer ingesting turbo-electric propulsor at the tail. The design includes electromechanical flight actuations and electrical de-icing, removing the requirements for bleed air and hydraulic lines. Currently, ground testing of the STARC-ABL design is being done at NASA's Electric Aircraft Testbed (NEAT) [51, 52]. NASA is also working with academic and industry partners on improving electronic materials, increasing the specific weights of electrical machines, and improving integrated system testing with the long-term goal of implementing distributed electrical propulsion on commercial aircraft [53].

This thesis considers a hybrid power microgrid with electrical energy provided by generators and batteries. Other potential energy sources not considered in this work are electrical accumulators [54], fuel-cells [55], and super-capacitors [56]. These forms of energy storage have not yet reached a sufficient energy density or have characteristics that limit their applicability to aircraft microgrids. Auxiliary power units (APUs) are also common on aircraft to provide additionally power or as an engine starter but are not considered in this work.

1.4 Contributions

The methods proposed in this dissertation are potential solutions to the problem stated in Section 1.2 and a continuation of the body of literature on MEA modeling and control, summarized in Section 1.3. The specific contributions are listed below.

1. Development of MEA jet engine and electrical distribution models for control development and testing.
    - Coupling the dynamics of representations of the engine and power subsystems by mechanically connecting the shafts of the engine to the electrical generators,
    - High fidelity modeling with circuitry modeling of the microgrid and the well characterized Pratt & Whitney JT9D for the engine,
    - Fast and longer term simulations accomplished with a power flow representation of the microgrid with the AGTF30 concept engine to provide additional control inputs.
2. Identifying the components of a control strategy capable of managing the MEA engine and power system.
    - Application of rate-based MPC to achieve offset free tracking of thrust and power loads,
    - Coordination of the subsystem inputs improves the ability of the engine to track thrust references in the presence of surge margin constraints,
    - Preview of power demand dampens voltage deviations during rapid transients,
    - Hierarchical control for the power electronics to stabilize the transients that are too fast for predictive control.
3. Development of a distributed control framework for subsystems operating at differing time-scales.
    - The use of ADMM to inform the updates at the time instants when both engine and power subsystem controller jointly update and the resulting terms inform the optimization when only the power subsystem controller update,
    - Privacy of the subsystems is maintained by limiting information exchange to the interacting variables,

- The use of down-sampling for the interaction variable trajectories filters to the slowest subsystem rate, reducing the size of the vectors that need to be communicated and the computational burden on the engine controller,
- Demonstrates ability to track references, maintain constraints, and robustness to unexpected disruptions through simulation.

4. Development of a control strategy for MEA management with stochastic preview of the references.
    - Representation of an MEA mission as a Markov chain to enable the generation of scenario trees of possible reference trajectories,
    - Optimization of the MEA inputs with a Stochastic MPC that minimizes the expected value of the cost function while imposing constraints across all scenarios,
    - Simulations demonstrate that the strategy performances similarly to a controller given exact knowledge of the future and outperforms a controller given no preview.

1.5 Outline

The work is presented as follows. In Chapter 2, the MEA models common to the remainder of the thesis are presented and the basic control objectives are defined. The configuration of interest is a dual-spool turbojet engine that is dynamically connected to the generators of the electrical power distribution through a geared connection. The electrical grid is composed of the two generators, a High Voltage DC (HVDC) bus, a battery pack for energy storage, and an aggregation of the loads drawn from the bus into a Controlled Power Load (CPL). Two models are used for control demonstrations, a Simplified and Detailed model. The Simplified model uses a power flow representation of the electrical distribution to allow for rapid control iterations. The Detailed model is composed of an existing engine with high fidelity circuitry modeling of the microgrid and is more representative of a real system.

In Chapter 3, the rate-based MPC for offset free tracking using linear systems is introduced. Additionally, the impact of coordinating the control of the subsystems and anticipating the power load demands are examined through simulation. The work illustrates how coordination allows for the engine to reach otherwise infeasible thrust profiles without violating surge margin constraints through balancing the power extraction of the generators. Furthermore, anticipating the power load requests is shown to improve the controller's

ability to enforce military specifications on power quality by allowing the generators time to ramp up.

In Chapter 4, two Distributed Model Predictive Control (D-MPC) algorithms that enable subsystem controllers to achieve near optimal system-wide results while allowing for privacy considerations and differing input update rates are characterized. The interactions between the subsystems are coordinated using the Alternating Direction Method of Multipliers, that can converge on useful results in tens of iterations. The Lagrange multipliers and agreed upon trajectories produced during the consensus step allows for a fast controller to intelligently update its input in regard to what would most benefit both the local cost and that of its slower neighbor. An extension that coordinates at the slower controller time resolution reduces the communication volume required in order to reach consensus.

In Chapter 5, preview of a stochastic reference is handled. A mission to infiltrate opposition held airspace, passively collect information, survive potential encounters through countermeasures, and return to friendly airspace is considered. The stages of the mission are represented by a discrete Markov chain, which is used to generate scenario trees. A scenario based MPC uses these tree graphs representations to optimize over the scenarios considered over the prediction horizon while ensuring constraint satisfaction. Simulation results demonstrate that the controller outperforms a reactive controller and is nearly able to achieve the results of a controller given the exact future.

Finally, concluding remarks and a discussion of future avenues of research are given in Chapter 6.

CHAPTER 2

System Description and Control Problems

This chapter contains a description of the MEA configuration, representative simulation models, and the core control problem considered in this thesis. The MEA system includes dynamical interactions between the engine and power subsystems that must be considered by any solution to the control problem in order to achieve acceptable system performance with regards to tracking references on power loads and thrust while maintaining safety constraints.

The MEA configuration examined is composed of a dual-spool turbojet engine for thrust and power generation connected with a hybrid sourced microgrid for electrical power distribution. This configuration for the MEA engine-power system has been chosen as it is broadly representative of many military and civilian applications. The jet engine is a high-bypass dual-spool design, common in modern commercial and military applications. The electrical microgrid is composed of two generators, a High Voltage DC (HVDC) bus, a battery pack for energy storage, and a Controlled Power Load (CPL) that represents all loads drawn from the bus. A geared connection between the engine shafts and the electrical generators couples the dynamics of the electrical and propulsion subsystems.

Two models are used for simulating the MEA, a Detailed model and a Simplified model, that share a similar overall architecture but differing systems. The two models incorporate differing engines and level of fidelity with which the electrical components are simulated. The Detailed model, previously used in [13, 57, 58], demonstrates the controllers' ability to handle the complex dynamics within a more realistic system. The Simplified model has been introduced to reduce the simulation run-time that allows for rapid evaluations of the impact of control design variations while also being easier to analyze and a concept engine that includes additional inputs for the controller. The parameters for the models are given in Appendix A. The development of these two models and different considerations reflected a natural progression of this research. A detailed back-to-back comparison of the Detailed and Simplified approaches for the same system configuration is left to future research.

The remainder of this chapter is laid out as follows. The Detailed model composed of a JT9D engine and electrical circuitry is described in Section 2.1 including dynamics, inputs available for actuation, imposed constraints, and tracking references. Section 2.2 describes the AGTF30 engine and power flow dynamics, inputs, tracked outputs, and constraints composing the Simplified model. The control problems for each model are described in Section 2.3 along with illustrating diagrams. Finally, linearized models for control development are described in Section 2.4.

2.1 Detailed Model

The Detailed model was developed in collaboration with the State Awareness and Real Time Response group at the Air Force Research Laboratory in Dayton, Ohio to support the testing of control algorithms for the MEA engine-power system. The model captures a high level of fidelity in the simulation of the engine and power components using commercially available modeling software.

The engine is modeled off the Pratt & Whitney JT9D, a well known turbofan engine with a long service history [59]. The power distribution is modeled at the circuit level, providing realistic simulations down to the time-scales of converter switching. Figure 2.1 provides an overview of the Detailed model with the major components and connections shown.

2.1.1 The JT9D Engine

The Pratt & Whitney JT9D is a dual-spool turbojet engine that first entered into service in 1970 on the Boeing 747 [59]. The engine was chosen to be included in this model as it represents a generic commercial sized jet engine and has publicly available models. The engine produces the power extracted by the electrical generators and the thrust that drives the aircraft.

The two spools of the engine are identified by the state of the air worked by their components as the low pressure (LP) and high pressure (HP) spools. The LP spool contains the fan facing the incoming air flow, and the low pressure stage compressor and turbine, with the HP spool between the latter two. The HP spool has the high pressure stage compressor at the front end and high pressure turbine at the back end, with the burner placed between them. The HP spool shaft is a hollow cylinder with the LP shaft rotating freely within that space. The JT9D is a high-bypass engine with the majority of the air flow bypassing the engine at a ratio of 5 pounds for every pound of air passing through the core. Past the fan,

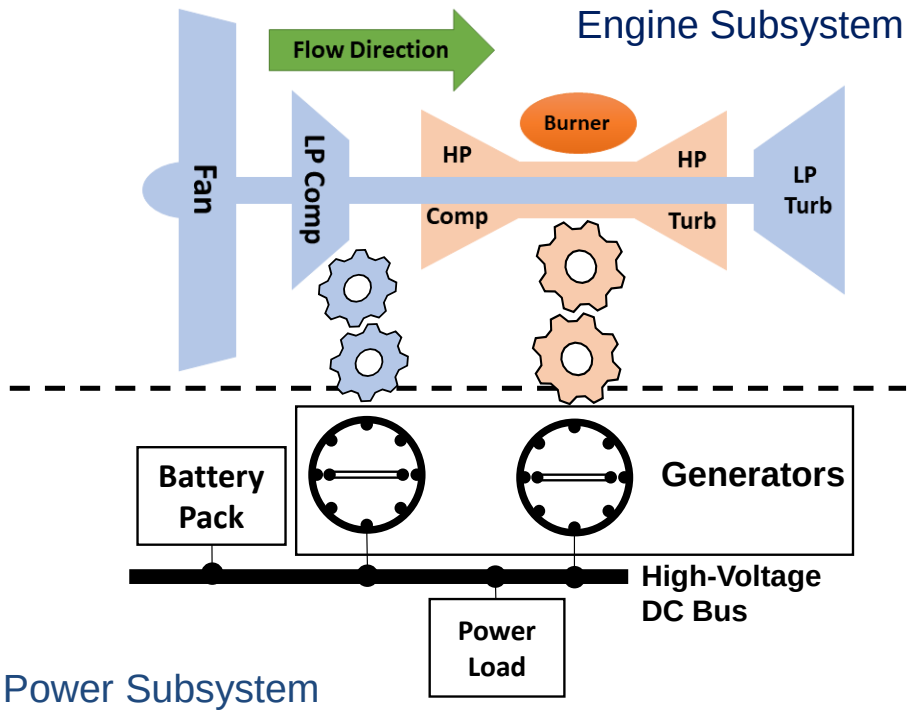

Figure 2.1: The Detailed model consisting of the JT9D engine, whose shafts share a geared connection with the generators of a hybrid-sourced electrical power distribution, represented as a one-line bus diagram. The key components of both subsystems are labeled.

the engine air flow is compressed by the LP then HP stage compressors. Fuel is injected into the stream and ignited in the burner. Some of the energy from this thermodynamic expansion is harvested by the HP and LP turbines to drive the compressors and any geared connections to their shafts. The air then passes through the outlet and the net difference in pressure between the inlet and outlet flows produces the aircraft's thrust. The flow direction and elements of the engine are illustrated in Figure 2.1.

The model of the JT9D engine used in this thesis is based on NASA's T-MATS toolbox JT9D example, with some modifications to allow for generator torque loads to be passed to the shaft dynamics [60]. T-MATS is an open source toolbox for the modeling of thermodynamic systems with a focus on aero-thermal applications in Simulink [61]. The gas dynamics within T-MATS are considered static as they are much faster than the mechanical dynamics of the engine shafts. Look up tables for the compressors and turbines use the pressure ratio across the element, mass flow rate of the gas, and shaft rotation rate to determine the gas characteristics at the element boundaries. The flow error between the element and the incoming flow is driven to zero by an iterative solver that adjusts the R-line value of each compressor or turbine, see [61] for more details. This approach is similar to the

one used in other simulation packages such as Numerical Propulsion System Simulation (NPSS) [62].

The dynamics of the shaft rotation rates evolve according to the following differential equations,

$$\dot{\omega}_{HP} J_{HP} = -\tau_{HP}^{gen} - \tau_{HP}^{comp} + \tau_{HP}^{turb}, \tag{2.1}$$

and

$$\dot{\omega}_{LP} J_{LP} = -\tau_{LP}^{gen} - \tau_{LP}^{fan} - \tau_{LP}^{comp} + \tau_{LP}^{turb}, \tag{2.2}$$

where ω is the shaft speed with the subscript designating the shaft, J is the moment of inertia of the shaft, and τ denotes a torque load. The superscript on the torque designates the component applying the load. The shaft speeds are driven by the turbine torques and in turn provides mechanical power to the fan, compressors, and generators. The compressor and turbine torques are found using T-MATS elements and are functions of both the shaft speeds and gas flow characteristics while the generator torques originate from the electrical subsystem, described below. The adjustment of the lower level elements such as vane angles is scheduled and incorporated into the compressor and turbine tables. The gas flow characteristics depend nonlinearly on the ambient air conditions (Mach number, altitude, and temperature) and the fuel-to-air ratio (FAR) fed to the burner. As vehicle dynamics are not considered in this work, the ambient air conditions are kept static throughout the simulations.

The input manipulated at the predictive control level for the engine is the FAR, $u_e = u_{FAR}$. The generator torques are considered to be the interaction variables, $x_{ep} = [\tau_{HP}^{gen}\ \tau_{LP}^{gen}]^T$, where the subscript ep denotes that these torques are inputs to the engine, subsystem e, and originate from the electrical power distribution, subsystem p. Note that in the remainder of this dissertation the "gen" superscript is dropped when referring to the torques created by the generators; this simplifies the notation as the other torque values are not of concern. The dynamics of the engine can be written as

$$\dot{x}_e = f_e(x_e, u_e, x_{ep}), \tag{2.3}$$

where x_e is a vector of the states of the subsystem and the function f_e may depend on additional parameters such as ambient air pressure and temperature. The only reference tracked at the MPC level is thrust, $r_e = [r_{thr}]$, and is assumed to originate from a path planner or pilot request. The outputs of the engine, $y_e = [y_{thr}\ y_{HP,SM}\ y_{LP,SM}]^T$, are thrust, and the surge margins of the HP and LP compressors, respectively, and are used for reference tracking and constraint enforcement. These are non-linear functions of the state

of the engine and the input,

$$y_e = g_e(x_e, u_e, ambient\ air), \tag{2.4}$$

and they also depend on parameters such as ambient air pressure and temperature. The interactions originating from the engine are the rotation rates of the shafts,

$$x_{pe} = [\omega_{HP},\ \omega_{LP}]^T = h_{pe}(x_e, u_e). \tag{2.5}$$

Thus, the engine dynamics can be modeled as the system of equations in (2.3), (2.4), and (2.5).

The control design must consider constraints on both the inputs and outputs of the engine. The FAR has physical constraints on how fast the fuel pumps can ramp up or down and is mathematically expressed as

$$\Delta \underline{u}_e \leq \Delta u_e \leq \Delta \bar{u}_e, \tag{2.6}$$

where $\Delta u_e = u_e(t) - u_e(t - \Delta t)$ is the change of u_e over a time-step of Δt. The FAR actuation also has physical limits on the maximum and minimum values it can take,

$$\underline{u}_e \leq u_e \leq \bar{u}_e, \tag{2.7}$$

In this work, these limits on the FAR are treated as constant while in implementation they would derive from the air flow and the capabilities of the fuel injection pumps, thus would vary based on the flight conditions. The surge margins on the outputs are constrained as

$$c_{j,SM} \leq y_{j,SM}, \quad j = [HP,\ LP], \tag{2.8}$$

where $c_{j,SM}$ are the minimum surge margins to be maintained, in order to prevent compressor surge. As T-MATS uses 0D modeling and static flow assumptions, it is possible that some of the faster modes in the turbomachinery are neglected, thus the constraints in (2.8) are chosen to be conservative and are soft constrained to allow for short deviations. The above constraints can be expressed in set notation as

$$\Delta u_e \in \mathcal{D}_e, \quad u_e \in \mathcal{U}_e, \text{ and } y_e \in \mathcal{Y}_e. \tag{2.9}$$

Further discussion and an overview of the JT9D control problem are given in Section 2.3.

2.1.2 Electrical Microgrid

The microgrid of the MEA extracts the electrical power from the engine shafts and distributes it throughout the aircraft. The microgrid is composed of a high voltage DC (HVDC) bus, two synchronous generators, a battery pack, and the power loads drawing from the bus; a line diagram is given in Figure 2.1.

In the Detailed model, the generators are modeled as three-phase synchronous machines and provide the base load handling in the aircraft. The batteries are modeled as XALT Energy's 63 Ah High Power Superior Lithium Ion Cells [63] with a two-capacitance equivalent representation and can either provide or draw power from the bus. The batteries can ramp power at a faster rate than the generators and are used to smooth out the impact on the voltage dynamics of large changes in the power loads while the generators ramp up. The power loads drawn from the bus are modeled as an equivalent lumped constant power load (CPL). A CPL is a circuit that regulates the input draw in order to maintain a power set point, typically by solid-state converters. Stepped or rapidly rising power loads of primary interest in this work as they induce destabilizing negative impedance characteristics in the bus due to the regulation of the output to a desired power being much faster than the ramp rates of generators or most batteries. The converters regulating the CPL and the battery pack are represented by average-value models in circuit form, as in [64].

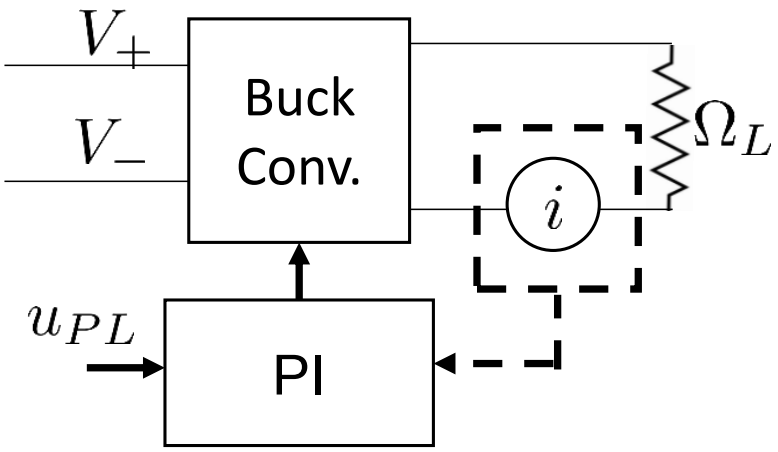

Figure 2.2: Actuation loop and basic circuit diagram for the CPL, as implemented in the Detailed model electrical power subsystem.

The electrical circuitry is simulated using PC Krause and Associates' Automated State

Machine Generation (ASMG) toolbox for Simulink. ASMG is a simulation package that builds state equations of circuits of arbitrary complexity based on the topology of the circuit [65]. The CPL is modeled as a resistor with the current through it regulated by a DC-DC Buck converter with the input connected to the HVDC bus. The duty cycle of the converter is controlled by a proportional-integral (PI) loop that drives the power in the CPL to the command from the higher level controller, u_{PL}, as shown in Figure 2.2. The battery pack is simulated as a two-capacitance equivalent representation that includes internal voltage dynamics, state of charge, and temperature effects [66]. The command for battery power, u_{Batt}, is treated similarly as the CPL regulation, a PI loop tracks for a current flow to the voltage bus, as shown in Figure 2.3.

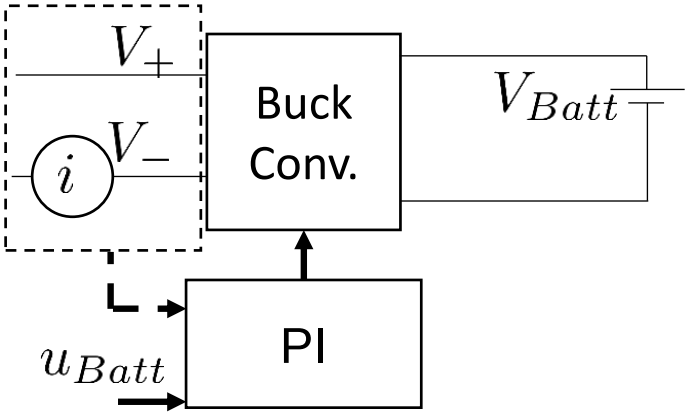

Figure 2.3: Actuation loop and basic circuit diagram for the battery pack, as implemented in the electrical power subsystem of the Detailed model.

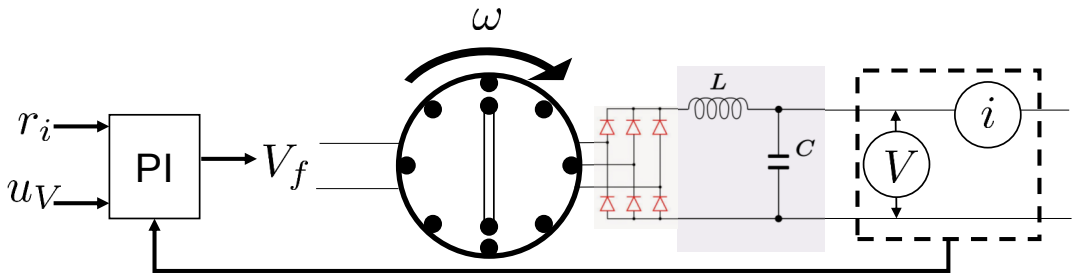

Figure 2.4: Actuation loop and basic circuit diagram for the generator in the electrical power subsystem with bridge rectifiers and LC filter shown.

The synchronous machine generators are modeled using the dynamical equations from

[67] that include winding and stator inductance dynamics. The AC electrical current of the generators is passed through a rectifier to convert it to DC power, then through a low-pass L-C filter to the HVDC bus to reduce the voltage ripple. The generator inputs are the rotation rates of the shafts attached to them, $\omega_{HP/LP}$, and the field winding voltage, V_f. A schematic of the generator low-level control loop and the major components are shown in Figure 2.4. The power out of each generator is a non-linear function of those inputs,

$$P_{Gen} = f(\omega, V_f). \tag{2.10}$$

The generators have two control objectives within the electrical architecture: 1) to regulate the HVDC bus voltage to the specified voltage command, u_V, and 2) to regulate the ratio of the power draw from the engine to match an MPC split command, u_{sp}. The power output of each generator, as measured after its filter, is $P_{Gen,m} = V_{HVDC} I_m,\ m \in \{HP,\ LP\}$, the bus voltage times the current through the filter. Both generators provide power to the same bus, thus the voltage at the outputs are shared and thus the current through the filter is regulated in order to control the power output of each generator. The power split command u_{sp} takes values between zero and one; at one, all generator power originates from the HP shaft connected generator, at zero, all generator power originates from the LP shaft. The total generator power to the bus is then

$$P_{Gen,tot} = P_{Gen,HP} + P_{Gen,LP} = V_{HVDC}(I_{HP} + I_{LP}), \tag{2.11}$$

that, with the definition of u_{sp}, leads to

$$P_{Gen,HP} = u_{sp} P_{Gen,tot}, \quad P_{Gen,LP} = (1 - u_{sp}) P_{Gen,tot}. \tag{2.12}$$

Dividing the right hand sides by V_{HVDC} and substituting with (2.11) gives the references for the current for each generator as

$$r_{I,HP} = u_{sp}(I_{HP} + I_{LP}), \tag{2.13}$$

$$r_{I,LP} = (1 - u_{sp})(I_{HP} + I_{LP}). \tag{2.14}$$

The field voltage that excites the generators are then regulated through the PI loops

$$V_{f,j} = K_{prop,V}(u_V - y_{HVDC}) + K_{int,V}\int_0^t (u_V(s) - y_{HVDC}(s))ds + \\ K_{prop,I}(r_{I,j} - I_j) + K_{int,I}\int_0^t (r_{I,j}(s) - I_j(s))ds, \tag{2.15}$$

where $j \in \{HP,\ LP\}$ denotes the generator, $K_{prop,V/I}$ is the proportional gain, and $K_{int,V/I}$ is the integral gain. The rotational rates of the shafts driving the generators are the interactions coming into the power subsystem, $x_{pe} = [\omega_{HP}\ \omega_{LP}]^T$.

The outputs from the power subsystem that are used by a higher level controller for regulation and constraint enforcement, $y_p = [y_{HVDC},\ y_{PL}]$, are the bus voltage and the power load, respectively. The bus voltage is constrained to follow an extrapolation of the Mil Spec MIL-STD-704F [68] out to 540 V,

$$500\ V \leq y_{HVDC} \leq 560V, \tag{2.16}$$

with deviations of that to the range of 400-660 V allowed for less than 0.01 seconds. This is enforced as a soft constraint with slack variables that are highly penalized, allowing for short deviations. The constraints on the power subsystem can be represented compactly in the set notation as

$$y_p \in \mathcal{Y}_p, \tag{2.17}$$

where $y_p = [y_{PL},\ y_{HVDC}]$.

The local dynamics of the electrical power subsystem are modeled as a set of nonlinear equations

$$\dot{x}_p = f_p(x_p, u_p, x_{pe}), \tag{2.18}$$

and its outputs as

$$y_p = g_p(x_p, u_p), \tag{2.19}$$

where the components of the vector, x_p, are the local states of the power subsystem. The electrical power subsystem impacts the engine dynamics through the torques, modeled by the following relation

$$x_{ep} = h_{ep}(x_p, u_p). \tag{2.20}$$

In the following chapter, MPC design is considered that manipulates the voltage, split factor, power load, and battery commands to the lower level actuation loops,
$u_p = [u_V,\ u_{sp},\ u_{PL},\ u_{Batt}]^T$. The power subsystem has references given for the power load and bus voltage, $r_p = [r_{PL},\ r_V]^T$. These are assumed to be generated by a load

scheduler and pilot requests. Additionally, the inputs are rate-constrained as

$$\Delta u_p \in \mathcal{D}_p, \tag{2.21}$$

in order to prevent exciting higher order dynamics in the solid state converters and voltage dynamics. Limits are also imposed on the inputs to account for the maximum power flow achievable by the battery pack,

$$c_{Batt,min} \leq u_{Batt} \leq c_{Batt,max}, \tag{2.22}$$

and to prevent any generator from having zero load,

$$0.2 \leq u_{sp} \leq 0.8, \tag{2.23}$$

as that can cause power to back flow and damage the rectifier diodes or generator windings. This is expressed mathematically as

$$u_p \in \mathcal{U}_p. \tag{2.24}$$

The control problem for the electrical power subsystem is summarized in Section 2.3.

2.2 Simplified Model

The Simplified model was developed to abstract the dynamics of the electrical components to the time-scales of the higher level MPC-based controller. In particular, the electrical distribution is simply modeled as a power flow. This allows for faster simulation and prediction times at the cost of fidelity. Additionally, the choice of the Advanced Geared Turbo-Fan 30,000 (AGTF30), a concept engine, makes this system more representative of the capabilities of future aircraft. The AGTF30 engine has more inputs than the JT9D, allowing for comparison of cases with under-actuation by blocking one input. As a natural progression of this research, the case of the AGTF30 engine has become of interest for which the Simplified model has been implemented. The development of a power flow electrical subsystem for the JT9D engine is left to future research and publications. An illustration of the Simplified model is given in Figure 2.5.

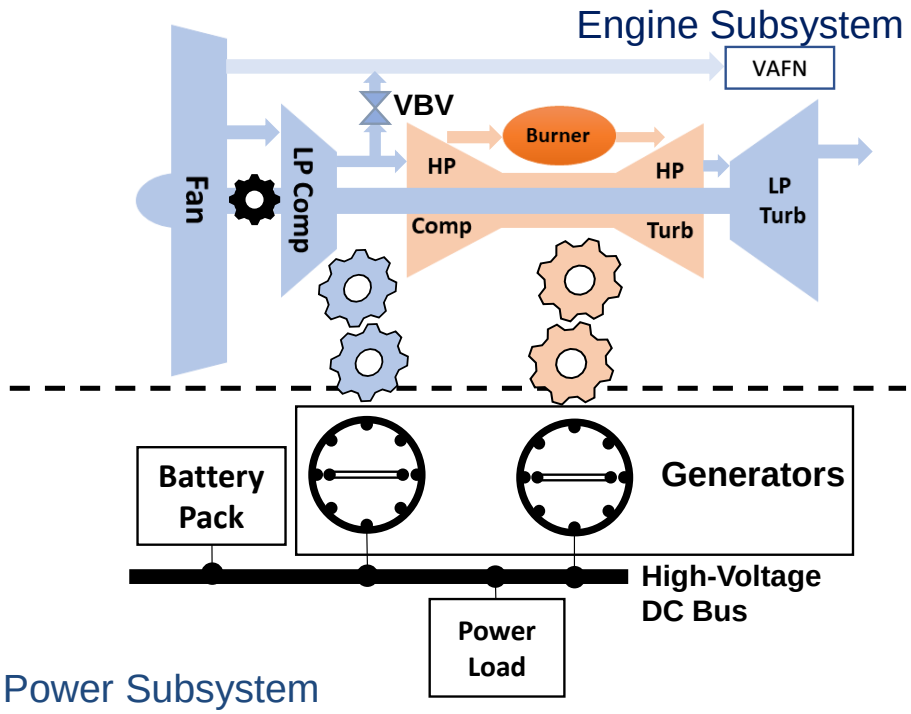

Figure 2.5: The Simplified model with the AGTF30 engine and hybrid-sourced electrical power, represented as a one-line diagram, with key components labeled. The subsystems are coupled through a geared connection between the engine shafts and generators.

2.2.1 The AGTF30 Engine

The AGTF30 used for the engine of the Simplified model is a concept designed by NASA for a 30,000 lbf thrust class engine [69]. It is a smaller dual-spool jet engine than the JT9D, which is rated between 45,000 and 56,000 lbf thrust at sea level. The AGTF30 is an ultra high-bypass engine with a bypass ratio of 20 pounds to 1 pound of worked air. The fan of the engine is connected to the LP shaft through a geared connection, spinning it slower than the LP shaft rotation rate. The AGTF30 also features a variable bleed valve (VBV) after the LP compressor and a variable area fan nozzle (VAFN). These components can be seen in Figure 2.5.

The shaft dynamics of the AGTF30 are the same as in equations (2.1) and (2.2), but the components along the shafts follow different maps. The VAFN impacts the operating point of the fan by impacting the pressure of the fan nozzle with the purpose of keeping the fan at its optimal efficiency. Decreasing the nozzle area increases the pressure behind the fan by choking the air flow while increasing the area decreases the pressure. A look up table based on the Mach number of the ambient flow and the LP shaft speed determines the

optimal VAFN position with respect to the fan operating point, as

$$v_{VAFN} = l(MN, \omega_{LP}), \tag{2.25}$$

where MN is the Mach number, and the table is adapted from [69]. The VBV releases air from the exit of the LP compressor to the engine bypass stream in order to increase the stall margin of that component by reducing its back-end pressure, impacting the pressure ratio. Opening the VBV releases some of the worked air and decreases the efficiency of the overall engine. As such, it is desirable for the VBV to follow the input reference of $v_{VBV} = 0$ as much as is possible.

The MPC level inputs for the AGTF30 are $u_e = [u_{Wf},\ u_{VAFN},\ u_{VBV}]^T$, where u_{Wf} is actuated in pounds per second (pps) instead of the FAR as in the JT9D. First order actuator dynamics and input lag are included in the model. The outputs of the AGTF30 tracked for regulation and constraint enforcement are $y_e = [y_{thr},\ y_{SM,HP},\ y_{SM,LP}]^T$, and the incoming interactions from the electrical distribution are $x_{ep} = [\tau_{HP},\ \tau_{LP}]^T$. The references to be tracked are $r_e = [r_{thr},\ v_{VAFN},\ v_{VBV}]^T$. The inputs are all box constrained as $u_e \in \mathcal{U}_e$ and rate constrained as $\Delta u_e \in \mathcal{D}_e$. Surge margin constraints are imposed to prevent stall as $y_e \in \mathcal{Y}_e$, as was done for the Detailed model engine. The control problem for the AGTF30 is discussed in Section 2.3.

2.2.2 Electrical Power Flow

In the Detailed model, the circuitry of an electrical microgrid is simulated in ASMG. That level of fidelity allows for more realistic simulations but much of the low level dynamics, such as converter switching, is far too fast for predictive controllers that update in discrete time to consider. The Simplified model abstracts this microgrid into a series of directed power flows whose modes are closer in time scale to the controller. The power flow graph with the components, states, inputs, and outputs is shown in Figure 2.6. Power flow modeling of electrical components takes many forms but is a well established practice [70] and has previously been done for MEA modeling [71], although at slower time-scales than of concern here. These simpler dynamics allow for faster simulation times that enables quicker control iterations.

Each node in the graph in Figure 2.6 represents a component within the electrical subsystem, each having one or two states. The edges are channels that power can flow through and are assumed to be regulated connections. Starting from the end point of the model and working back, the CPL is again represented by a resistor connected to the voltage bus with

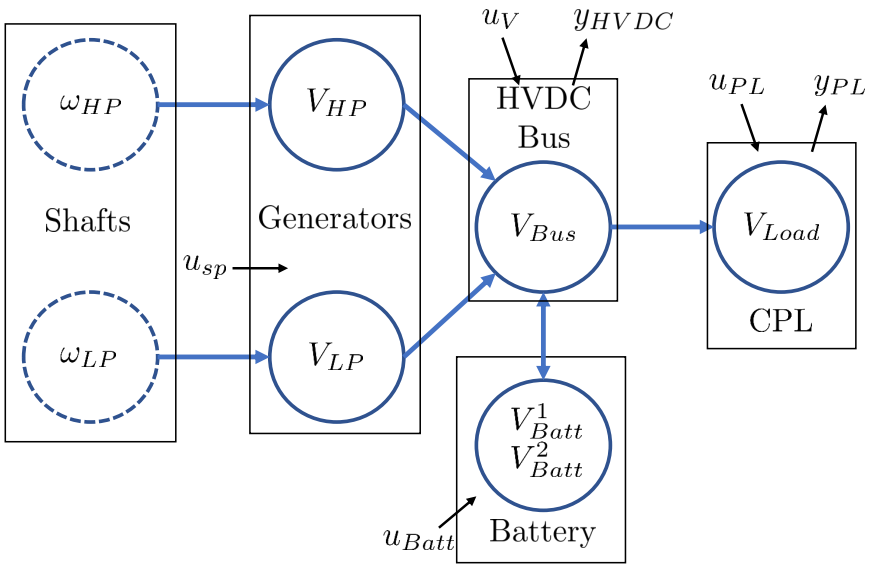

Figure 2.6: Power flow representation of the electrical microgrid with components and key states labeled.

a buck converter. The buck converters are modeled as second-order a transfer function,

$$H_{conv}(s) = \frac{D}{1 + s\frac{L}{R} + s^2 LC}, \tag{2.26}$$

where D is defined here as the duty cycle of the converter, R as the power load resistor, L as the converter inductance, and C its capacitance. An integrating feedback loop regulates the duty cycle for the CPL as

$$\dot{D} = K_{load}\left(u_{PL} - \frac{V^2_{Load}}{R}\right). \tag{2.27}$$

The HVDC bus is the nexus for all the power flows in the model. The HVDC voltage dynamics are described as a capacitance, using

$$C_{Bus}\dot{V}_{Bus} = P_{HP,Gen} + P_{LP,Gen} - P_{Load} + P_{Batt,} \tag{2.28}$$

where C_{Bus} is the bus capacitance, $P_{HP/LP,Gen}$ are the power flows coming from the two generators, and P_{Batt} is the battery power flow to or from the bus. The power flow from

the generators to the voltage bus follows the relation

$$P_{j,Gen} = u_{j,GenPwr}(\alpha_{Gen} V_j + \beta_{Gen} V_{Bus}), \quad j \in \{HP,\ LP\}, \tag{2.29}$$

where α_{Gen}/β_{Gen} are constants whose ratio is proportional to that of a transformer between the generators and the bus, and V_j is the jth generator output voltages. This encompasses the power flow from the output of the generators through any rectification and filtering before connecting the bus through a converter. The converter actuation is $u_{j,GenPwr}$ and is controlled by a PI loop with the commanded power split as

$$u_{HP,GenPwr} = \tilde{u}_{GenPwr} u_{sp}, \quad u_{LP,GenPwr} = \tilde{u}_{GenPwr}(1 - u_{sp}), \tag{2.30}$$

where u_{sp} is the MPC generator power split command, the total generator draw command is

$$\tilde{u}_{GenPwr} = K_{V,p}(u_V - V_{Bus}) + K_{V,I} \int_0^t (u_V(s) - V_{bus}(s))ds, \tag{2.31}$$

and u_V is the MPC HVDC bus voltage command.

The battery pack is modeled with an OCV-RC-RC equivalent circuit, as described in [72]. This representation has two states for the fast and slow modes, both with RC pair dynamics and described by

$$\dot{V}^1_{Batt} = \frac{1}{C_1} i_{Batt} - \frac{1}{R_1 C_1} V^1_{Batt}, \tag{2.32}$$

$$\dot{V}^2_{Batt} = \frac{1}{C_2} i_{Batt} - \frac{1}{R_2 C_2} V^2_{Batt}. \tag{2.33}$$

The output voltage is then described as

$$V^{out}_{Batt} = V_{OCV} - V^1_{Batt} - V^2_{Batt} - i_{Batt} R_{Batt}, \tag{2.34}$$

with the open circuit voltage V_{OCV} being a function of the current state of charge and R_{Batt} being the internal resistance of the battery. The terms $R_{1/2}$ and $C_{1/2}$ vary with the state of charge as described in [72]. The current drawn from the battery terminals is regulated by the feedback loop

$$\dot{i}_{Batt} = K_{Batt}(u_{Batt} - V^{out}_{Batt} i_{Batt}). \tag{2.35}$$

The battery power onto the bus is

$$P_{Batt} = V^{out}_{Batt} i_{Batt}. \tag{2.36}$$

The generators follow the dynamics

$$C_{Gen}\dot{V}_j = P_{in,j} - P_{j,Gen}, \quad j \in \{HP,\ LP\}, \tag{2.37}$$

where the term C_{Gen} is a time-constant for the dynamics of the generator and not an energy storage capacitance. The power flow into the generator is given by

$$P_{in,j} = u_j(\alpha_{Shaft}\omega_j + \beta_{Shaft}V_j),\ j \in \{HP,\ LP\}, \tag{2.38}$$

the engagement of the generator through the field winding voltage is u_j and is actuated by a PI loop to regulate the generator output voltage to a nominal value as

$$u_j = K_{prop}(V_{ref,gen} - V_j) + K_{int}\int_0^t (V_{ref,gen}(s) - V_j(s))ds\ j \in \{HP,\ LP\}. \tag{2.39}$$

The coefficients α_{Shaft} and β_{Shaft} describe the input power flow based on the connected shaft speed and generator voltage, respectively. The internal voltage of the jth generator, V_j, can be thought of as the engagement of that generator and the capacitance, C_{Gen}, determines the transient generator dynamics. The capacitance of the generator can be represented by limiting the regulation term $u_j,\ j \in \{HP,\ LP\}$, but this is not done in this work. The torque load created by each generator follows a simple efficiency relationship during the conversion from mechanical power to electrical as

$$\tau_j = \frac{P_{in,j}}{\omega_j \eta_{gen}},\ j \in \{HP,\ LP\}, \tag{2.40}$$

where η_{gen} is the efficiency of each generator.

The predictive controller manipulates the power flow subsystem through the inputs $u_p = [u_V,\ u_{sp},\ u_{Batt},\ u_{PL}]^T$. The outputs that need to track higher level commands are $y_p = [y_{PL},\ y_V]^T$ and represent the actual power loads and voltages, in order to track the reference signal $r_p = [r_{PL},\ r_V]^T$, and maintain constraints on the bus voltage, as described in the specification for aircraft power quality MIL-STD-704F [68]. As for the Detailed model, constraints imposed on the voltage are softly held with highly penalized slack variables. Constraints on the inputs are intended to keep the system within a physically reasonable operating range, e.g., a split factor of greater than 1 or less than zero would have the generators acting as motors and driving the engine shafts. Rate limits on the inputs mitigate excitation in the system from the converters. The control problem is further discussed in the following section.

2.3 Control Summary

The control problem for the Detailed model is visualized in Figure 2.7 and for the Simplified model in Figure 2.8. The controller objective is to use the inputs $u = [u_e^T,\ u_p^T]^T$, subject to the constraint set $u \in \mathcal{U} = \mathcal{U}_e \times \mathcal{U}_p$ and rate constraint set $\Delta u \in \mathcal{D} = \mathcal{D}_e \times \mathcal{D}_p$, such that the system outputs $y = [y_e^T,\ y_p^T]^T$ are within the constraint set $y \in \mathcal{Y} = \mathcal{Y}_e \times \mathcal{Y}_p$ and the references $r = [r_e^T,\ r_p^T]^T$ are tracked by their corresponding outputs. If the subsystems are coordinated, then the dynamical impacts of the interactions, reflected through the variables x_{ep} and x_{pe}, must be accounted for.

The control problems formulated for the Detailed and Simplified models, are similar in their goals but have certain distinct characteristics. The Detailed model has the same number of control inputs and outputs only if the subsystems are coordinating; otherwise, the JT9D engine is under actuated when the surge margin constraints are active. The Simplified model has more inputs than outputs, due to the VBV and VAFN actuators, and these extra degrees of freedom can be exploited to increase the efficiency of the engine. This can be handled in various ways such as prescribing extra set-points for these inputs following efficiency maps based on the current system state.

2.4 Linearized Discrete-Time Models

The development of MPC solutions in subsequent chapters will be based on using linearized discrete-time models for prediction that leads to a constrained quadratic problem (QP) that needs to be solved online to generate the control action. The linearized models for the Detailed model subsystems were found using the system identification toolbox for MATLAB. The linearized model for the Simplified model engine were found with a linearization tool included with T-MATS [61] that employs a perturbation method. The Simplified electrical power linearized model were found using linear filter fittings for the voltage and power load dynamics, while the torque outputs were found by analytically solving for Equation (2.40). All of these models introduce inaccuracies into the prediction model that impact the performance of the controllers. Chapter 3 introduces the rate-based MPC framework to mitigate the steady state disturbances caused by these modeling errors, circumventing the need for more accurate prediction models.

The models are discretized with a zero-order hold over a time-step of T such that $t = kT$. This leads to the discrete-time equations

$$\delta x_i(k+1) = A_i \delta x_i(k) + B_i \delta u_i(k) + W_{ij} \delta x_{ij}(k), \tag{2.41}$$

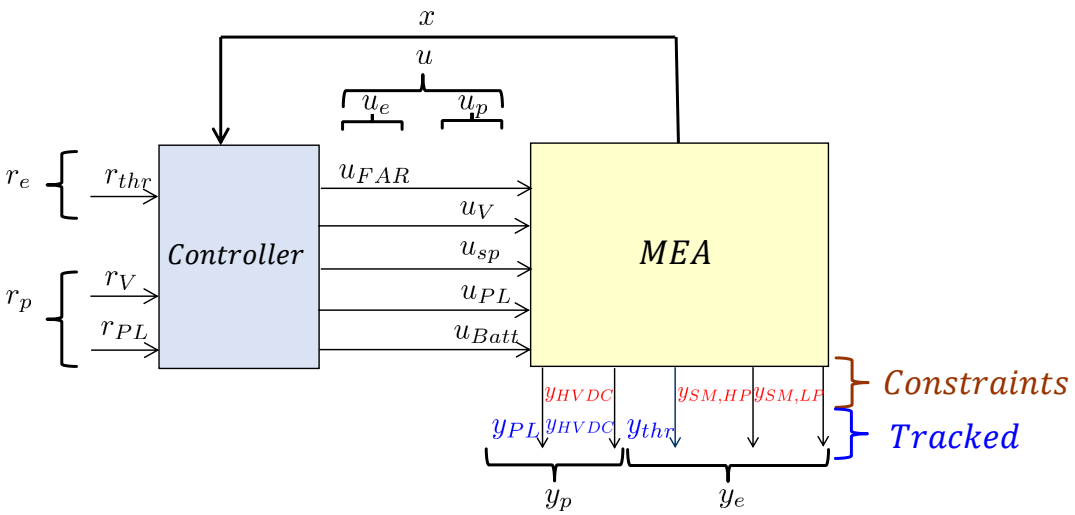

Figure 2.7: Diagram of the Detailed model control problem with input, output, and reference signals labeled.

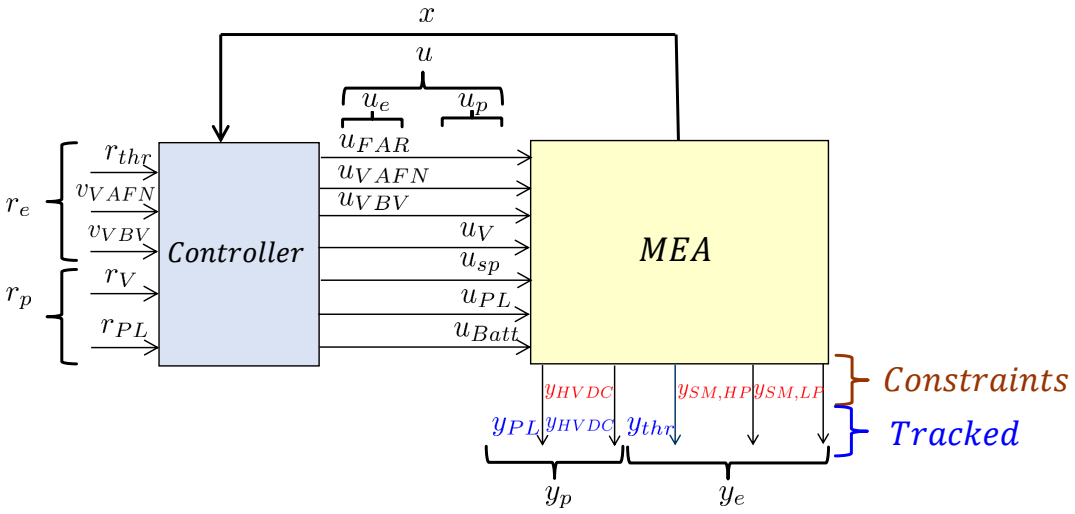

Figure 2.8: Diagram of the Simplified model control problem with input, output, and reference signals labeled.

$$\delta y_i(k) = C_i \delta x_i(k) + D_i \delta u_i(k), \tag{2.42}$$

$$\delta x_{ji}(k) = E_{ji} \delta x_i(k) + F_{ji} \delta u_i(k), \tag{2.43}$$

where (x_i^*, u_i^*) denote equilibrium values at which the linearization is performed, $\delta x_i(k) = x_i(k) - x_i^*$ is the offset from the equilibrium state, $\delta u_i(k) = u_i(k) - u_i^*$ is the input offset, $\delta y_i(k) = y_i(k) - g_i(x_i^*, u_i^*)$ is the output offset, and $\delta x_{ij}(k) = x_{ij}(k) - h_i(x_i^*, u_i^*)$ represents the interaction variable offset. The point that is chosen as the equilibrium is during cruise-flight conditions, with constant thrust and power loads.

Equations (2.41), (2.42), and (2.43) describe a distributed model of the MEA. An aggregated model of the whole system takes the form,

$$\delta x(k+1) = A \delta x(k) + B \delta u(k), \tag{2.44}$$

and

$$\delta y(k) = C \delta x(k) + D \delta u(k), \tag{2.45}$$

where

$$\delta x(k) = \begin{bmatrix} \delta x_e(k) \\ \delta x_p(k) \end{bmatrix}, \ \delta u(k) = \begin{bmatrix} \delta u_e(k) \\ \delta u_p(k) \end{bmatrix}, \ \delta y(k) = \begin{bmatrix} \delta y_e(k) \\ \delta y_p(k) \end{bmatrix}, \tag{2.46}$$

$$A = \begin{bmatrix} A_e & W_{ep} E_{ep} \\ W_{pe} E_{pe} & A_p \end{bmatrix}, \quad B = \begin{bmatrix} B_e & W_{ep} F_{ep} \\ W_{pe} F_{pe} & B_p \end{bmatrix}, \quad C = \begin{bmatrix} C_e & \mathbf{0} \\ \mathbf{0} & C_p \end{bmatrix}, \tag{2.47}$$

$$D = \begin{bmatrix} D_e & \mathbf{0} \\ \mathbf{0} & DC_p \end{bmatrix},$$

and $\mathbf{0}$ is a matrix of zeros of appropriate size. With these models, predictive controllers can be formulated. The numerical values for the linearized models are given in Appendix B.

CHAPTER 3

Predictive Control Strategies for MEA Engine-Power Control

This chapter introduces strategies that, together, can effectively manage the engine and power subsystems of the MEA. These strategies are disturbance rejection to handle model mismatch error, coordination to account for subsystem interactions, and anticipation of changes in the power load demand to dampen voltage transients. They enable offset free tracking of references while enforcing key system state constraints. These strategies are identified through simulation as the components of an effective controller, given full system feedback, authority over all subsystem inputs, and foresight of the future power loads.

Rate-based MPC is able to achieve offset free tracking by leveraging a velocity form of prediction that can account for constant or slowly varying disturbances [73]. In application to MEA engine and power control, this allows the usage of simple linear models for prediction on the nonlinear engine and power system as the integral action helps overcome the mismatch between the predicted and actual dynamics. Additional literature on rate-based and offset free MPC strategies can be found in [74, 75, 76, 77, 78, 79].

Coordination of the interactions between the engine and power subsystems of the MEA improves tracking of references and constraint enforcement. Coordination of the generator power draw from the engine through a centralized controller is able to improve thrust tracking in the presence of surge margin constraints by providing additional inputs to the subsystem. However, centralizing control can be computationally more expensive and would require more coordination in the design process, thus this chapter seeks to demonstrate the benefits that make coordination desirable.

The negative impedance characteristic of the solid-state regulation of the power load leads to instabilities in the bus voltage. These can be mitigated by rate-limiting the power load command, but would lead to a delay in meeting requests that may not be acceptable, e.g. actuation of flight surfaces during take off. Anticipation of the power loads in the prediction horizon enables the controller to act in advance and diminish bus voltage transients.

The reference profiles given to the controllers for simulation on the MEA models discussed in the previous chapter contain high thrust and power loads with rapid transients, designed to stress the bus voltage and engine compressors. This tests the abilities of the control strategies to account for the interactions between the subsystems while having to enforce constraints on the compressor surge and bus voltage. The profiles are not grounded in a particular scenario but could represent a military aircraft required to perform evasive high-thrust turns while using DEW shots or a hybrid-propulsion craft accelerating through both a jet engine and electric motors.

This chapter is laid out as follows. The basics of MPC are discussed in Section 3.1 and rate-based MPC in Section 3.2. Simulations on the Simplified model are used to examine the benefits of coordination of the MEA subsystems in Section 3.3 and of load anticipation in Section 3.4. The control strategies are then demonstrated on the Detailed model in Section 3.5. A discussion of the results is given in Section 3.6.

3.1 Model Predictive Control

Model Predictive Control (MPC) leverages a discrete-time prediction model of the system for the optimization of a sequence of control inputs over a finite horizon subject to the imposed input and output constraints. The feedback control law is then defined by the first element of the optimized control sequence. Specifically, the MPC exploits the model in order to predict the response over a finite horizon of n_h discrete steps, T seconds apart, into the future in order to determine the optimal control trajectory that minimizes a cost function subject to constraints. A large body of literature exists on MPC and many variations of it have been made since its inception. Reference [73] provides a good introduction.

A basic formulation of MPC as it applies to the MEA problem described in Section 2.3 is given as

Table 3.1: Review of key variables.

Variable	Description
x	States of the system
u	Inputs of the system
y	Outputs of the system
r	System references

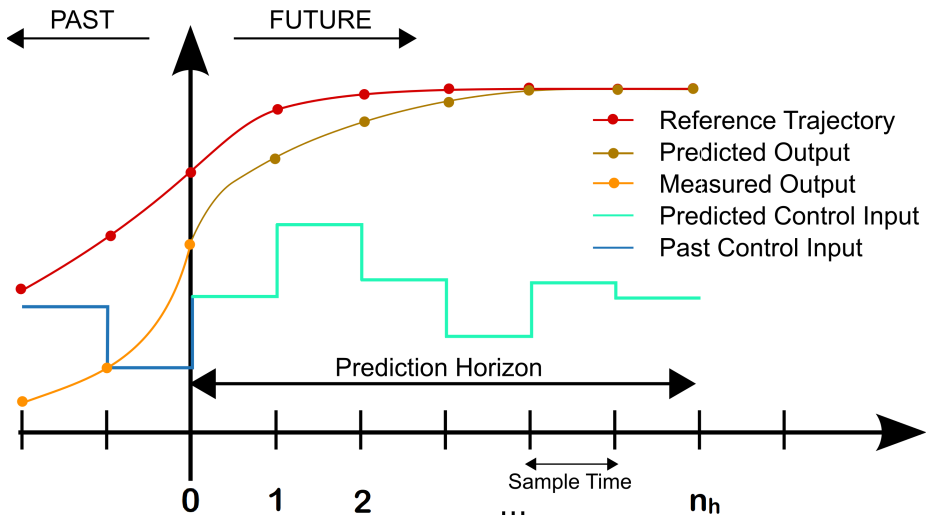

Figure 3.1: Overview of the predictive control method. Image credit to [3].

$$\min_{u} \sum_{k=0}^{n_h-1} [(y(k)-r)^T Q(y(k)-r) + \delta u^T(k) R \delta u(k)] + (y(n_h)-r)^T P(y(n_h)-r), \tag{3.1}$$

$$\begin{aligned} \text{subject to } & \delta x(k+1) = A\delta x(k) + B\delta u(k), \\ & y(k) = C\delta x(k) + D\delta u(k) + y^*, \\ & \Delta u(k) \in \mathcal{D}, \\ & u(k) \in \mathcal{U}, \\ & y(k) \in \mathcal{Y}, \\ & \delta x(0) = x(t) - x^*. \end{aligned}$$

The point (x^*, u^*) is the equilibrium point about which the system is linearized and y^* is the corresponding output. The matrices Q and R are symmetric positive-definite and penalize deviations from the tracked references and corresponding equilibrium input values. The matrix P is positive-definite and is typically set to the unique solution of the Discrete Algebraic Ricatti Equation (DARE), that, under the assumption of no active constraints near the set-point, ensures local closed-loop stability [80]. A review of the key variable definitions is given in Table 3.1.

The standard MPC formulation given in (3.1) may not guarantee zero steady-state output tracking error in the presence of disturbances such as model mismatch. Augmentation for disturbance rejection is required to achieve offset free tracking in the MEA engine-power system.

3.2 Rate-Based MPC

The mismatch between the nonlinear system dynamics and the linear predictive models, if unaccounted for, can degrade tracking and constraint handling. The rate-based MPC has been shown to reduce the impact of model mismatch [81, 82] and was previously used for MEA engine-power control in [13, 83, 57].

The vector $\bar{x}(k) = [\Delta x^T(k)\ e^T(k)\ y^T(k)\ u^T(k)]^T$ is defined as the extended rate-based model state vector, where the rate of change in the state is defined as

$$\Delta x(k) = x(k) - x(k-1), \tag{3.2}$$

the instantaneous tracking error is defined as

$$e(k) = y(k) - r(k), \tag{3.3}$$

the control rate of change is defined as

$$\Delta u(k) = u(k) - u(k-1), \tag{3.4}$$

and, for a constant reference, r, it follows that

$$\begin{aligned} \Delta x(k+1) &= x(k+1) - x(k) \\ &= A(x(k) - x(k-1)) + B(u(k) - u(k-1)) \\ &= A\Delta x(k) + B\Delta u(k), \end{aligned} \tag{3.5}$$

the error evolves as

$$\begin{aligned} e(k+1) &= Cx(k+1) + Du(k+1) - r \\ &= C(\Delta x(k) + x(k)) + D(\Delta u(k) + u(k)) - r \\ &= C\Delta x(k) + D\Delta u(k) + Cx(k) + Du(k) - r \\ &= C\Delta x(k) + D\Delta u(k) + y(k) - r \\ &= C\Delta x(k) + D\Delta u(k) + e(k), \end{aligned} \tag{3.6}$$

and the output changes as

$$\begin{aligned} y(k+1) &= Cx(k+1) + Du(k+1) \\ &= C(\Delta x(k) + x(k)) + D(\Delta u(k) + u(k)) \\ &= C\Delta x(k) + D\Delta u(k) + Cx(k) + Du(k) \\ &= C\Delta x(k) + D\Delta u(k) + y(k). \end{aligned} \tag{3.7}$$

The rate-based dynamics can then be represented by the mathematical model

$$\bar{x}(k+1) = \bar{A}\bar{x}(k) + \bar{B}\Delta u(k), \tag{3.8}$$

where

$$\bar{A} = \begin{bmatrix} A & \mathbf{0} & \mathbf{0} & \mathbf{0} \\ C & I & \mathbf{0} & \mathbf{0} \\ C & \mathbf{0} & I & \mathbf{0} \\ \mathbf{0} & \mathbf{0} & \mathbf{0} & I \end{bmatrix}, \quad \text{and} \quad \bar{B} = \begin{bmatrix} B \\ D \\ D \\ I \end{bmatrix}. \tag{3.9}$$

With the rate-based model specified, a quadratic cost function is defined over a horizon of n_h steps as

$$J(\Delta u, \bar{x}) = \sum_{k=0}^{n_h-1} \left[\bar{x}^T(k) Q \bar{x}(k) + \Delta u^T(k) R \Delta u(k)\right] + \bar{x}^T(n_h) P \bar{x}(n_h). \tag{3.10}$$

The extended state stage penalty, Q, is a positive semi-definite matrix,

$$Q = \begin{bmatrix} Q_{\Delta x} & \mathbf{0} & \mathbf{0} & \mathbf{0} \\ \mathbf{0} & Q_e & \mathbf{0} & \mathbf{0} \\ \mathbf{0} & \mathbf{0} & Q_y & \mathbf{0} \\ \mathbf{0} & \mathbf{0} & \mathbf{0} & Q_u \end{bmatrix}, \tag{3.11}$$

and the input stage cost R matrix is positive definite. The penalties $Q_{\Delta x}$, Q_y, and Q_u are typically set to zero but can be used to dampen the state change rate or track nominal outputs and inputs, which may be desirable in some situations. The DARE for the extended system (3.8)-(3.11) typically has no solution due to a lack of stabilizability; however, for the dynamics of Δx and e, with only the cost corresponding to those states in (3.11), the DARE typically has a solution, $\tilde{P}$. The terminal penalty in (3.10) is then set to

$$P = \begin{bmatrix} \tilde{P} & \mathbf{0} \\ \mathbf{0} & \mathbf{0} \end{bmatrix}. \tag{3.12}$$

If the problem is unconstrained or constraints are inactive near the set-point, the resulting MPC feedback law coincides with the LQR feedback law for the model representing the evolution of Δx and e; this guarantees zero steady-state offset error, i.e., $e(k) \to 0$ as $k \to \infty$ for constant or slowly varying references [73]. This property will also be maintained under constant additive disturbances to the system dynamics. The velocity form of rate-based MPC defined here requires that the pairs (A, C) and $\left(\begin{bmatrix} \mathbf{0} & \mathbf{0} \\ \mathbf{0} & Q_e \end{bmatrix}, \begin{bmatrix} A & \mathbf{0} \\ C & I \end{bmatrix} \right)$ are detectable, the pair $(\bar{A}, \bar{B})$ to be stabilizable, and an accurate measurement of the tracking error e in order to achieve offset free tracking of the references [77, 84].

The rate-based MPC problem can then be stated as

$$\begin{aligned} \min_{\Delta u} \; & J(\Delta u, \bar{x}), \\ \text{subject to } \bar{x}(k+1) = & \bar{A}\bar{x}(k) + \bar{B}\Delta u(k), \\ & \Delta u(k) \in \mathcal{D}, \\ & u(k) \in \mathcal{U}, \\ & y(k) \in \mathcal{Y}, \\ & \text{given } x(0),\ u(-1). \end{aligned} \tag{3.13}$$

The MPC feedback law is now defined by the first element of the control sequence $\Delta u^*(k)$ that optimizes (3.13) as

$$\Delta u^{MPC}(\Delta x(0), e(0), y(0), u(0)) = \Delta u^*(0). \tag{3.14}$$

3.3 Coordination

To demonstrate the benefits of coordination for control of the engine-power system and capabilities of the rate-based MPC in meeting the control objectives, two controllers are simulated on the Simplified model. The first controller simulated is a Decentralized rate-based MPC, where the subsystem controllers are not aware of their impacts on each other and do not communicate. A schematic of the Decentralized MPC, as applied to the MEA system, is shown in Figure 3.2. Then a Centralized MPC, previously shown in Figure 2.8, is simulated and the results are compared against the Decentralized solution to demonstrate the improvement. The Decentralized MPC would be computationally less burdensome than the Centralized MPC but, without consideration for the interactions, would have worse performance. The Centralized MPC represents the best possible solution that can be achieved

given the linear prediction models, constraints, and cost functions but requires that one controller has authority over both subsystem inputs, is given state feedback from both subsystems, and has a prediction model for the entire system. The controllers use the same tunings for their Q and R weights, as presented in Table 3.2, and the constraints on the inputs, input rates, and outputs are in Appendix A.

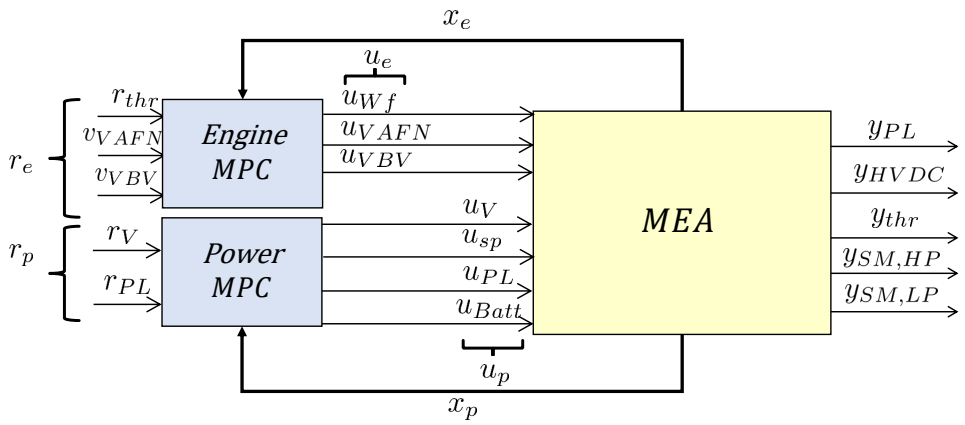

Figure 3.2: Diagram of the Decentralized MPC as applied to the Simplified model of the MEA with states, references, inputs, and outputs labeled.

Table 3.2: Penalties and parameters for the Centralized and Decentralized MPCs on the Simplified model.

Variable	Description	Value	Variable	Description	Value
T	Controller time step	0.1 s	n_h	Horizon length	10 (1 s)
Q_{thr}	Thrust penalty	10^{-3}	Q_{VAFN}	VAFN penalty	10^{-2}
Q_{VBV}	VBV penalty	50	R_{Wf}	Wf change penalty	5×10^5
R_{VAFN}	VAFN penalty	0.01	R_{VBV}	VBV change penalty	5×10^4
Q_{PL}	PL penalty	0.1	Q_V	Voltage penalty	0.1
Q_{Batt}	Battery use penalty	10^{-8}	R_{PL}	PL change penalty	1
R_V	Voltage ref penalty	100	R_{sp}	Split ref penalty	10^4
R_{Batt}	Battery ref penalty	10^{-6}			

The rate-based Decentralized MPC for the engine, e, and electrical power, p, subsystems is defined by the solution of two independent problems,

$$\begin{aligned} &\min_{\Delta u_i} J_i(\Delta u_i, \bar{x}_i), \\ \text{subject to } \bar{x}_i(k+1) =& \bar{A}_i \bar{x}_i(k) + \bar{B}_i \Delta u_i(k), \\ & \Delta u_i(k) \in \mathcal{D}_i, \\ & u_i(k) \in \mathcal{U}_i, \\ & y_i(k) \in \mathcal{Y}_i, \\ & \text{given } x_i(0),\ u_i(-1), \end{aligned} \tag{3.15}$$

where the subscript $i \in \{e,\ p\}$ denotes that the models and constraints for the local subsystem dynamics in Equations (2.41) and (2.42) are used for prediction in Problem (3.15).

Tuning was done by adjusting the penalties of the Decentralized MPC controllers. The costs were then centralized by a weighted summation as

$$J = \alpha_e J_e + \alpha_p J_p, \tag{3.16}$$

where $\alpha_e,\ \alpha_p \in \mathbb{R}^+$ and the relative value of each is changed until the desired emphasis is placed on the objectives of each subsystem. The penalties reported in this work are scaled by the α terms.

The Decentralized MPC is simulated on the Simplified model and the results are presented in Figures 3.3-3.9. The controller is not active until 10 seconds into the simulation. Here and elsewhere in this chapter the MPC optimization problem is solved by MATLAB's quadprog.m QP solver.

The power load reference and CPL response to the Decentralized MPC are shown in Figure 3.3, where the controller is shown to be capable of following the reference despite a large increase at 25 seconds from 100 kW to 1 MW, and drop with ramp back down to 199 kW at 80 seconds. The bus voltage in Figure 3.4 violates the Mil-Spec constraints at the times of the stepped power load changes. This violation is attributed to model mismatch. In the next section, load anticipation is shown to be effective at enforcing the voltage constraint. Output constraints are implemented as soft so that the optimization problem is solvable even if no feasible solution exists. This also accounts for the short deviations of the voltage range allowed by Mil-Spec, as discussed in Section 2.1.2.

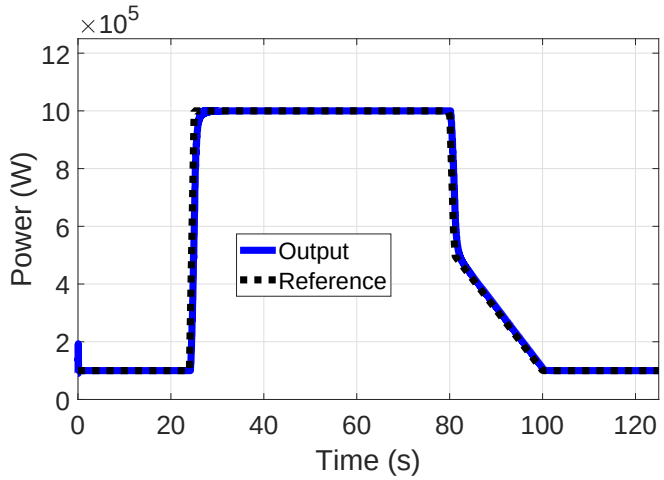

Figure 3.3: Power load reference and CPL response by the Decentralized MPC on the Simplified model.

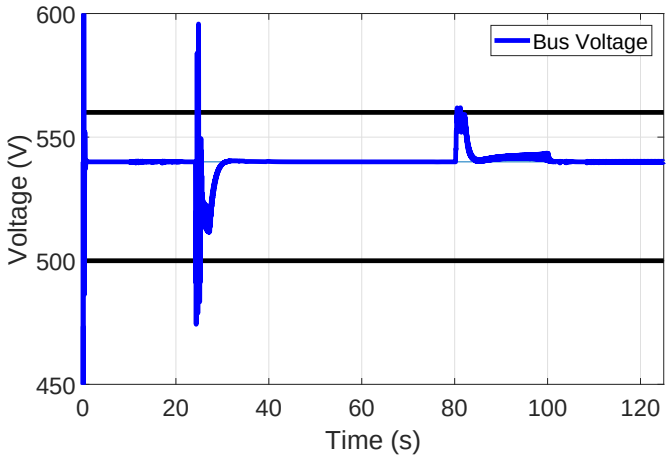

Figure 3.4: Time history of the HVDC bus voltage responses from the Decentralized MPC on the Simplified model with the soft constrained Mil-Specs in black.

The battery pack results in Figure 3.5 demonstrate how the energy storage is used to mitigate the voltage deviations by adding power to the bus when the power load is rising and drawing from it when the power load is dropping. The split factor in Figure 3.6 barely moves from its initial starting point of a 50-50 power balance between the two generators, without coordination the Decentralized MPC has no incentive to change the power split.

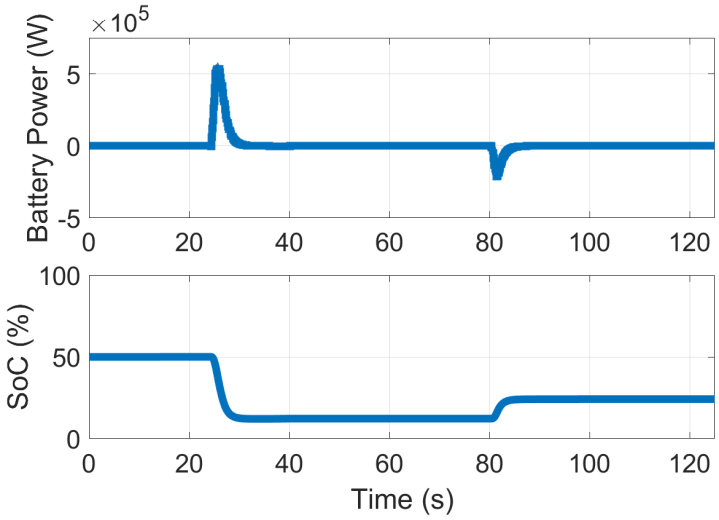

Figure 3.5: Battery usage and state of charge resulting from the Decentralized MPC on the Simplified model.

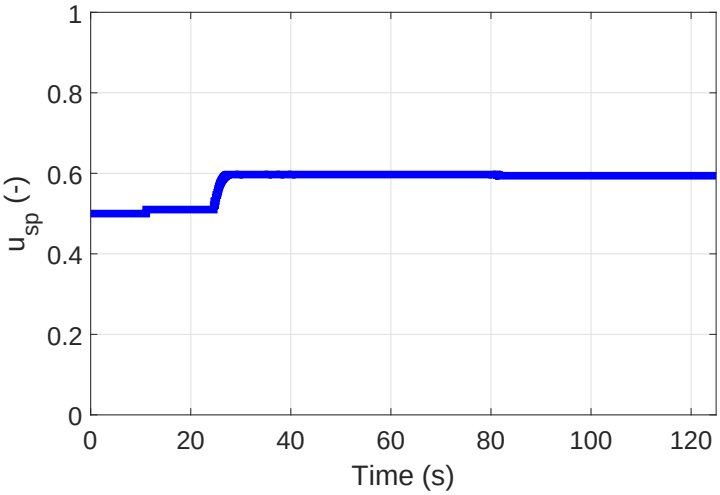

Figure 3.6: Time history of the split factor command from the Decentralized MPC on the Simplified model.

The engine responses are given in Figures 3.7-3.9. Figure 3.7 shows that the Decentralized controller is able to follow the thrust reference closely, despite the ramp up in requested thrust in the time interval between 25 to 60 seconds and ramp down in the interval of 75 to 90 seconds. There is a momentary loss in tracking during the power load transient at 25 seconds and a similar bump followed by a constant offset at 80 seconds to 90 seconds. This suggests that the unaccounted for torque loads imposed by the electrical generators degrade the Decentralized controller performance, but that it is able to rapidly recover. The time histories of the surge margins of the compressors in Figure 3.8 show that the Low

Pressure compressor surge margin (LP SM) is at its safety limit throughout the simulation, excepting for before the controller initialization at t=10 seconds and briefly at 25 and 80 seconds. Note that the initial condition has the LP surge start below the constraint before the controller becomes active at 10 seconds. The High Pressure (HP) compressor surge is also held to the safety limit of 15%, but the constraint is never active and is not shown in the figure.

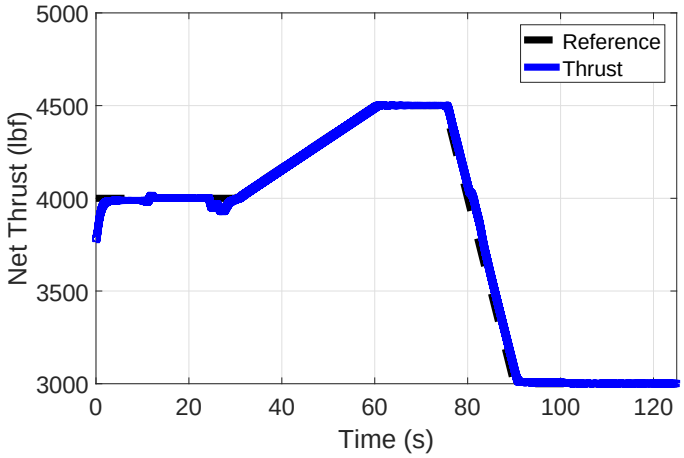

Figure 3.7: Time histories for the commanded and actual net thrust of the AGTF30 engine with the Decentralized MPC simulated on the Simplified model.

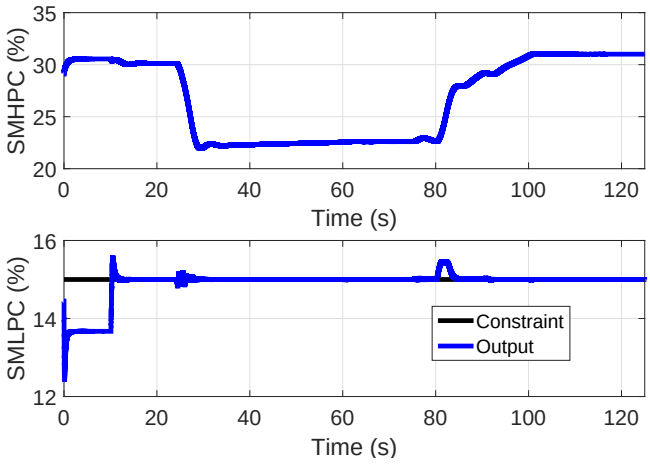

Figure 3.8: Results for the surge margins of the AGTF30 compressors during the Decentralized MPC run with LP constraint.

The plots of the engine inputs in Figure 3.9 shows that the Variable Area Fan Nozzle (VAFN) is able to track the desired trajectory and that the Variable Bleed Valve (VBV) opens as soon as the Decentralized MPC becomes active at 10 seconds, helping the LP

surge constrain in Figure 3.8, the VBV then rises to near 10% open for the remainder of the simulation. The VBV cannot close any further as the LP constraint is active for the majority of the simulation, except for the transient at 80 seconds when both the power load and thrust references are backing off.

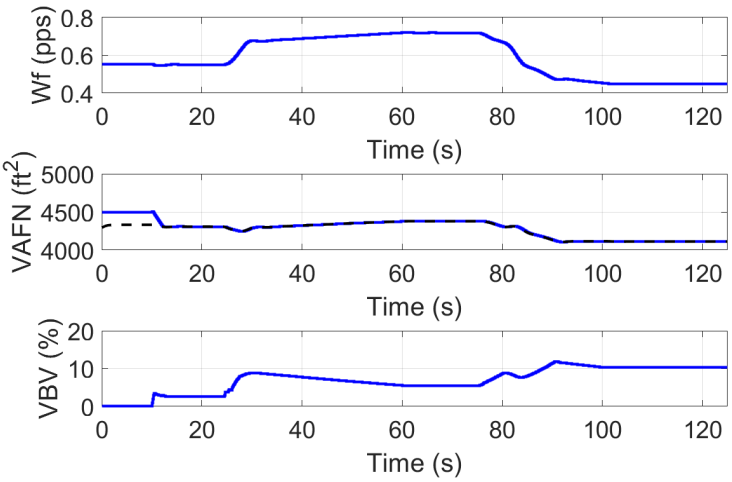

Figure 3.9: The time histories of the fueling rate, VAFN area, and VBV position with the Decentralized MPC simulated on the Simplified model. VAFN reference is shown as a dashed black line.

The simulation results of the Centralized MPC in closed-loop with the Simplified system are displayed in Figures 3.10-3.16. Again, the controller becomes active at 10 seconds. The responses of the power load, bus voltage, and battery power responses, respectively in Figures 3.10, 3.11, and 3.12 are identical to the Decentralized MPC responses. The bus voltage Mil-Specs are violated and this is again attributed to model mismatch. As in the simulations of the Decentralized MPC, the Centralized MPC is activated at t=10 seconds.

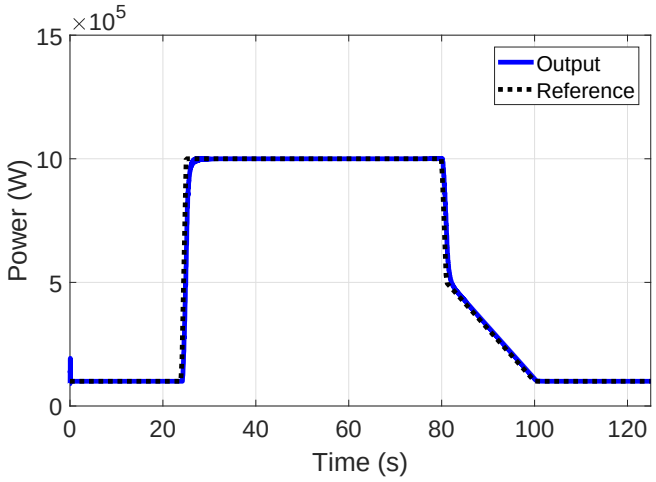

Figure 3.10: Power load reference and response from the Centralized MPC applied to the Simplified model.

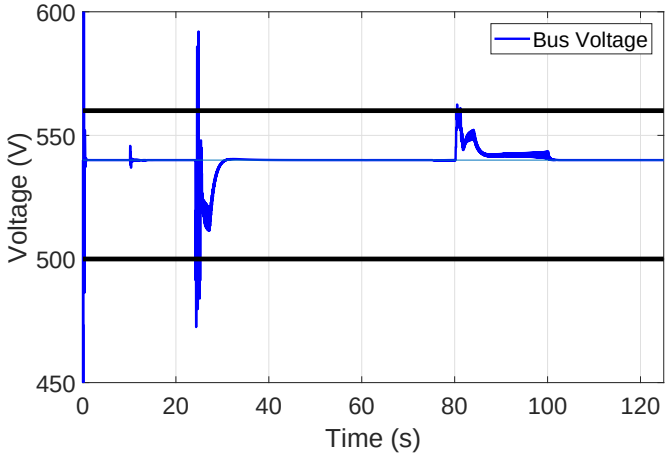

Figure 3.11: Bus voltage response with the Centralized MP, the constraint is shown as black lines.

The time history of the split factor command in Figure 3.13 indicates considerably more shifting of the load balance onto the LP shaft connected generator, reaching a 90-10 split compared to the 50-50 with the Decentralized MPC. This slows the rotation of the LP shaft, helping to alleviate difficulties with the surge margin constraint, as will be explained in the following engine results.

The thrust response from the Centralized MPC is shown in Figure 3.14, where the knowledge of the incoming torque loads from the generators enables the controller to dampen the thrust deviations at 25 and 80 seconds considerably. Figure 3.15 shows the LP SM constraint is active as soon as the controller turns on at 10 seconds, although the

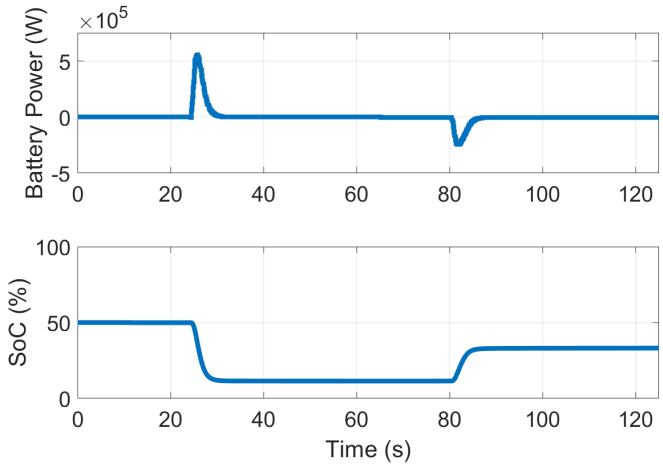

Figure 3.12: Time histories of the battery power and state of charge with the Centralized MPC.

Centralized MPC is able to dampen the impact of the power load jump at 25 seconds. With the power loads shifted to the LP shaft connected generator, the VBV is allowed to close further, as shown in Figure 3.16, staying below 5% open before the split factor constraint forces it to open up to about 7.5% open, lower than the 10% of the Decentralized MPC meaning that the Centralized controller is able to reduce the amount of worked air that is needed to be bled.

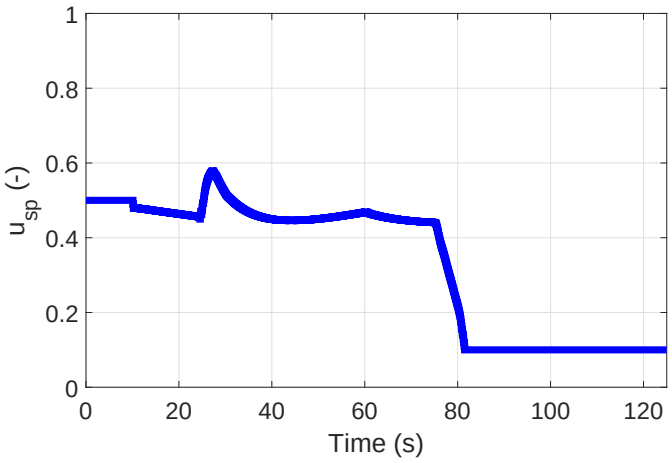

Figure 3.13: The time history of the split factor command with the Centralized MPC on the Simplified model.

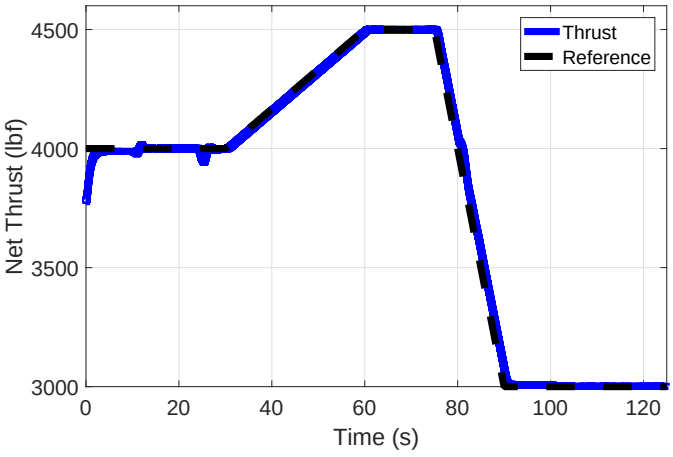

Figure 3.14: Time histories of the net thrust and thrust reference with the Centralized MPC simulated on the Simplified model.

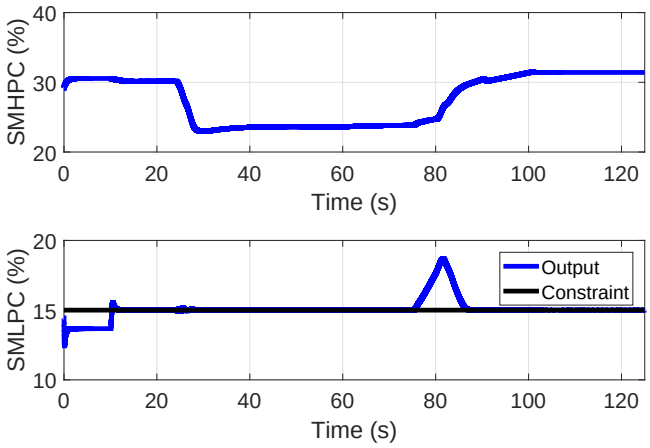

Figure 3.15: Surge margin time histories for the engine compressor surge margins from the Centralized MPC applied to the Simplified model.

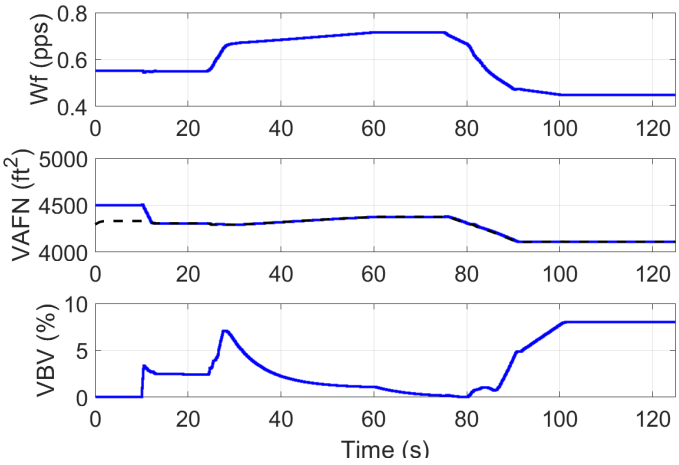

Figure 3.16: Engine actuation time histories from the Centralized MPC on the Simplified model. VAFN reference is shown in black.

3.3.1 Under-Actuated Engine

The Centralized MPC is able to exploit the interactions between the subsystems as another actuation signal for the engine, as was demonstrated by the fact that coordination enabled the VBV to close further than the non-coordinated case. To further examine the capabilities of coordination, the VBV is now fixed at 7.5% to reduce the degrees of freedom available to the MPCs. The VAFN has only a minor impact on the LP shaft dynamics, thus the fuel flow is the only point of actuation directly available in the engine subsystem. However, the fuel flow is also the main driver of the engine thrust, thus certain scenarios are potentially impossible for the engine subsystem.

The simulation results results in Figures 3.17-3.21 illustrate how the locking of the VBV has made the differences between the Centralized and Decentralized MPCs much starker. The power and bus voltage results in Figures 3.17 demonstrate that both controllers are able to track the power demand but still struggle with the voltage constraint at 25 seconds. However, the controllers do diverge in their usage of the battery and, to a greater extent, the split factor, in Figure 3.18. As before, the Centralized MPC still draws a majority of the power load from the LP shaft in order to help with the LP surge margin. The thrust responses in Figure 3.20 show that the Decentralized MPC struggles to meet the thrust reference for a large portion of the simulation and instead has a constant offset. The LP surge margin in Figure 3.21 shows that during those instances, the LP surge margin constraint is active for the Decentralized controller. On the other hand, the Centralized MPC is able to leverage the power flow split factor in Figure 3.18 in order to allow for the thrust tracking to be unaffected until hitting the split factor constraint just past 80 seconds into the simulation. At that point, the Centralized MPC runs out of avenues through which to bleed energy out of the LP shaft and at 100 seconds loses thrust tracking, although there does appear to be some effort to charge the batteries in Figure 3.18 to increase the power flow from the engine.

Oscillations in the engine inputs in Figure 3.21 are caused by the MPC responses running into the LP compressor SM safety limit while trying to track the thrust reference in Figure 3.20.

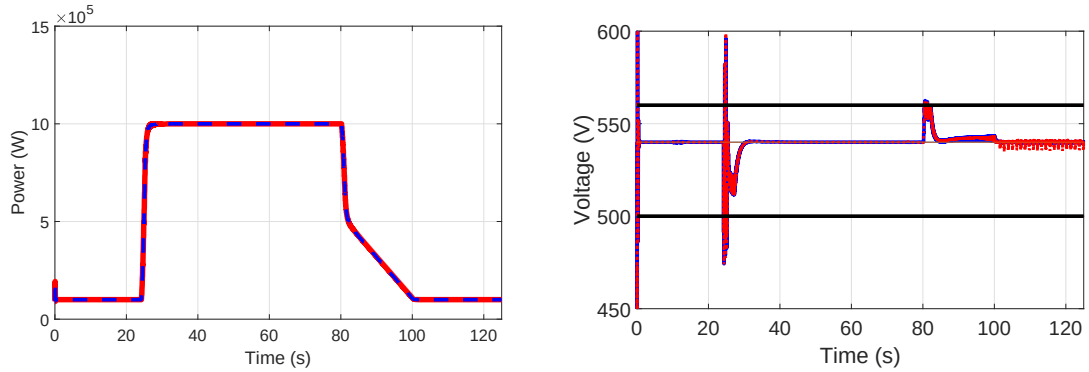

Figure 3.17: Simulated results for the CPL (left) and HVDC bus voltage responses (right) from the Centralized (red) and Decentralized (blue) MPCs Simulated on the Simplified model with fixed VBV. Voltage Mil-Spec is shown in black.

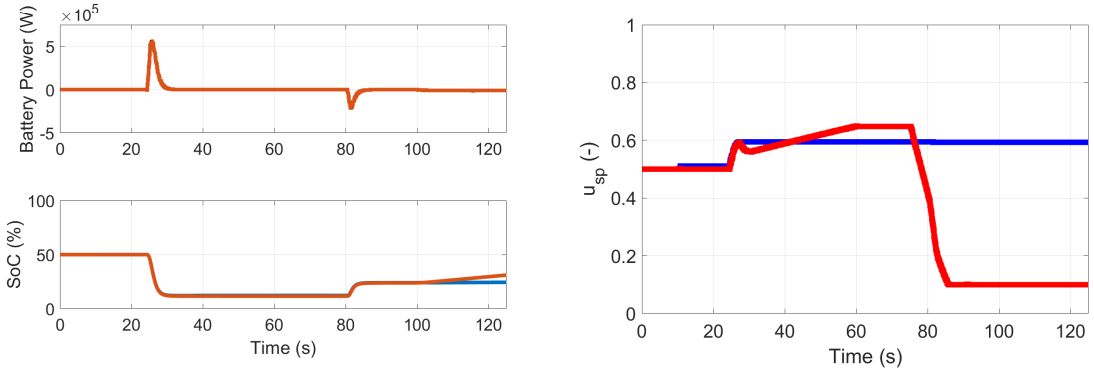

Figure 3.18: Time histories of the battery power (top, left), battery state of charge (bottom, left), and split factor command (right) with the Centralized (red) and Decentralized (blue) MPCs on the Simplified model with fixed VBV.

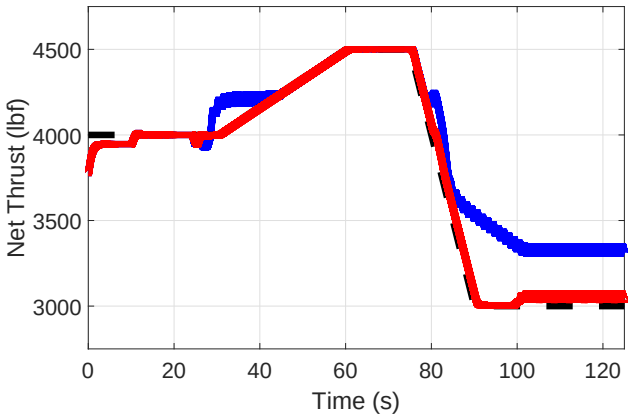

Figure 3.19: Thrust responses from the Centralized MPC (Red) and Decentralized MPC (Blue) with the VBV locked.

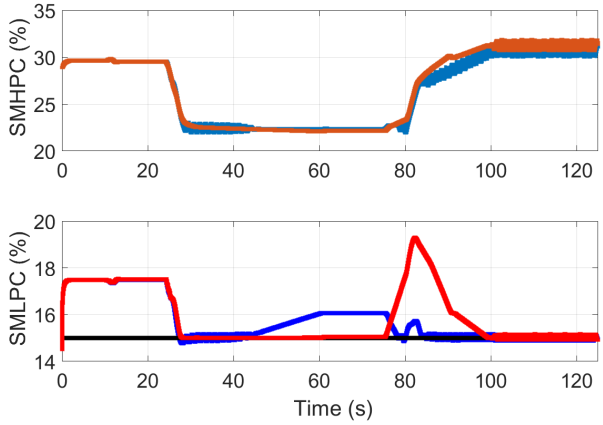

Figure 3.20: Time histories of the compressor surge margins with the Centralized MPC (red) and Decentralized MPC (blue) on the Simplified model.

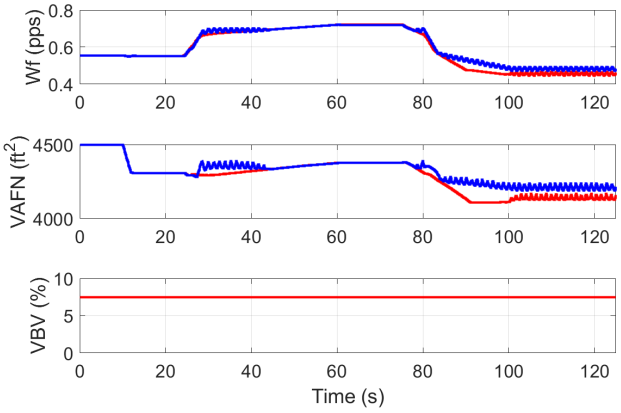

Figure 3.21: Engine actuations with the Centralized MPC (red) and Decentralized MPC (blue) on the Simplified model with fixed VBV.

3.4 Anticipation of Power Load

Coordination of the subsystems enabled the engine to track the thrust reference in the presence of the surge margin constraint by giving the engine additional degrees of freedom through the generator torques. However, the large changes in the power load request lead the control responses to excite the faster electrical modes, causing violations of the bus voltage constraints. This issue could be handled through tighter rate-limits on the power load command from the controller, but would lead to a slower response to the changes in demand which may not be acceptable to flight or mission critical power loads. The solution that is explored in this section is the use of preview of the changes in the power load demand along the controller prediction horizon, enabling the controller to prepare by ramping up or down the slower moving generators in conjunction with the faster energy storage to offset the additional power added to the bus. In doing so, the power generation should be better positioned to respond to the power load requests, damping the voltage transients.

In order to implement the preview of the reference command into the MPC, the change in the reference, $\Delta r(k) = r(k+1) - r(k)$, is added to the error dynamics as

$$e(k+1) = C\Delta x(k) + D\Delta u(k) - \Delta r(k), \tag{3.17}$$

and enters the extended state dynamics in Equation (3.8) as

$$\bar{x}(k+1) = \bar{A}\bar{x}(k) + \bar{B}\Delta u(k) + \bar{R}\Delta r(k), \tag{3.18}$$

where

$$\bar{R} = \begin{bmatrix} \mathbf{0}_{n_{\Delta x} \times n_e} \\ -I_{n_e \times n_e} \\ \mathbf{0}_{(n_y+n_u)\times n_e} \end{bmatrix}. \tag{3.19}$$

The rate based MPC problem in (3.13) is then augmented with the reference dynamics as

$$\begin{aligned} \min_{\Delta u} \; & J(\Delta u, \bar{x}), \\ \text{subject to } \bar{x}(k+1) = & \bar{A}\bar{x}(k) + \bar{B}\Delta u(k) + \bar{R}\Delta r(k), \\ & \Delta u(k) \in \mathcal{D}, \\ & u(k) \in \mathcal{U}, \\ & y(k) \in \mathcal{Y}, \\ & \text{given } x(0),\ u(-1). \end{aligned} \tag{3.20}$$

The MPC formulation with anticipation in (3.20) exploits a preview of the power loads one second in advance, which is the prediction horizon of the MPC. Preview of the power load can be considered non-causal as the MPC is given knowledge of events before they occur, but this can be implemented by delaying the request satisfaction by an amount of time sufficient to enable the benefits of preview in the MPC. Another strategy is to implement a stochastic forecast of the references, as is explored in Chapter 5.

Simulations of the Centralized MPC with and without anticipation are performed on the Simplified model. The power load responses, blown up for detail at transients, are shown in Figures 3.22 and 3.23, and demonstrate that the anticipation allows for faster tracking of the power load, with reduced offset during transients. Again, the controllers become active at 10 seconds and are solved as quadratic programming problems using MATLAB's `quadprog.m` solver.

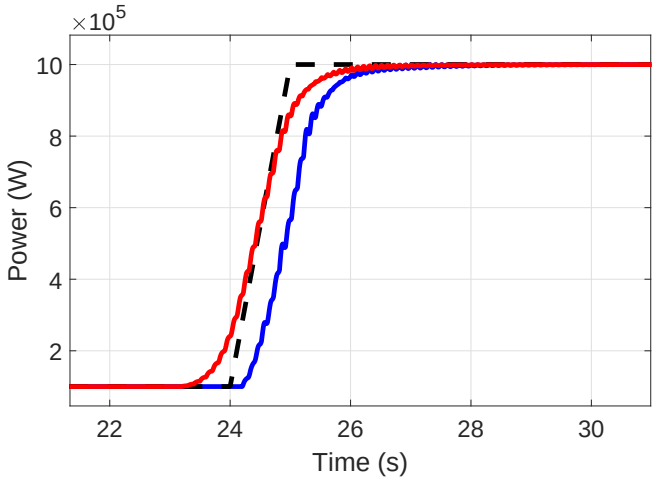

Figure 3.22: Current through the PL resistor around the increase in power load request at 25 seconds for the Centralized MPC with (Red) and without (Blue) load preview on the Simplified model. The reference profile is shown as a dashed black line.

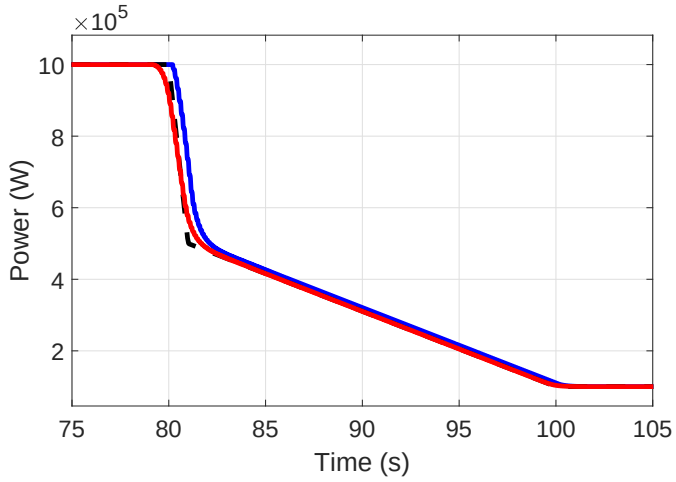

Figure 3.23: Current through the PL resistor around the ramped decrease in the power load request between 80 and 100 seconds for the Centralized MPC with (Red) and without (Blue) load preview on the Simplified model. The reference profile is shown as a dashed black line.

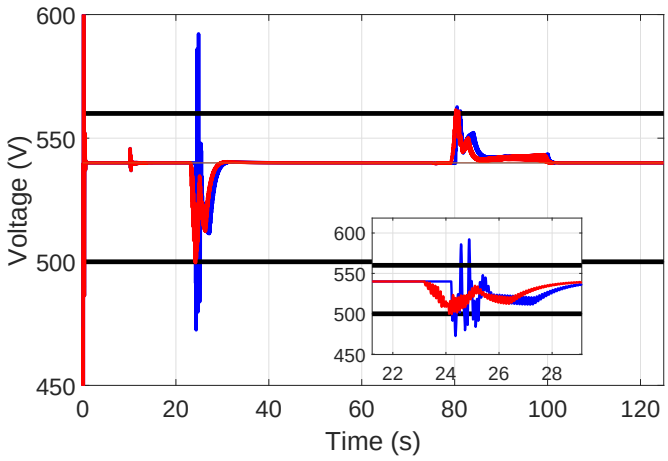

Figure 3.24: Time histories for the bus voltages with (red) and without (blue) anticipation of the power load, inset is a blow up of the responses between 22 and 28 seconds. The Mil-Spec constraints are shown in black.

Figure 3.24 demonstrates the impact of anticipation on the controllers' ability to maintain the bus voltage specifications required by the Mil-Spec guidelines. The voltage violations near 25 seconds by the non-anticipating controller has disappeared from the anticipating control response, see the inset of Figure 3.24. The response at 80 seconds is slightly damped, although neither controller is in violation of Mil-Spec at that instance due to the allowance of short deviations under 0.01 seconds.

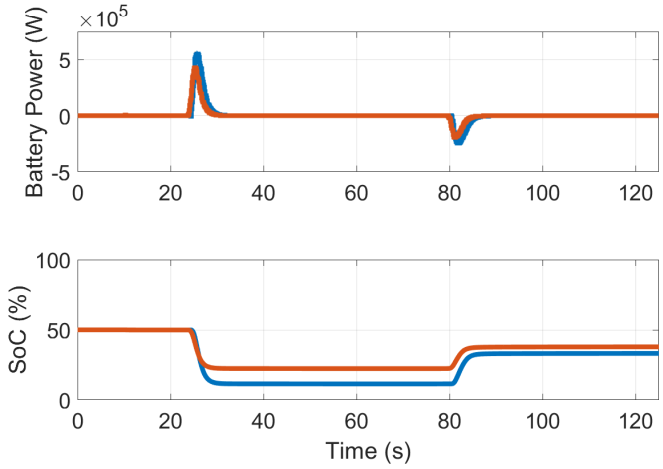

Figure 3.25: Responses from the battery pack of the Simplified model with the Centralized MPC with (red) and without (blue) load anticipation.

Battery power usage decreases with anticipation, as Figure 3.25 illustrates, as the controller is not reacting to highly penalized violations but taking preemptive action. The split factor command in Figure 3.26 remains relatively unchanged with and without power load preview.

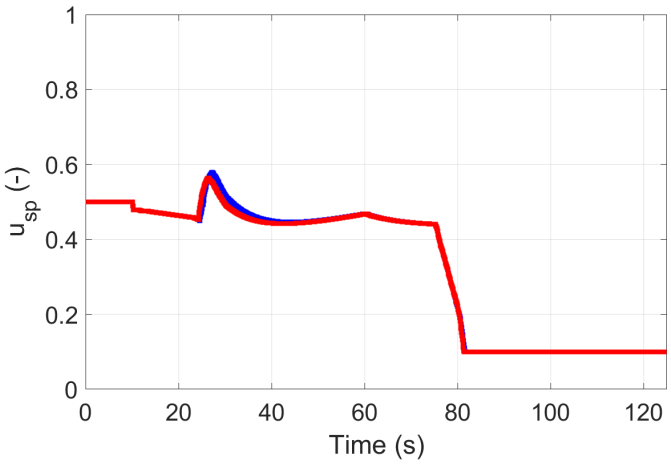

Figure 3.26: Time history of the split factor commands with (red) and without (blue) anticipation of the power load in the Centralized MPC.

Power load anticipation has a minimal impact on the engine response. The thrust time histories in Figure 3.27 show that both the anticipating and non-anticipating controllers are able to track the reference. The fuel flow and VBV both move earlier with anticipation than without it while the VAFN is unchanged in Figure 3.28. The surge margins in Figure 3.29 also display little difference with or without power load anticipation.

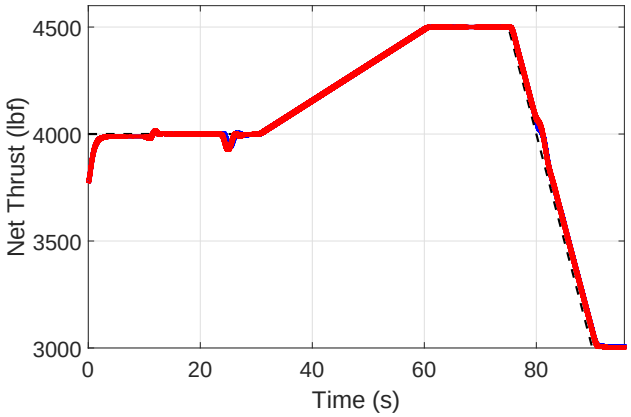

Figure 3.27: Thrust reference and simulated responses from the engine by the Centralized MPC with (red) and without (blue) load anticipation.

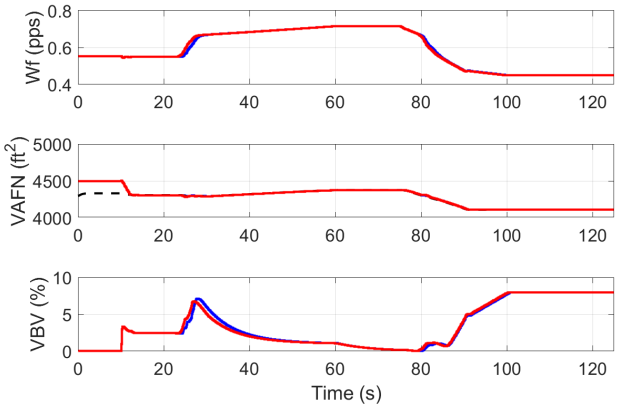

Figure 3.28: Time histories of the engine inputs from the Centralized MPC with (red) and without (blue) anticipation of the power load.

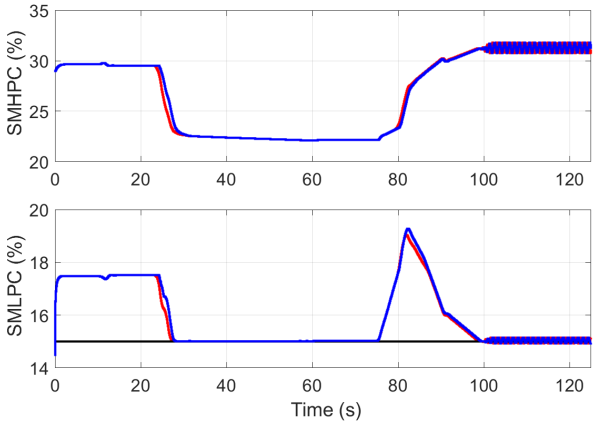

Figure 3.29: Surge margin time histories from the Centralized MPC with (red) and without (blue) anticipation of the power load.

Implementing load preview could be done with a delay in power load satisfaction, however, minimizing this delay may be necessary for flight critical loads. For example, a one second delay in the movement of the flight control surfaces would lead to many accidents on take-off and landing. Thus it is desirable to minimize the delay between a load being known and being satisfied. A study of the impact of the lead time in the preview was made and is shown in Figure 3.30. Note that the penalties in the cost functions have been tuned for the 1 second preview case.

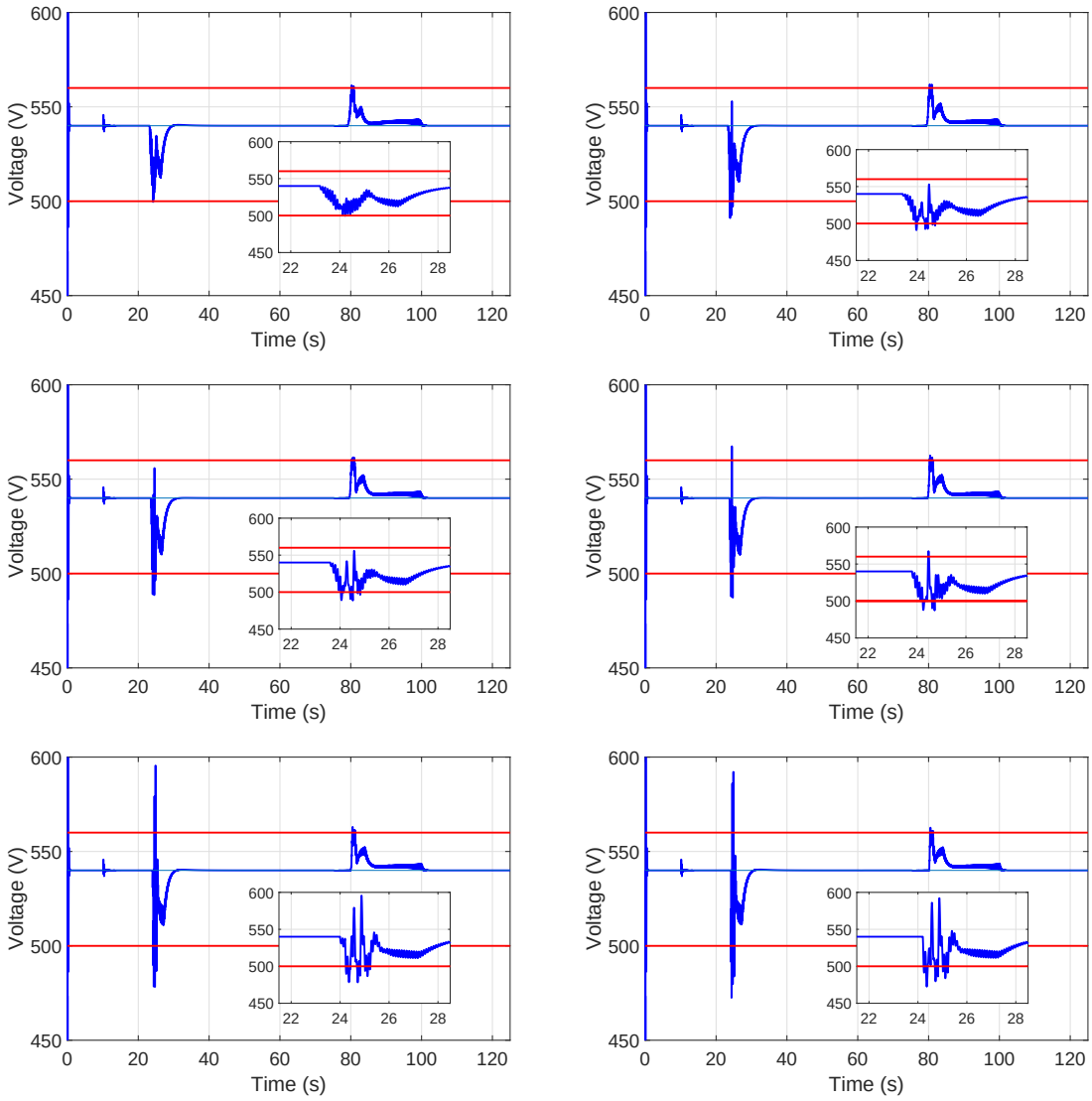

Figure 3.30: Spread of results for the length of time power load changes are given anticipation. From left to right, top to bottom: 1 s, 0.8 s, 0.6 s, 0.4 s, 0.2 s, and no anticipation.

As before, the 1 second preview case does not violate the constraint at 25 seconds. With 0.8 seconds of anticipation, the MPC does have a violation of the lower limit at 25

seconds. This progressively gets worse as the preview time decreases until the 0.2 second preview case that is indistinguishable from the no anticipation case. The above discussion suggests that there are two approaches to maintain bus voltage fluctuations within limits: 1) Power load preview lead time, 2) Rate-limits on the CPL actuation in order to prevent the excitation of the faster voltage modes.

3.5 Detailed Model Results

The previous sections examined the impact of coordination and anticipation on the application of MPC to the Simplified model. In this section, the control strategies are demonstrated on the Detailed model, with higher fidelity dynamics for the electrical distribution and an engine representative of an existing platform. Four MPC strategies are examined based on the possible combinations of with or without coordination and with or without load anticipation. All controllers use the parameters presented in Table 3.3. The controllers with preview are given changes 0.3 seconds in advance, the length of the prediction horizon. The Detailed model was found to require different tunings and a shorter horizon than the Simplified model in order to achieve similar performance in tracking the profiles and constraint enforcement. This is due to the differences in the system and in the linear models used for control synthesis. The controllers are posed as quadratic programming problems and solved using MATLAB's `quadprog.m`. The results of the simulations are presented in Figures 3.31-3.38.

Table 3.3: Penalties and parameters for the Centralized and Decentralized MPCs on the Detailed model.

Variable	Description	Value	Variable	Description	Value
T	Controller time step	10 ms	n_h	Horizon length	30 (0.3 s)
Q_{thr}	Thrust penalty	10^{-8}	R_{FAR}	FAR penalty	0.1
Q_{PL}	PL penalty	0.01	Q_V	Voltage ref penalty	10^{-3}
Q_{Batt}	Battery use penalty	5×10^{-4}	R_{PL}	PL penalty	0.1
R_V	Voltage ref penalty	1	R_{sp}	Split ref penalty	1
R_{Batt}	Battery ref penalty	1			

The engine thrust results, in Figure 3.31, show that the controllers are grouped by whether or not they are centralized. The reference rapidly rises from 25,000 lbf to 37,000 lbf over the first coupled seconds, the last second of which no controller can meet. At 2 seconds, the power draw from the power load, in Figure 3.35, rises dramatically. The two coordinated controllers are able to regain thrust tracking and, besides a ripple at 4 seconds

from the power load dropping, maintain thrust tracking for the remainder of the simulation. A second thrust peak occurs at 6.5 seconds, reaching 36,000 lbf, which the Decentralized controllers fail to reach. The time histories of the HP SM in Figure 3.32 illustrate the difficulties the controllers have in tracking the reference. The HP SM constraint becomes active at 1 second, the Centralized MPC controllers are able to move the compressor response from the limit just before 2 seconds, while the decentralized controllers take until the thrust drop at 4 seconds. Similar result occurs between 6 and 8 seconds. Increasing the penalty on thrust tracking was found to diminish the offset at 1 to 2 seconds, but would drive the HP SM to a steady violation of the constraint that would increase with the penalty. This is due to the soft constraining of the HP SM constraint allowing the controller to trade off violations for improved tracking of the thrust. The LP SM is shown in Figure 3.33, and all controllers are able to enforce the constraint. The FAR inputs of the controllers are given in Figure 3.34 and show a similar grouping to the thrust responses.

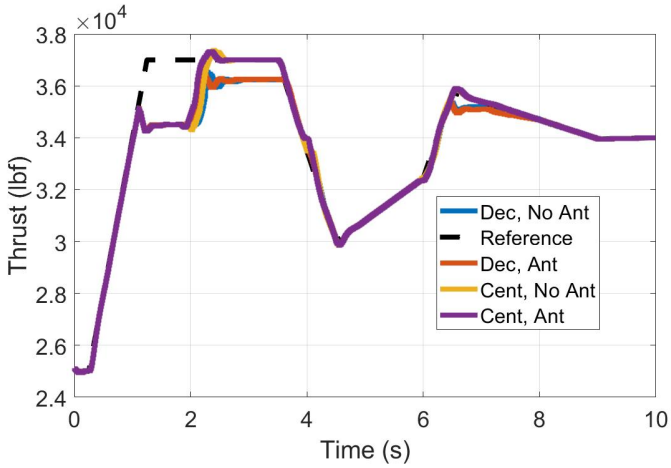

Figure 3.31: Thrust time histories from the Detailed model with the four MPC controllers. Reference given as a dashed black line.

The power load reference in Figure 3.35 starts with a base load of 94 A before a step up to 408 A at 2 seconds. With a resistance of 0.9 Ohms in the CPL, this is an increase from roughly 8 kW to 150 kW. The power load then drops to 200 A (35 kW) at 4 seconds before rising again at 6 seconds to 340 A (110 kW), finally ramping back down to 8 kW from 7 to 9 seconds. All controllers are able to track the loads although the controllers that use load anticipation are quicker to react to changes, particularly noticeable around the jump at 2 seconds. The bus voltage response in Figure 3.36 is violated by the Decentralized MPC with no preview at 2 and 4 seconds and by the Decentralized MPC with preview at 4 seconds. Figure 3.37 illustrates how the battery is used to counter the movements of the voltage and, in the anticipation cases, as an outlet to allow the generators to ramp faster.

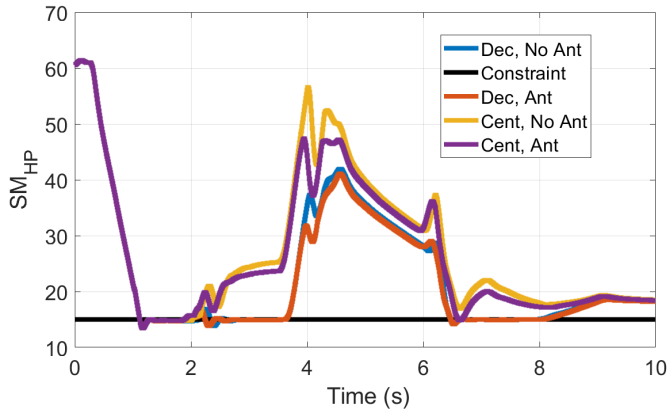

Figure 3.32: Time history of the high pressure compressor surge margin responses from the MPC strategies with constraint, as applied to the Detailed model.

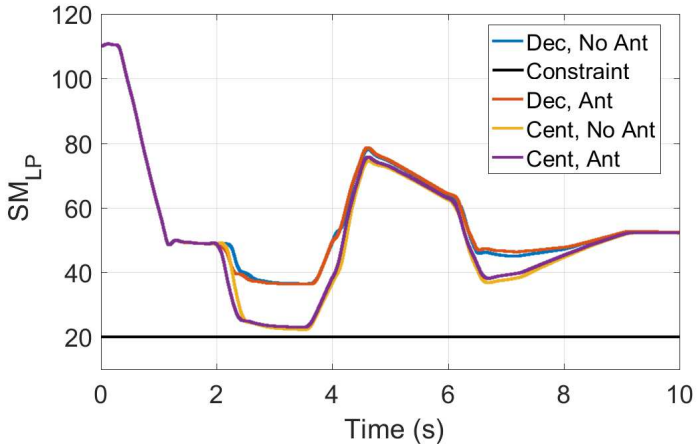

Figure 3.33: Time history of the low pressure compressor surge margin responses from the MPC strategies with constraint, as applied to the Detailed model.

The constraint violation by the Decentralized MPC with preview appears to be caused by the battery putting power on the bus to allow the generators to ramp down before the power load drops, but model mismatch causes the voltage to rise above the constraint.

The generator power split command traces in Figure 3.38 again shows the clear grouping of the controllers by coordinating and non-coordinating controllers. While the Decentralized MPC controllers stay near the 50-50 generator split, the Centralized MPC controllers draw around 70% of their power from the HP shaft. This aids in the thrust tracking by alleviating the surge margin constraints, as was previously discussed in comments on Figures 3.31 and 3.32.

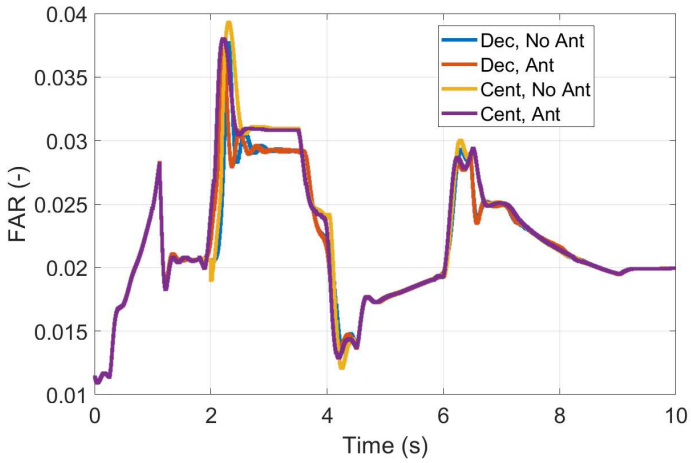

Figure 3.34: Fuel-to-air ratio time histories with the four MPC strategies on the Detailed model.

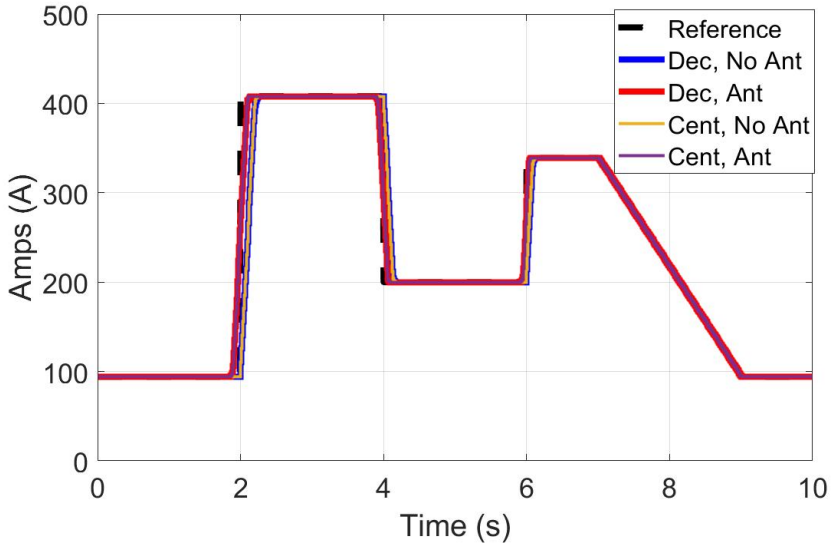

Figure 3.35: Time history of the CPL responses from the MPC strategies as applied to the Detailed model.

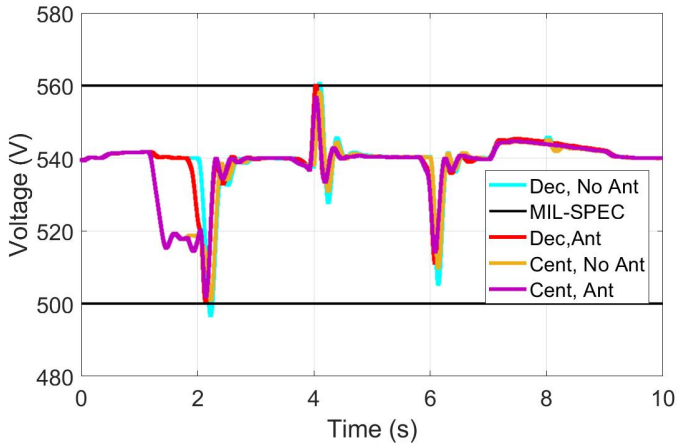

Figure 3.36: Bus voltage time histories from the four MPC strategies as applied to the Detailed model.

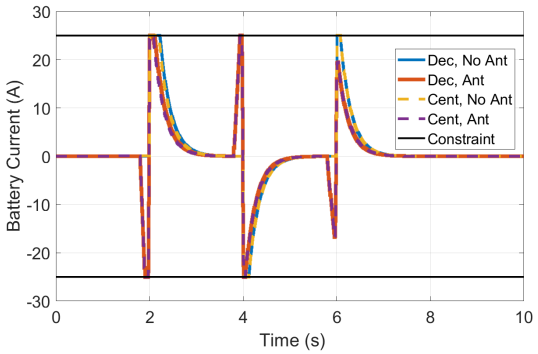

Figure 3.37: Battery command time histories from the four MPC strategies as applied to the Detailed model.

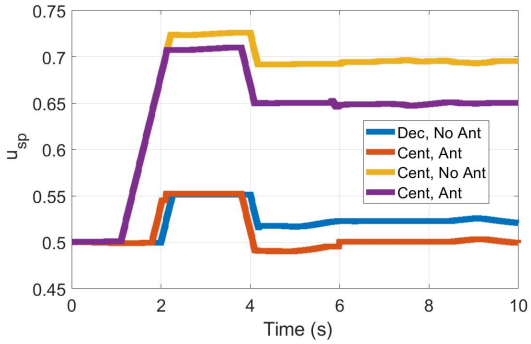

Figure 3.38: Time histories of the generator power splits from the four MPC strategies.

3.6 Discussion

This chapter introduced strategies for an effective MEA engine and power controller, namely a rate-based prediction model, coordination between subsystems, and anticipation of the power load demand. The rate-based MPC formulation facilitates the use of a single linearized model for control development, despite model mismatch errors with the non-linear system. Coordination among the subsystems greatly enhances the ability of the controllers to track the engine thrust references, despite the presence of surge margin constraints or under-actuation of a subsystem, such as in the locked bleed valve case study. In these scenarios, the ability to modify the generator torques as an indirect input is able to impact the shaft dynamics sufficiently to help with the compressor surge margins. Controllers that leverage a preview of the changes in the power load references are able to dampen the bus voltage deviations that come from the solid-state power regulation without sacrificing the speed at which the loads are satisfied.

However, implementing such an idealized controller requires that the predictive control of the subsystems be centralized and that exact knowledge of the future trajectory of the references are known. Achieving similar results to such a control strategy with practical barriers such as competing entities designing the subsystem controllers or inexact preview of the future is considered in the remaining chapters.

CHAPTER 4

Multiple Time-Scales D-MPC

This chapter describes a predictive control framework for the MEA engine-power system with asynchronous distributed controllers. The subsystem controllers perform independent optimizations on their local inputs and must communicate in order to achieve an acceptable system level response. The subsystems and their controllers are assumed to be designed by competing entities, requiring the preservation of subsystem privacy as an integral part of any coordination mechanism. As the controllers are separately developed and have differing time-scales in their dynamics, their control update rates are not guaranteed to be synchronized.

A distributed model predictive control (D-MPC) algorithm for coordination of the subsystem interactions based on the alternating direction method of multipliers (ADMM) is proposed, which accounts for and exploits the multi-rate control updates of the engine and power subsystem controllers while preserving privacy. An extension to the algorithm that seeks to minimize the communication volume required by down-sampling the interactions to the rate of the engine time-scale is also presented. Simulation results on the Simplified and Detailed engine-power models demonstrates the control architectures' abilities as compared to the Decentralized and fully Centralized MPC solutions.

A large body of literature has been made on D-MPC over the past decade, surveys of which can be found in [85, 86, 87]. Optimality for D-MPC is typically measured by how close the architecture control solution can approximate that of a centralized MPC with full knowledge of the system and authority over all inputs. Algorithms seeking optimal results commonly augment local subsystem cost functions with a globalizing term, allow them to account for the impact of their inputs on the entire system [88]. These algorithms require the subsystems to exchange information and iterate on control solutions until a consensus is reached. In [89], the authors present a coordinating D-MPC strategy where the subsystem cost functions are augmented with a linear combination of all subsystem costs, requiring that subsystems have complete knowledge of how their inputs affect neighboring dynamics

and objectives. Iterative controllers are required to achieve an optimal solution but constraint feasibility can be difficult to ensure if the algorithm is stopped prematurely. Another approach to D-MPC seeks to achieve system constraint feasibility over optimality. One example is a contract based method presented in [90] that requires only minimal communication and is structured to allow subsystem modularity. An iterative method is chosen for this work as coordination between the subsystems is desired, as shown from the results in Chapter 3. Recent research into distributed control on aircraft subsystems [91, 44, 92] has found that distributed control of turbine engines can reduce overall weight, increase component modularity, and reduce maintenance costs. Control of mobile thermodynamic subsystems, such as aircraft and automotive subsystems, has been approached from a power flow perspective using non-linear MPCs [31] and a passivity based Decentralized MPC [32].

Architectures that distribute control of a system based on slow and fast dynamics are called singularly perturbed [93]. This is relevant to MEA control where the speed of the fast power modes and slow engine modes can be separated by several orders of magnitude. A survey of papers applying MPC to the singularly perturbed problem is given in [94]. A common strategy is to develop a hierarchical solution where the slower modes are driven by an MPC or other optimal controller while the faster modes are stabilized using a simple feedback controller [95]. Applications of MPC to both the slow and fast modes have been examined; however, in [95], the faster subsystem MPC is given full knowledge over the slow subsystem dynamics in order to prevent de-stabilizing actions and in [96], the MPCs are decentralized. In [97], the time-steps of the MPC are varied such that they are shorter near the current time to stabilize the faster modes and longer towards the end of the prediction horizon for the slower modes. The authors of [97] suggest that such a method could be distributed with the fast and slow modes separated. That is the approach taken in this work, where the faster power subsystem dynamics require shorter MPC time-steps to stabilize than the engine.

The Alternating Direction Method of Multipliers (ADMM) is an algorithm for solving distributed convex optimization problems, and is closely related to techniques such as Douglas-Rachford splitting and proximal methods [98]. This makes it well suited for linear D-MPC applications where the central problem is typically convex. A recent example of such an application of ADMM for D-MPC is given in [99], with comparisons to the closely related Method of Multipliers. Previously, ADMM based D-MPC was applied to the MEA problem in [57]; however no considerations were made for privacy or the differing time-scales of the subsystems. In this work, privacy is defined as withholding the local dynamics, inputs, or objectives from any communication.

The background for the problem is given in Section 4.1. The Centralized and Decentralized MPC solutions to the multiple time-scales MEA control problem are given in Section 4.2. The Multiple Time-Scales D-MPC (MT D-MPC) algorithm solving the centralized problem with distributed controllers operating at differing update rates and its foundation in theory is presented in Section 4.3. The extension to the solution, the Down-Sampled Multiple Time-Scales D-MPC (DMT D-MPC), is given in Section 4.4, with simulation results. Section 4.5 presents simulation results of the D-MPC architectures on the Detailed model along with a case study for an unexpected change in reference between coordinated updates and a timing study. A discussion of the results are given in Section 4.6.

4.1 Background

The focus of this work is in the distribution of the predictive control in the MEA system. The subsystem controllers are given reference profiles, assumed to originate from a path planner optimizing for some mission-level cost, and the outputs are the optimized inputs to a lower-level actuation loop, as discussed in Chapter 2. Local subsystems are assumed to be developed independently by competing entities, requiring that any coordination must consider privacy of the controllers and account for differences in their update rates. A high-level view of the approach taken is outlined in Figure 4.1, with distributed MPCs coordinating interacting variables.

4.1.1 Privacy

The subsystems are assumed to be developed and manufactured by subcontractors that are potentially in competition with each other across various projects. Thus, the details of the subsystems and their controllers may be considered intellectual property (IP) and their designers would be hesitant to use model based coordination that could risk exposing it.

A unified mathematical definition of privacy has not yet been devised. In state estimation and network consensus, such as in [100], privacy is considered as a filtering or sanitizing of the states of a subsystem when sharing them in order to remove private information. In [101], privacy in computer network control is cited as preventing the sharing of full topological information among client networks. For this work, we assume that privacy is preserved if the states, models, and cost functions of each subsystem are not shared as they could reveal some novel technology within the subsystem. Coordination is then done on trajectories of the interactions between the subsystems as these variables would already be observable by each subsystem through their own dynamics. The interactions between

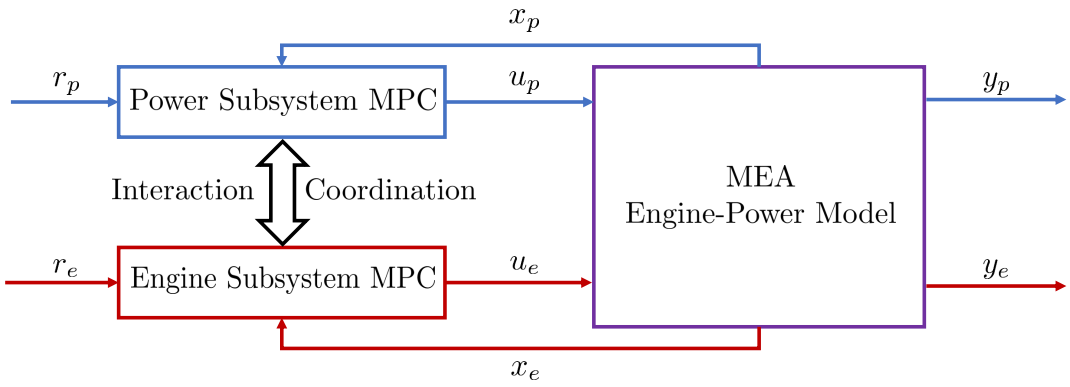

Figure 4.1: Diagram of the control approach taken in the distributed algorithms of this chapter.

aircraft subsystems is typically handled by setting static limits during component sizing and requirement generation, not online during system operation.

4.1.2 Interaction Rate-Based Model

To coordinate the interaction variables, a modeling framework for the subsystems utilizing them is introduced. In Chapter 3, coordination is done using centralized models using the rate-based system dynamics in Equations (2.44) and (2.45). However, these require full knowledge of the states of each subsystem. So we return to the linearized models from Equations (2.41), (2.42), and (2.43), repeated here for $i \in \{e,\ p\}$,

$$\delta x_i(k+1) = A_i \delta x_i(k) + B_i \delta u_i(k) + W_{ij} \delta x_{ij}(k), \tag{4.1}$$

$$\delta y_i(k) = C_i \delta x_i(k) + D_i \delta u_i(k), \tag{4.2}$$

$$\delta x_{ji}(k) = E_{ji} \delta x_i(k) + F_{ji} \delta u_i(k). \tag{4.3}$$

The extended rate-based states remain $\bar{x}_i(k) = [\Delta x_i^T(k)\ e_i^T(k)\ y_i^T(k)\ u_i^T(k)]^T$, but the rate-based dynamics for each subsystem is now

$$\bar{x}_i(k+1) = \bar{A}_i \bar{x}_i(k) + \bar{B}_i \Delta u_i(k) + \bar{R}_i \Delta r_i(k) + \bar{W}_{ij} \Delta x_{ij}(k), \tag{4.4}$$

where

$$\bar{W}_{ij} = \begin{bmatrix} W_{ij} \\ \mathbf{0}_{(n_e+n_y+n_u)\times n_v} \end{bmatrix}, \tag{4.5}$$

the dimension of the vector x_{ij} is n_v and $\Delta x_{ij}(k) = x_{ij}(k) - x_{ij}(k-1)$. In the case of the MEA engine and power coupling, $n_v = 2$, for the shaft speeds $x_{pe} = [\omega_{HP},\ \omega_{LP}]^T$ produced by the engine and generator torques $x_{ep} = [\tau_{HP},\ \tau_{LP}]^T$ produced by the microgrid.

Table 4.1: Key variables for Chapter 4.

Variable	Description
$x_i,\ \Delta x_i$	States and change in states of subsystem i
$\bar{x}_i$	Extended states of subsystem i for rate-based MPC
$u_i,\ \Delta u_i$	Inputs and change in inputs of subsystem i
$\hat{u}$	Unique inputs after move blocking
$x_{ij},\ \Delta x_{ij}$	Interacting variables and their rates, impacting i originating from j
$\tilde{x}_{ij}$	Requested interacting variable by i
y_i	Outputs of subsystem i
r_i	References for subsystem i
e_i	Tracking error for subsystem i

4.1.3 Multiple Time-Scales

One assumption used in previous chapters was that each controller updated their inputs at the same rate of every T seconds. The slower dynamics of the engine subsystem as compared to the power subsystem and the federated design process leads to the assumption that the controllers are built with differing update rates. The subsystem controllers update at a rate of T_i seconds, where $i = \{e,\ p\}$, and that $T_e > T_p$, that is, the power controller updates more often than the engine controller. For simplicity, we assume that the ratio $\kappa = T_e/T_p$ is an integer, $\kappa \in \mathbb{N}$. This is visualized in Figure 4.2 for $\kappa = 3$. The predictive controllers are formulated with prediction at the rate of T_p and then the slower engine update rate can be represented through move-blocking as

$$\begin{bmatrix} u_e(0) \\ \vdots \\ u_e(n_h-1) \end{bmatrix} = M_e \begin{bmatrix} \hat{u}_e(0) \\ \vdots \\ \hat{u}_e(n_h^e-1) \end{bmatrix}, \tag{4.6}$$

where $M_e \in \mathbb{R}^{n_h \times n_h^e}$ is the move blocking matrix, $n_h^e = n_h/\kappa$ is the engine control horizon length, and $\hat{u}_e(k)$ are the unique engine inputs with move blocked actions removed. The

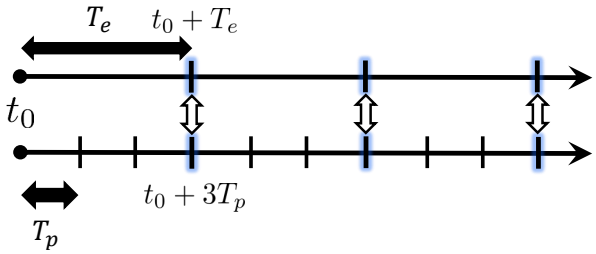

Figure 4.2: Visualization of the multi-rate updates of the power and engine subsystems. The controllers perform an iterative consensus update at times when the coarse T_e and fine T_p steps coincide. In this example, $\kappa = 3$.

move blocking matrix contains all zeros with a single entry set to one in each row and is constructed as

$$M_e = I_{n_h^e} \otimes \mathbf{1}_{\kappa \times 1}, \tag{4.7}$$

where $\otimes$ represents the Kronecker product. An example of a move-blocking matrix for the first time three time-steps in Figure 4.2 is

$$\begin{bmatrix} u_e(0) \\ u_e(1) \\ u_e(2) \end{bmatrix} = \begin{bmatrix} 1 & 0 & 0 \\ 1 & 0 & 0 \\ 1 & 0 & 0 \end{bmatrix} \begin{bmatrix} \hat{u}_e(0) \end{bmatrix}. \tag{4.8}$$

The move blocking constraint in (4.6) can be written without the need for the unique inputs $\hat{u}_e(k)$ as $U_e \in Im(\mathcal{P}_e)$, where $\mathcal{P}_e = M_e^T M_e$ is a projection matrix and $U_e = [(u_e(0))^T, \ldots, (u_e(n_h - 1))^T]^T$ is a vector stacking the control inputs over the prediction horizon.

4.2 Centralized and Decentralized Solutions

The centralized solution of the multiple time-scales MEA engine and power problem is formulated as, given full authority over the engine and power subsystem inputs and knowledge of all states and outputs, it represents the optimal result with respect to the cost functions and prediction models available. The decentralized solution to the problem where both subsystems are separately controller with no coordination is also considered as the best possible solution without communication.

The Centralized MPC problem with the subsystem interaction model and move-blocking

constraint is defined as

$$\begin{aligned}
&\min_{\Delta u_e,\ \Delta u_p} J_e(\Delta u_e, \bar{x}_e) + J_p(\Delta u_p, \bar{x}_p), \qquad (4.9)\\
\text{subject to } \bar{x}_i(k+1) =& \bar{A}_i \bar{x}_i(k) + \bar{B}_i \Delta u_i(k) + \bar{R}_i \Delta r_i(k) + \bar{W}_{ij} \Delta x_{ij}(k),\\
&\Delta x_{ij}(k) = E_i \Delta x_i(k) + F_i \Delta u_i(k),\\
&\Delta u_i(k) \in \mathcal{D}_i,\\
&u_i(k) \in \mathcal{U}_i,\\
&y_i(k) \in \mathcal{Y}_i,\\
&U_e \in Im(\mathcal{P}_e),\\
&\text{given } x_i(0),\ u_i(-1),
\end{aligned}$$

where $i \in \{e,\ p\}$, $j \in \{e,\ p |\ j \neq i\}$, and $k = [0, \cdots, n_h]$.

However, in order to apply the alternating direction method of multipliers (ADMM) to the system, it is required to have an equality constraint that connects the subsystem problems. The subsystems are made to optimize with a request of the incoming interaction variables, $\Delta\tilde{x}_{ij}$, that is applied to the local subsystem dynamics. Consistency in the system is maintained by the constraint $\Delta\tilde{x}_{ij}(k) = \Delta x_{ij}(k)$. The Centralized MPC problem can then, with the slight abuse of notation for the arguments of the cost function, be re-stated as

$$\begin{aligned}
&\min_{\Delta u_e,\ \Delta u_p,\ \Delta\tilde{x}_{ep},\ \Delta\tilde{x}_{pe}} J_e(\Delta u_e, \bar{x}_e) + J_p(\Delta u_p, \bar{x}_p), \qquad (4.10)\\
\text{subject to } \bar{x}_i(k+1) =& \bar{A}_i \bar{x}_i(k) + \bar{B}_i \Delta u_i(k) + \bar{R}_i \Delta r_i(k) + \bar{W}_{ij} \Delta\tilde{x}_{ij}(k),\\
&\Delta x_{ij}(k) = E_i \Delta x_i(k) + F_i \Delta u_i(k),\\
&\Delta\tilde{x}_{ij}(k) = \Delta x_{ij}(k)\\
&\Delta u_i(k) \in \mathcal{D}_i,\\
&u_i(k) \in \mathcal{U}_i,\\
&y_i(k) \in \mathcal{Y}_i,\\
&U_e \in Im(\mathcal{P}_e),\\
&\text{given } x_i(0),\ u_i(-1),
\end{aligned}$$

where $i \in \{e,\ p\}$, $j \in \{e,\ p |\ j \neq i\}$, and $k = [0, \cdots, n_h]$. Note that the MPC problems described in (4.9) and in (4.10) are mathematically equivalent.

The Decentralized solution to the problem is described by zeroing out the interaction variables, removing the connection between the subsystem dynamics and the need for the consistency constraint. With the move-blocking constraint, the Decentralized Power Subsystem MPC becomes

$$\begin{aligned} &\min_{\Delta u_p} J_p(\Delta u_p, \mathbf{0}), \\ \text{subject to } \bar{x}_p(k+1) =& \bar{A}_p \bar{x}_p(k) + \bar{B}_p \Delta u_p(k) + \bar{R}_p \Delta r_p(k), \\ & \Delta u_p(k) \in \mathcal{D}_p, \\ & u_p(k) \in \mathcal{U}_p, \\ & y_p(k) \in \mathcal{Y}_p, \\ & \text{given } x_p(0),\ u_p(-1), \end{aligned} \tag{4.11}$$

for $k = [0, \cdots, n_h]$ and the Decentralized Engine MPC is

$$\begin{aligned} &\min_{\Delta u_e} J_e(\Delta u_e, \mathbf{0}), \\ \text{subject to } \bar{x}_e(k+1) =& \bar{A}_e \bar{x}_e(k) + \bar{B}_e \Delta u_e(k) + \bar{R}_e \Delta r_e(k), \\ & \Delta u_e(k) \in \mathcal{D}_e, \\ & u_e(k) \in \mathcal{U}_e, \\ & y_e(k) \in \mathcal{Y}_e, \\ & U_e \in Im(\mathcal{P}_e), \\ & \text{given } x_e(0),\ u_e(-1), \end{aligned} \tag{4.12}$$

for $k = [0, \cdots, n_h]$.

Simulations of the Centralized and Decentralized MPCs are done on the Simplified model with the VBV locked at 7.5% open. Locking the VBV was shown in Chapter 3 to create a large spread in the results of the between coordinating and non-coordinating controllers, particularly in the ability to track the thrust references. This is useful for comparisons with the D-MPC strategies given in this chapter as distributed coordination is one of their main objectives. The power controller time-step is kept at $T_p = 0.1$ s while the engine controller updates at steps of $T_e = 0.5$ s. The tunings from Table 3.2 are used. The problems are solved using MATLAB's `quadprog.m` solver.

The results for the multiple time-scales Centralized and Decentralized MPCs on the Simplified model are given in Figures 4.3-4.6. The same reference profile as was applied in Chapter 3 is given to the controllers, with the power load demand previewed one second

out. Both controllers are successfully able to track the power load reference in Figure 4.3, where the responses are layered on top of each other. The voltage responses in that same figure show that both controllers are able to satisfy the Mil-Spec constraint, with acceptable deviations under 0.01 seconds. The battery and split factor commands in Figure 4.4 again appears similar to the results of Section 3.3.

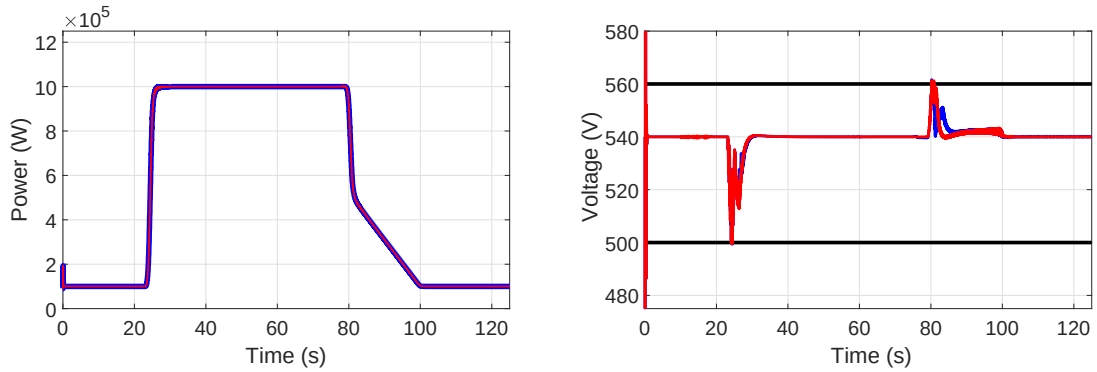

Figure 4.3: Simulation results for the CPL power load current (Left) and HVDC bus voltage (Right) responses from the multiple time-scales Centralized (Blue) and Decentralized (Red) MPCs on the Simplified model.

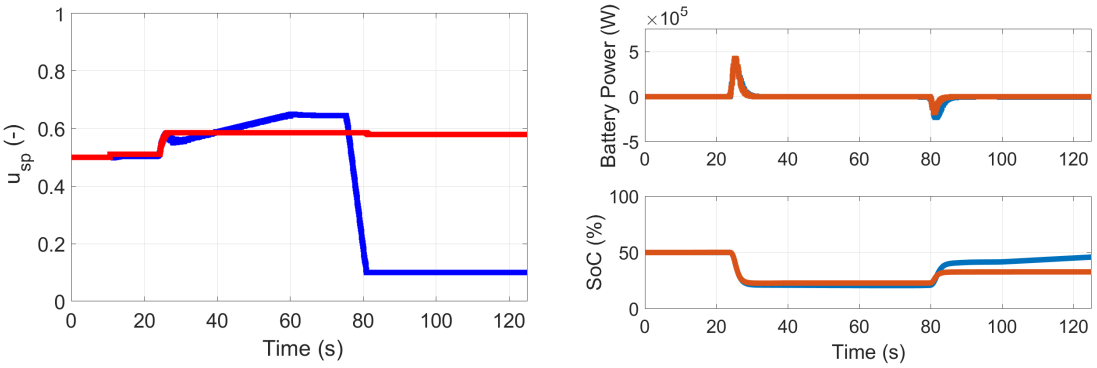

Figure 4.4: Time histories of the split factor command (Left) and battery responses (Right) from the multiple time-scales Centralized (Blue) and Decentralized (Red) MPCs on the simplified model.

The reduced engine update rate leads to poorer net thrust tracking, as seen in Figure 4.5 where the Centralized MPC has a constant offset during transients. As in the previous chapter, centralizing the MPC enables the leveraging of the balance of the power loads drawn by the generators in order to achieve better tracking performance than the Decentralized MPC. Both controllers are still able to enforce the surge margin constraint, as seen in Figure 4.5, recalling that the controllers engage at 10 seconds. The control input trajectories for both controllers are plotted in Figure 4.6.

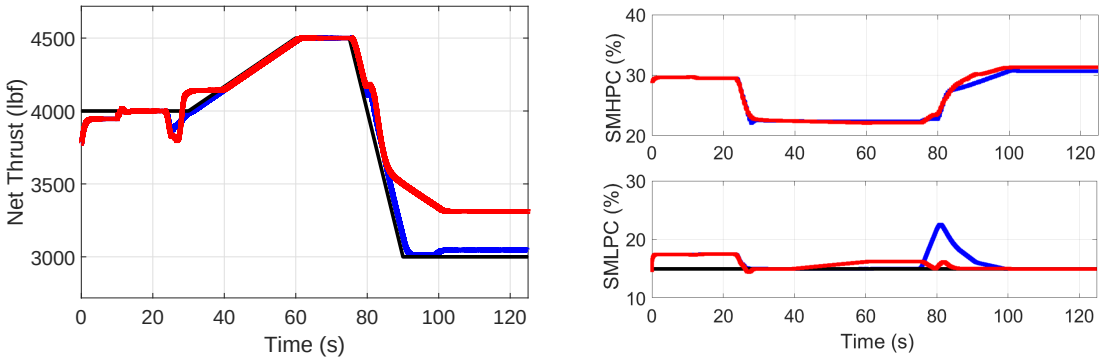

Figure 4.5: Simulation results for the net engine thrust and surge margin responses from the multiple time-scales Centralized (Blue) and Decentralized (Red) MPCs on the Simplified model. The LP surge safety constraint is shown in black.

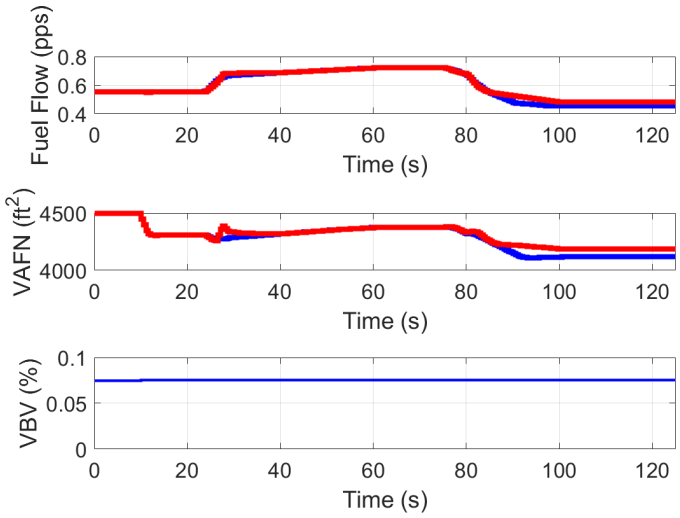

Figure 4.6: Histories for the engine control inputs from the multiple time-scales Centralized (Blue) and Decentralized (Red) MPCs on the Simplified model. The VAFN reference signals are omitted for clarity.

The addition of the multiple time-scales clearly impacts how fast the MPC could respond to changes, as evidence by the increased deviations at 25 and 80 seconds by the thrust in response to the power load shifts. Additionally, distinction between the Centralized and Decentralized strategies remains, as seen by the loss of thrust tracking only by the Decentralized MPC from 25 to 40 and 80 to 125 seconds.

4.3 Multiple Time-Scales D-MPC

A method for solving (4.10) in a distributed fashion while preserving subsystem privacy is now proposed. The algorithm is referred to as the Multiple Time-Scales Distributed Model Predictive Control (MT D-MPC) and is described in Algorithm 4.1. On time-steps where both the engine and power controllers are updating, an ADMM strategy is used to drive the subsystem controllers to a consensus on the interaction variables. This only requires that the subsystems share trajectories of the actual and requested interactions over the prediction horizon, allowing the local cost functions and dynamics to remain hidden. For the time instants where only the power controller is updating, the interaction variable trajectories and requests along with the Lagrange multipliers that result from the previous joint update are used in the input optimization. This allows for the power subsystem controller flexibility in its actions while considering the penalty to a system-wide cost function for deviations. The ADMM method is chosen for coordination of the subsystems as it typically is able to converge to a solution near optimal within a limited number of iterations [98].

Capital notation is used to denote the trajectory over the horizon for certain variables, for example $X_{ij} = [(x_{ij}(1))^T, \ldots, (x_{ij}(n_h))^T]$, see Table 4.2 for a complete listing. The ADMM based algorithm is formulated by removing the interaction consistency constraint, written in trajectory form as $X_{ij} = \tilde{X}_{ij}$, and defining the augmented Lagrangian for each subsystem as

$$\mathcal{L}_i = J_i(\Delta U_i, \tilde{X}_{ij}) + \sum_i \sum_{j \neq i} \left[\nu_{ij}^T (X_{ij} - \tilde{X}_{ij}) + \frac{\rho_{ij}}{2} \|X_{ij} - \tilde{X}_{ij}\|_2^2 \right], \tag{4.13}$$

where ρ_{ij} is a penalty parameter and ν_{ij} is the Lagrange multiplier associated with the constraint $X_{ij} - \tilde{X}_{ij} = 0$. Subsystem dynamics and constraints are grouped into the constrained augmented Lagrangian as

$$\begin{aligned} \bar{\mathcal{L}}_i = J_i(\Delta U_i, \tilde{X}_{ij}) + \sum_i \sum_{j \neq i} [\nu_{ij}^T (X_{ij} - \tilde{X}_{ij}) + \frac{\rho_{ij}}{2} \|X_{ij} - \tilde{X}_{ij}\|_2^2], \\ \text{subject to } (\Delta U_i, \tilde{X}_{ij}) \in \mathcal{C}_i, \end{aligned} \tag{4.14}$$

where $\mathcal{C}_i$ is a single set representation of all dynamic, input, and output constraints as defined for each subsystem in Section 4.2.

Algorithm 4.1 The Multiple Time-Scales D-MPC

Input: $\bar{x}_e(t)$, $\bar{x}_p(t)$,$X_{ep}(t-T_p)$, $X_{pe}(t-T_p)$, $\tilde{X}_{ep}(t-T_p)$, $\tilde{X}_{pe}(t-T_p)$, $\nu_{ep}(t-T_p)$, and $\nu_{pe}(t-T_p)$, ▷ Initialize with current states and previous trajectories

Output: $u_e(t)$, $u_p(t)$, $X_{ep}(t)$, $X_{pe}(t)$,$\tilde{X}_{ep}(t)$, $\tilde{X}_{pe}(t)$, $\nu_{ep}(t)$, and $\nu_{pe}(t)$,

$X_{ep} = \Theta X_{ep}(t-T_p)$, $X_{pe} = \Theta X_{pe}(t-T_p)$, ▷ Shift previous results , see Eq. (4.15),

$\tilde{X}_{ep} = \Theta \tilde{X}_{ep}(t-T_p)$, $\tilde{X}_{pe} = \Theta \tilde{X}_{pe}(t-T_p)$,

$\nu_{ep} = \Theta \nu_{ep}(t-T_p)$, $\nu_{pe} = \Theta \nu_{pe}(t-T_p)$,

if $t = n \cdot \kappa,\ n \in \mathbb{N}$, **then** ▷ Both controllers updating

  while $\|X_{ep} - \tilde{X}_{ep}\|_2^2 \geq \epsilon_{ep}$ or $\|X_{pe} - \tilde{X}_{pe}\|_2^2 \geq \epsilon_{pe}$ **do** ▷ Until primal convergence of the interaction constraints

    $[\Delta U_p^+, X_{ep}^+, \tilde{X}_{pe}^+] = \min_{\Delta U_p,\ \tilde{X}_{pe}} \bar{\mathcal{L}}_p(\Delta U_p, \nu_{ep}, \tilde{X}_{ep}, \nu_{pe}, X_{pe}, \tilde{X}_{pe})$, ▷ Power update

    $\nu_{ep}^{+/2} = \nu_{ep} - \rho_{ep}(1-\lambda)(X_{ep}^+ - \tilde{X}_{ep})$, ▷ Lagrange multipliers half update

    $\nu_{pe}^{+/2} = \nu_{pe} - \rho_{pe}(1-\lambda)(X_{pe} - \tilde{X}_{pe}^+)$,

    $[\Delta U_e^+, X_{pe}^+, \tilde{X}_{ep}^+] = \min_{\Delta U_e,\ \tilde{X}_{ep}} \bar{\mathcal{L}}_e(\Delta U_e, \nu_{pe}^{+/2}, \tilde{X}_{pe}^+, \nu_{ep}^{+/2}, X_{ep}^+, \tilde{X}_{ep})$, ▷ Engine update

    $\nu_{ep}^+ = \nu_{ep}^{+/2} + \rho_{ep}(X_{ep}^+ - \tilde{X}_{ep}^+)$, ▷ Lagrange multipliers full update

    $\nu_{pe}^+ = \nu_{pe}^{+/2} + \rho_{pe}(X_{pe}^+ - \tilde{X}_{pe}^+)$,

  end while

  $u_p(t) = u_p(t-T_p) + \Delta u_p(0)$, ▷ Update inputs

  $u_e(t) = u_e(t-T_e) + \Delta u_e(0)$,

else ▷ Update only power controller

  $[\Delta U_p, \tilde{X}_{pe}] = \min_{\Delta U_p,\ \tilde{X}_{pe}} \bar{\mathcal{L}}_p(\Delta U_p, \nu_{ep}, \tilde{X}_{ep}, \nu_{pe}, X_{pe}, \tilde{X}_{pe})$,

  $u_p(t) = u_p(t-T_p) + \Delta u_p(0)$,

end if

$X_{ij}(t) \Leftarrow X_{ij}$, $\tilde{X}_{ij}(t) \Leftarrow \tilde{X}_{ij}$, $\nu_{ij}(t) \Leftarrow \nu_{ij}$, for $i \in \{e,\ p\},\ j \in \{e,\ p | j \neq i\}$,

Table 4.2: Trajectory vector definitions over the horizon n_h used in formulating the MT D-MPC. The Δ is dropped for the interaction vectors to simplify notation.

Trajectory	**Correlated Variable**
U_i	Control input u_i
ΔU_i	Change in control input Δu_i
Y_i	Subsystem output y_i
X_{ij}	Interaction rate Δx_{ij}
$\tilde{X}_{ij}$	Copy of the interaction rate $\Delta \tilde{x}_{ij}$

The Lagrange multiplier, predicted interaction variable, and requested interaction variable trajectories are all initialized to be vectors of zeros. At each subsequent time-step, the interactions and Lagrange multipliers are advanced by one time step with the shift register Θ, defined here as

$$\Theta = \begin{bmatrix} \mathbf{0} & I & \mathbf{0} & \cdots & \\ \mathbf{0} & \mathbf{0} & I & \cdots & \\ \mathbf{0} & \mathbf{0} & \mathbf{0} & \ddots & \\ \vdots & \vdots & \vdots & & I \\ & & & & I \end{bmatrix}. \tag{4.15}$$

The final element along each advanced trajectory is assumed to remain constant.

On steps with joint updates, the relaxed form of ADMM presented in lines 4 to 14 in Algorithm 4.1 is used in order to determine the control inputs. This begins by a power controller optimization in line 6, followed by a relaxation half update to the multipliers in lines 7 and 8, an engine controller optimization in line 9, and finally completing the multipliers update in lines 10 and 11. This sequence requires that the engine and power controllers communicate twice each iteration. The term λ is a relaxation parameter and the form of ADMM used here was presented in [102]. Convergence is determined once the Euclidean norms of the differences between the predicted and requested interaction trajectories falls below a tolerance of ϵ_{ij}, demonstrating primal convergence of the consistency constraint. The first element of the resulting control input change trajectories from the rate-based optimizations are then added to the current inputs and the process is repeated at the next coordination step.

A simulation of the MT D-MPC as applied to the Simplified model is performed and compared to the Centralized results. The ADMM parameters used by the controller are given in Table 4.3. They are the augmentation penalty to the Lagrangians ρ_{ij}, the primal convergence tolerances ϵ_{ij}, and the relaxation parameter λ. The control problems are solved

with Matlab's `quaprog.m` function.

Table 4.3: Parameter values for the ADMM related terms in the MT D-MPC simulation.

Parameter	Value	Parameter	Value
ρ_{ep}	0.1	ρ_{pe}	0.05
ϵ_{ep}	5	ϵ_{pe}	5
λ	1.9		

The MT D-MPC and Centralized MPC power load responses in Figure 4.7 are identical. The voltage responses differ just past 80 seconds but are otherwise indistinguishable. The MT D-MPC battery command in Figure 4.8 lags behind that of the Centralized MPC at approximately 80 seconds. The split factor command for the load balance on the two generators in Figure 4.9 shows additional variation between the controllers as the MT D-MPC again lags behind the Centralized command, particularly between 80 and 100 seconds.

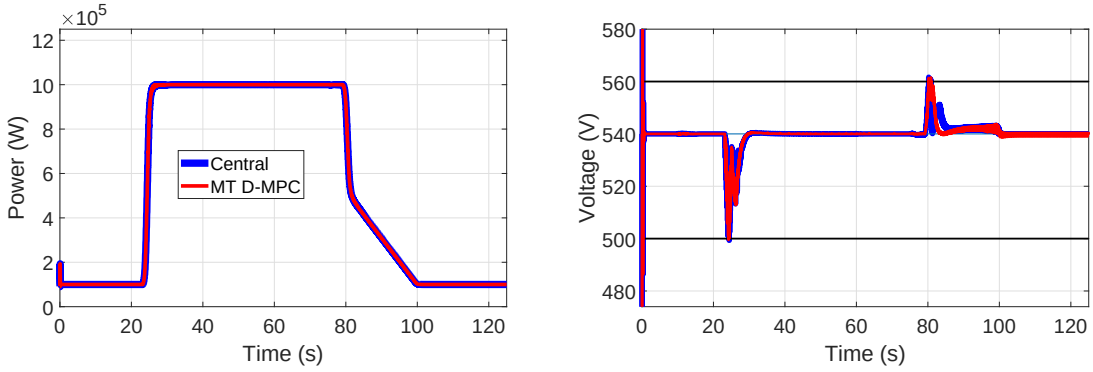

Figure 4.7: Simulation results for the CPL power load and HVDC bus voltage responses from the Centralized (Blue) and MT D-MPC (Red) MPCs on the Simplified model.

Both controllers display similar thrust tracking performance, as seen in Figure 4.10. The surge margin constraints are also satisfied by both controllers. The control input trajectories in Figure 4.11 overlap each other.

The number of ADMM iterations required to achieve consensus in the MT D-MPC are shown in Figure 4.12. There are spikes at the initialization and around the large power load changes at 25 and 80 seconds, but remains below 35 iterations at all times. The offset thrust tracking from the surge margin constraint from 100 seconds until the end of the simulation does cause a rise in the iterations to around 5.

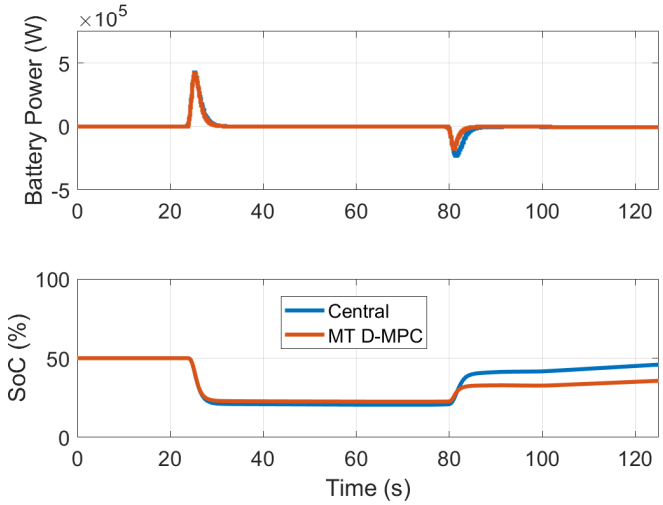

Figure 4.8: Time histories of the battery current from the four controllers on the Simplified model with upper and lower limits shown in black.

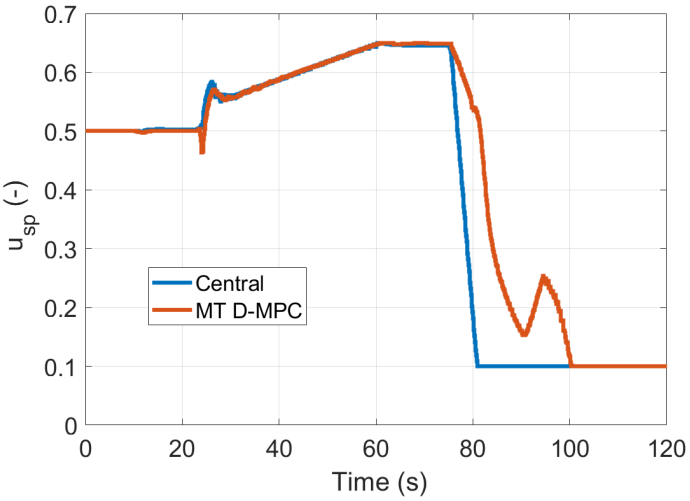

Figure 4.9: Split factor commands from the Centralized MPC (Blue) and MT D-MPC (Red) on the Simplified model.

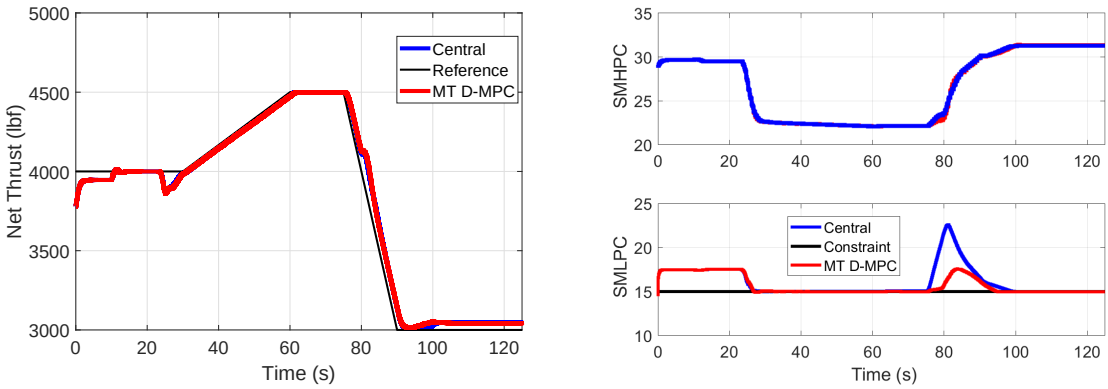

Figure 4.10: Simulation responses for the net engine thrust and the compressor surge margins by the Centralized (Blue) and MT D-MPC (Red) MPCs on the Simplified model.

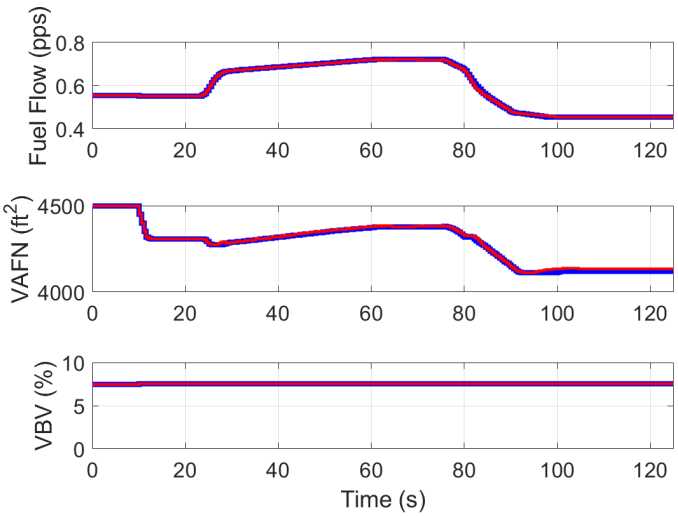

Figure 4.11: Engine inputs by both the Centralized (Blue) and MT D-MPC (Red) MPCs on the Simplified model. The VAFN references are omitted for clarity.

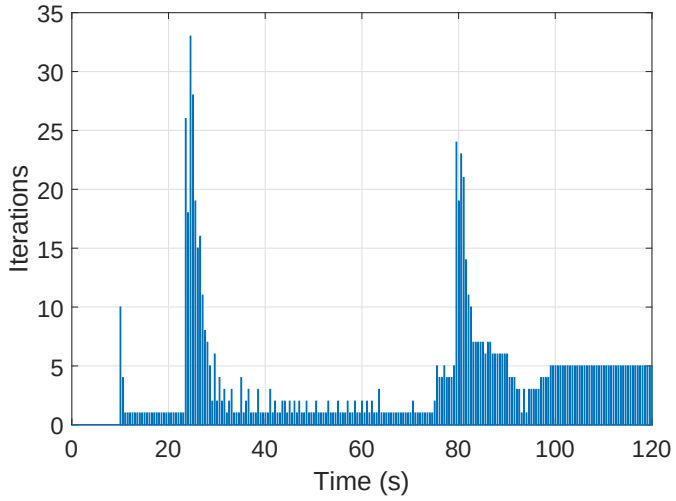

Figure 4.12: Time history for the number of iterations required until convergence in the MT D-MPC.

The simulation results illustrate the MT D-MPC's ability to match the performance of the Centralized MPC, although the variations in control actions suggest that the optimal system point is within a shallow valley of the Lagrangian topology.

4.3.1 Properties of the Algorithm

In this section, the properties of ADMM and the implications for optimality and convergence in the MT D-MPC are considered based on [98, 102], and [103]. To simplify notation, we collect the variables each subsystem controller optimizes over as $Z_i = [(\Delta U_i)^T \; \tilde{X}_{ij}^T]^T$ and note that the subsystem cost can be re-written as $h_i(Z_i) = J_i(Z_i) + \mathcal{I}_{\mathcal{C}_i}(Z_i)$. Recall that $\mathcal{C}_i$ is the representation of all constraints in subsystem i. The indicator function $\mathcal{I}_{\mathcal{C}_i}(Z_i)$ takes a value of zero if Z_i is within the set $\mathcal{C}_i$, otherwise it takes a value of infinity, i.e.,

$$\mathcal{I}_{\mathcal{C}_i}(Z_i) = \begin{cases} 0, & \text{if } Z_i \in \mathcal{C}_i \\ \infty, & \text{else.} \end{cases} \tag{4.16}$$

The central problem can then be re-formulated as

$$\begin{aligned} &\min_{Z_p, Z_e} \; h_p(Z_p) + h_e(Z_e), \\ &\qquad H_p Z_p + H_e Z_e = \mathbf{0}, \end{aligned} \tag{4.17}$$

where,

$$H_p = \begin{bmatrix} \bar{E}_p & \bar{E}_{ep} \\ \mathbf{0} & -I \end{bmatrix}, \quad H_e = \begin{bmatrix} \mathbf{0} & -I \\ \bar{E}_e & \bar{E}_{pe} \end{bmatrix}, \tag{4.18}$$

the matrix $\bar{E}_i$ is a matrix mapping the subsystem input trajectory to the interaction output and $\bar{E}_{ji}$ maps the incoming interaction trajectory to the outgoing interaction through its impact on the subsystem state dynamics. The matrices H_p and H_e are both full rank and surjective by their construction through Equations (4.1)-(4.3). In [104], the assumptions that the objective functions are closed, convex, and proper along with the constraint matrix H_p being surjective were shown to be sufficient to have linear convergence with relaxed forms of ADMM. The variant of ADMM with relaxation through the half-update is presented in [102] and shown to be equivalent to the more traditional method where the Z_p^+ terms in the engine and Lagrange multiplier update would be replaced with $\lambda H_p Z_p^+ - (1-\lambda) H_e Z_e$. Relaxation of ADMM is studied in more detail in [103].

The necessary and sufficient conditions for the minimizer of problem (4.17) include the primal feasibility condition,

$$H_p Z_p^* + H_e Z_e^* = \mathbf{0}, \tag{4.19}$$

and the dual feasibility condition,

$$\mathbf{0} = \nabla h_p(Z_p^*) + H_p^T \nu^*, \tag{4.20}$$

$$\mathbf{0} = \nabla h_e(Z_e^*) + H_e^T \nu^*, \tag{4.21}$$

where $\nu = [\nu_{ep}^T \ \nu_{pe}^T]^T$. The primal residual at an iteration a of the ADMM algorithm is calculated as

$$s_{primal}^a = H_p Z_p^a + H_e Z_e^a, \tag{4.22}$$

or,

$$\begin{aligned} H_p Z_p^a + H_e Z_e^a &= \begin{bmatrix} \bar{E}_p U_p^a + \bar{E}_{ep} \tilde{X}_{pe}^a - \tilde{X}_{ep}^a \\ -\tilde{X}_{pe}^a + \bar{E}_e U_e^a + \bar{E}_{pe} \tilde{X}_{ep}^a \end{bmatrix}, \\ &= \begin{bmatrix} X_{ep}^a - \tilde{X}_{ep}^a \\ X_{pe}^a - \tilde{X}_{pe}^a \end{bmatrix}, \end{aligned} \tag{4.23}$$

the two norm of which is used to determine convergence as $\|s_{primal}^a\|_2^2$ in Line 3 of Algorithm 4.1. The dual residual is calculated as

$$s_{dual}^a = \rho H_p^T H_e (Z_e^a - Z_e^{a-1}). \tag{4.24}$$

For the MEA case, it was found numerically that the primal residual would converge slower than the dual residual.

A theorem for the convergence of the MT D-MPC problem in (4.17) is given in Theorem 4.1. It is based on the results for convergence in ADMM in [98, 103].

Theorem 4.1 (Convergence of the MT D-MPC)**.** *Consider the application of ADMM to the multiple time-scales engine-power control problem stated in* (4.17)*. Suppose the functions* $h_p(\cdot)$ *and* $h_e(\cdot)$ *are closed, proper, convex, feasible at every iterate, and that there exists a point* (Z_p^*, Z_e^*, ν^*) *that satisfies the conditions for primal feasibility* (4.19) *and dual feasibility* (4.20)*. Then the sequences of residuals* s^a_{primal} *and* s^a_{dual} *converge to zero and the sequence of variables* $(Z_p^a, Z_e^a, \nu^a) \to (Z_p^*, Z_e^*, \nu^*)$ *as* $a \to \infty$*.*

Proof. Given in [103, p. 311-313]. □

To ensure feasibility of the MT D-MPC iterates, the output constraints in both subsystems are soft-constrained with slack variables, thus the value functions map to the extended real numbers as $h_e : \mathbb{R}^{n_e} \to \mathbb{R} \cup +\infty$ and $h_p : \mathbb{R}^{n_p} \to \mathbb{R} \cup +\infty$ and are closed, proper, and convex. The distributed problem is formulated from the centralized problem in (4.10), thus the existence of a solution point (Z_p^*, Z_e^*, ν^*) is assumed based on their being a solution for the Centralized MPC. Together, these properties ensure that the conditions of Theorem 4.1 are met by the MT D-MPC. This result and makes no guarantees on the convergence rate, but does demonstrate that Algorithm 4.1 converges.

4.4 Down-Sampled Multiple Time-Scales D-MPC

An extension to the MT D-MPC that coordinates the interaction terms at the slower engine time-scale is presented. Down-sampling the interaction variable trajectories allows for the engine subsystem to use a coarser time step in its optimization. For the engine controller, this reduces the number of optimization variables required for optimization and removes the need for move blocking, reducing its computational burden. Additionally, resolving the interaction variables and the local copies with time steps of T_e reduces the size of the vectors broadcast by the controllers, lowering the communication volume which may be necessary if bandwidth between the controllers is limited. However, the coarser resolution of the coordination would neglect the faster modes of the interactions, producing lower quality results than the MT D-MPC. The Down-Sampled Multiple Time Scales Distributed Model Predictive Control (DMT D-MPC) is given in Algorithm 4.2.

Because the engine controller now works at time steps of T_e, the vectors it produces come out at a coarser resolution over the horizon length shared with the power controller.

Algorithm 4.2 The Down-Sampled Multiple Time-Scales D-MPC

Input: $\bar{x}_e(t)$, $\bar{x}_p(t)$, $X_{ep}(t-T_p)$, $\mathcal{X}_{pe}(t-T_p)$, $\tilde{\mathcal{X}}_{ep}(t-T_p)$, $\tilde{X}_{pe}(t-T_p)$, $\nu_{ep}(t-T_p)$, and $\nu_{pe}(t-T_p)$, ▷ Initialize with current states and previous trajectories

Output: $u_e(t)$, $u_p(t)$, $X_{ep}(t)$, $\mathcal{X}_{pe}(t)$, $\tilde{\mathcal{X}}_{ep}(t)$, $\tilde{X}_{pe}(t)$, $\nu_{ep}(t)$, and $\nu_{pe}(t)$,

$X_{ep} = \Theta X_{ep}(t-T_p)$, $\tilde{X}_{pe} = \Theta \tilde{X}_{pe}(t-T_p)$, ▷ Shift fine terms with Θ

if $t = n \cdot \kappa,\ n \in \mathbb{N}$, **then** ▷ Both controllers updating

  $\mathcal{X}_{pe} = \hat{\Theta}\mathcal{X}_{pe}(t-T_p)$, $\tilde{\mathcal{X}}_{ep} = \hat{\Theta}\tilde{\mathcal{X}}_{ep}(t-T_p)$, ▷ Shift coarse terms with $\hat{\Theta}$

  $\nu_{ep} = \hat{\Theta}\nu_{ep}(t-T_p)$, $\nu_{pe} = \hat{\Theta}\nu_{pe}(t-T_p)$,

  while $\|\mathcal{S}X_{ep} - \tilde{\mathcal{X}}_{ep}\|_2^2 \geq \epsilon_{ep}$ or $\|\mathcal{X}_{pe} - \mathcal{S}\tilde{X}_{pe}\|_2^2 \geq \epsilon_{pe}$ **do**,

    $[\Delta U_p^+, X_{ep}^+, \tilde{X}_{pe}^+] = \underset{\Delta U_p,\ \tilde{X}_{pe}}{\min} \bar{\mathcal{L}}_{p,reg}(\Delta U_p, \nu_{ep}, \tilde{\mathcal{X}}_{ep}, \nu_{pe}, \mathcal{X}_{pe}, \tilde{X}_{pe})$, ▷ Power update

    $\nu_{ep}^{+/2} = \nu_{ep} - \rho_{ep}(1-\lambda)(\mathcal{S}X_{ep}^+ - \tilde{\mathcal{X}}_{ep})$, ▷ Lagrange multipliers half update

    $\nu_{pe}^{+/2} = \nu_{pe} - \rho_{pe}(1-\lambda)(\mathcal{X}_{pe} - \mathcal{S}\tilde{X}_{pe}^+)$,

    $[\Delta U_e^+, \mathcal{X}_{pe}^+, \tilde{\mathcal{X}}_{ep}^+] = \underset{\Delta U_e,\ \tilde{\mathcal{X}}_{ep}}{\min} \bar{\mathcal{L}}_e(\Delta U_e, \nu_{pe}^{+/2}, \mathcal{S}\tilde{X}_{pe}^+, \nu_{ep}^{+/2}, \mathcal{S}X_{ep}^+, \tilde{\mathcal{X}}_{ep})$, ▷ Engine Update

    $\nu_{ep}^{+/2} = \nu_{ep} + \rho_{ep}(\mathcal{S}X_{ep}^+ - \tilde{\mathcal{X}}_{ep}^+)$, ▷ Lagrange multipliers half update

    $\nu_{pe}^{+/2} = \nu_{pe} + \rho_{pe}(\mathcal{X}_{pe}^+ - \mathcal{S}\tilde{X}_{pe}^+)$,

  end while

  $u_p(t) = u_p(t-T_p) + \Delta u_p(0)$, ▷ Update inputs

  $u_e(t) = u_e(t-T_e) + \Delta u_e(0)$,

else ▷ Update only power

  $[\Delta U_p, \tilde{X}_{pe}, X_{ep}] = \underset{\Delta U_p,\ \tilde{X}_{pe}}{\min} \bar{\mathcal{L}}_p(\Delta U_p, \nu_{ep}, \tilde{\mathcal{X}}_{ep}, \nu_{pe}, \mathcal{X}_{pe}, \tilde{X}_{pe})$,

  $\mathcal{X}_{pe}(1) = \mathcal{X}_{pe}(1) - \tilde{X}_{pe}(1)$, $\tilde{\mathcal{X}}_{ep}(1) = \tilde{\mathcal{X}}_{ep}(1) - X_{ep}(1)$, ▷ Satisfied interactions

  $u_p(t) = u_p(t-T_p) + \Delta u_p(0)$,

end if

$X_{ij}(t) \Leftarrow X_{ij}$, $\tilde{X}_{ij}(t) \Leftarrow \tilde{X}_{ij}$, $\nu_{ij}(t) \Leftarrow \nu_{ij}$, for $i \in \{e,\ p\}$, $j \in \{e,\ p | j \neq i\}$,

These slow time-scale interaction trajectories are denoted with the calligraphic font, e.g. $\mathcal{X}_{ij}$. The Lagrange multipliers are also computed at this resolution, requiring the trajectories of the power subsystem to be down-sampled in order to be used for the multiplier and engine updates in lines 7 through 11 of Algorithm 4.2. This is done using the down-sampling operator, $\mathcal{S}$, constructed as

$$\mathcal{S} = I_{n_h^e} \otimes \begin{bmatrix} I_{n_v} & \cdots & I_{n_v} \end{bmatrix}, \tag{4.25}$$

where the second term in the Kronecker is a matrix of κ number of identity matrices, I_{nv}, ordered horizontally. Recalling that the trajectories X_{ij} are of the change in the interactions Δx_{ij} over the horizon, the $\mathcal{S}$ operator sums up the faster power originating trajectories to match the slower engine trajectories. An example over one engine time step for Δx_{ep} is given in Figure 4.13 for the case where $\kappa = 3$.

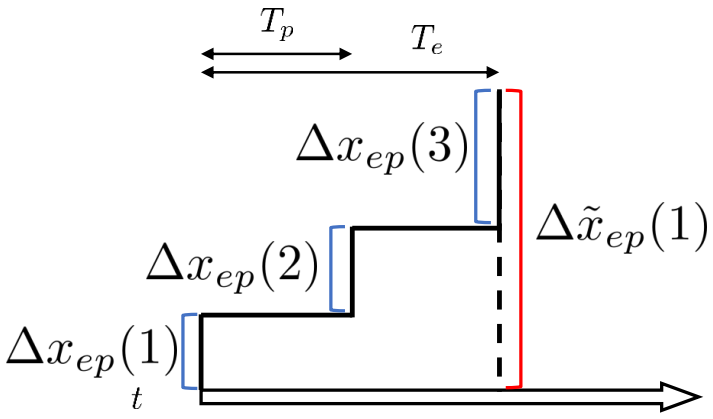

Figure 4.13: Visualization of matching the rate of change in an interaction between the finer time-steps of the power controller and the coarser engine controller.

The shift register $\hat{\Theta}$ operates as Θ does, see Eq. (4.15), but for signals at the engine time-scale and is used only at coordinating steps to warm-start the ADMM iterations. A regularization term is added to the power updates as

$$\bar{\mathcal{L}}_{p,reg} = \bar{\mathcal{L}}_p + \frac{\mu}{2}\|\tilde{X}_{pe}\|_2^2, \tag{4.26}$$

in order to smooth out the interaction requests produced, as they are otherwise only penalized by deviations in summation across multiple time-steps from the engine time-scaled interactions.

Simulation results of the DMT D-MPC are presented below with comparisons to the MT D-MPC. Tunings for the ADMM parameters are given in Table 4.4. Note that the

Table 4.4: Parameter values for the ADMM related terms in the DMT D-MPC simulation.

Parameter	Value	Parameter	Value
ρ_{ep}	0.5	ρ_{pe}	0.5
ϵ_{ep}	0.3	ϵ_{pe}	0.3
λ	1.9	μ	10

tolerances are tighter than from those of the MT D-MPC in Table 4.2 due to the reduced number of terms being coordinated. As seen in the previous controllers in this chapter, the DMT D-MPC is able to track the power load reference and enforce the voltage bus constraints in Figure 4.14. Recall that small deviations in the constraint are allowed by Mil-Spec, see Section 2.1.2.

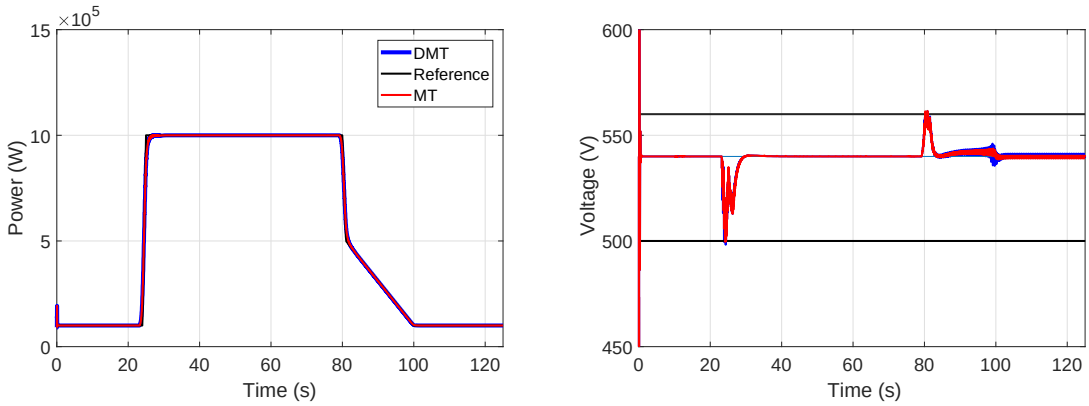

Figure 4.14: The Simplified model power load and bus voltage responses to the DMT (b) and MT (r) D-MPCs.

The battery power command in Figure 4.15 also shows little variation from the MT D-MPC controller but the DMT does make a greater effort to engage the battery during the thrust offset from 100 seconds until the end. The generator power split factor commands of the four control strategies discussed in this chapter in Figure 4.16 illustrates how the DMT D-MPC varies more from the Centralized MPC than the MT D-MPC, particularly from 20 to 80 seconds, but still follows the same general trends.

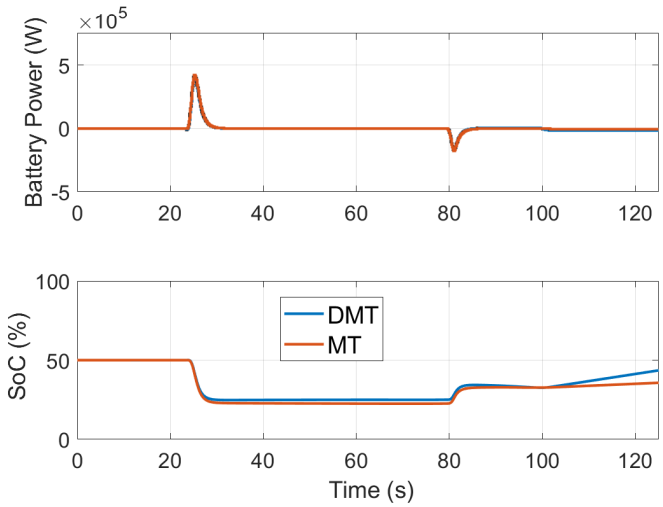

Figure 4.15: Battery usage of the MT and DMT D-MPCs in response to the given profile.

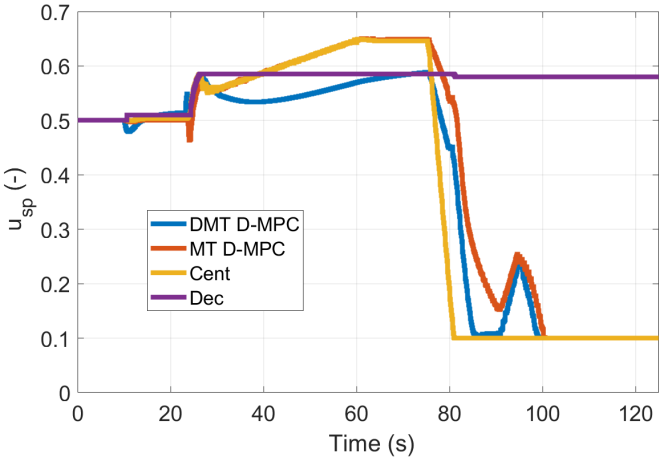

Figure 4.16: Split factor command across the four control architectures as applied to the Simplified model.

The thrust responses to the MT and DMT D-MPCs are given in Figure 4.17, the profile traces are largely the same. The exception is that the DMT is able to regain tracking after power load drop at 25 seconds faster than the MT, and thus the Centralized MPC. Both controllers are successfully able to maintain the LP compressor surge margin, as demonstrated in Figure 4.18. The engine inputs from both controllers, given in Figure 4.19, are nearly identical.

The iterations required to reach consensus, displayed in Figure 4.20, indicate that the number of iterations required for convergence is, for the most part, similar or greater than the number required by the MT D-MPC. This is possibly due to the large engine time-steps

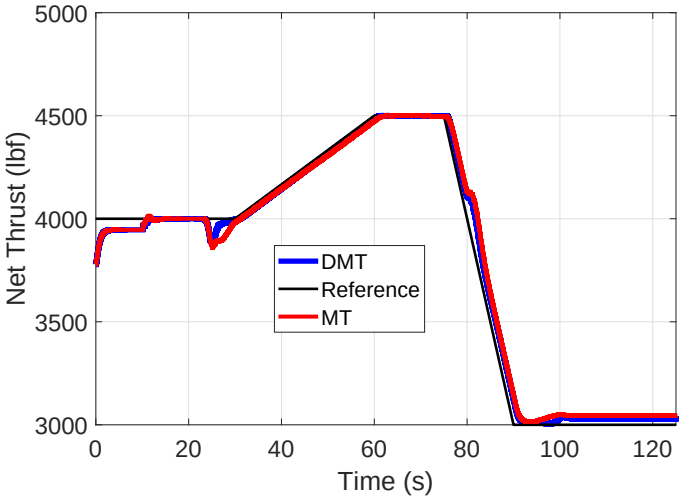

Figure 4.17: Thrust responses from the Simplified model as actuated by the MT (red) and DMT (blue) D-MPCs.

giving the engine MPC a horizon of only $n_h^e = 2$, meaning there is only one step without the heavy final state penalty P_e, set by the DARE solution.

Table 4.5: Statistical results of the timing studies done on the MT and DMT D-MPC algorithms.

Architecture	**Mean Time**	**Min**	**Max**
MT D-MPC	0.0357 s	0.0098 s	0.5507 s
DMT D-MPC	0.0730 s	0.0084 s	0.2951 s

A study on the computational time for each update for both algorithms was done using the MATLAB `tic-toc` functions. The time for each of the algorithms to reach a consensus for the simulation profile shown in Figures 4.14-4.19 was recorded after each coordinating time-step. These simulations were done on a Macbook Pro with an Intel Core i7-4980HQ CPU. A table of the statistical results is given in Table 4.5 and a histogram in Figure 4.21. The results are mixed, the DMT D-MPC has a mean computation time more than twice that of the MT D-MPC due to a second peak just under the 0.1 second/update mark. Examination of the time history of the computation times, in Figure 4.22, shows that this is caused by an increase in computation time from 80 to 125 seconds that corresponds to a similar raise in the iterations for the DMT D-MPC at those instances in Figure 4.20.

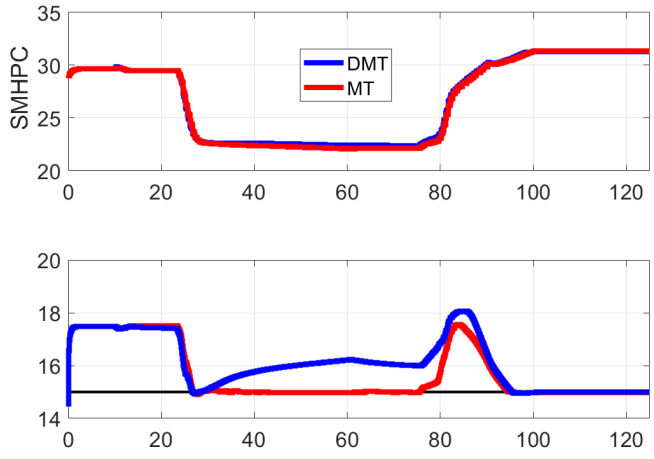

Figure 4.18: The compressor surge margin responses from the Simplified model in response to the MT (red) and DMT (blue) D-MPCs.

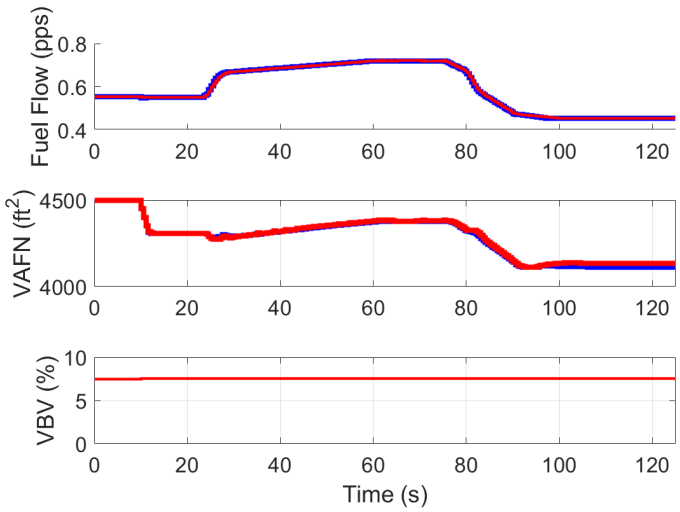

Figure 4.19: The engine control inputs from the MT (red) and DMT (blue) D-MPCs as applied to the Simplified model profile.

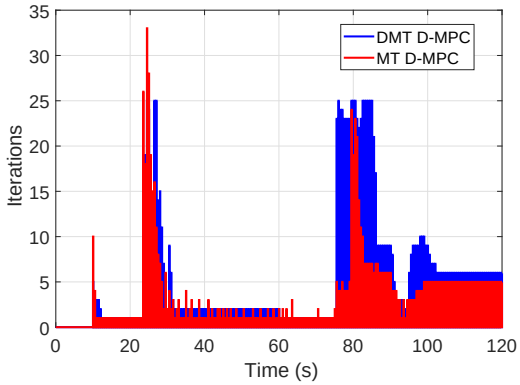

Figure 4.20: Time histories of the iterations required to reach consensus at each coordinated update by the MT (red) and DMT (blue) D-MPC algorithms.

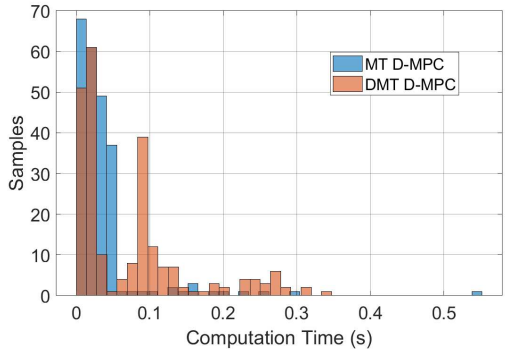

Figure 4.21: Histograms of computational times per consensus update of the MT (red) and DMT (blue) D-MPC algorithms, as applied to the Simplified model.

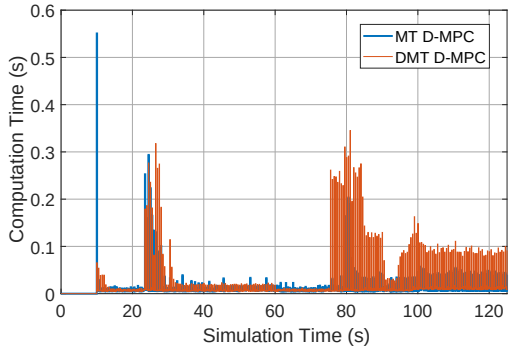

Figure 4.22: Time histories of the computation times per consensus update of the MT (red) and DMT (blue) D-MPC algorithms, as applied to the Simplified model.

4.5 Detailed Model

In this section, the Centralized, Decentralized, MT, and DMT architectures are applied to the Detailed model in simulation. The tunings for the MPCs were found with the Centralized MPC and are given in Table 4.6. The values for the MT and DMT parameters, as applied on the Detailed model, are given in Table 4.7.

Table 4.6: Tunings and key parameters for the Detailed model predictive controllers.

Variable	Description	Value	Variable	Description	Value
T_p	Power time step	10 ms	T_e	Engine time step	50 ms
Q_{thr}	Thrust penalty	10^{-9}	R_{FAR}	FAR change penalty	0.01
Q_{PL}	PL penalty	0.01	Q_V	Voltage reference penalty	10^{-3}
Q_{Batt}	Battery use penalty	$5 * 10^{-4}$	R_{PL}	PL change penalty	0.1
R_V	Voltage ref penalty	1	R_{sp}	Split ref penalty	1
R_{Batt}	Battery ref penalty	1	n_h (n_h^e)	Horizon length	30 (6)

Table 4.7: Parameter values for the ADMM related terms in the MT (left) and DMT (right) D-MPC strategies, as applied to the Detailed model.

Parameter	Value	Parameter	Value	Parameter	Value	Parameter	Value
ρ_{ep}	1e-7	ρ_{pe}	1e-7	ρ_{ep}	1e-7	ρ_{pe}	1e-7
ϵ_{ep}	2.5	ϵ_{pe}	2.5	ϵ_{ep}	2.5	ϵ_{pe}	2.5
λ	1			λ	1	μ	10

The simulation results are presented below; the Centralized MPC results are given in blue, MT D-MPC in red, DMT D-MPC in yellow, and the Decentralized MPC in purple. The engine thrust responses in Figure 4.23 show that, as expected, the controllers make two distinct groupings, with the two D-MPC strategies matching the Centralized MPC result while the Decentralized is the only controller unable to track the reference from 2 to 4 and 6 to 8 seconds. This is similar to how the coordinating and non-coordinating controllers grouped in Section 3.5, suggesting that the D-MPC architectures are able to consistently coordinate.

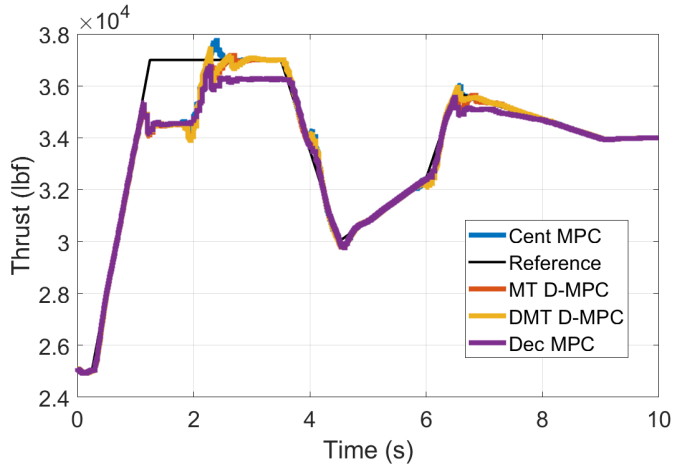

Figure 4.23: Thrust time histories from the four control strategies on the Detailed model.

The HP surge margin results, in Figure 4.24, demonstrate that the coordinating architectures are able to deactivate the constraint faster than the Decentralized MPC. This is most clear at the 2 to 4 and 6 to 8 second marks where the Decentralized MPC is riding the safety constraint, but it is also interesting to note that while the Centralized MPC is well above the constraints, and the two D-MPC strategies are only just a bit above it. Note that the SM LP never reaches its constraint and is not shown here.

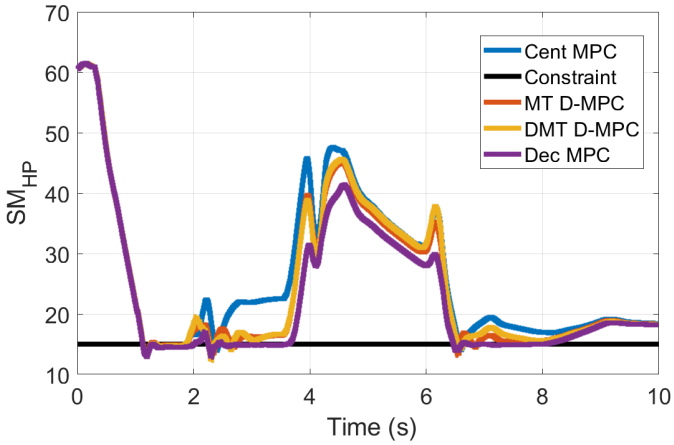

Figure 4.24: The HP compressor surge margin responses from the Detailed model to all four control architectures, with constraint shown in black.

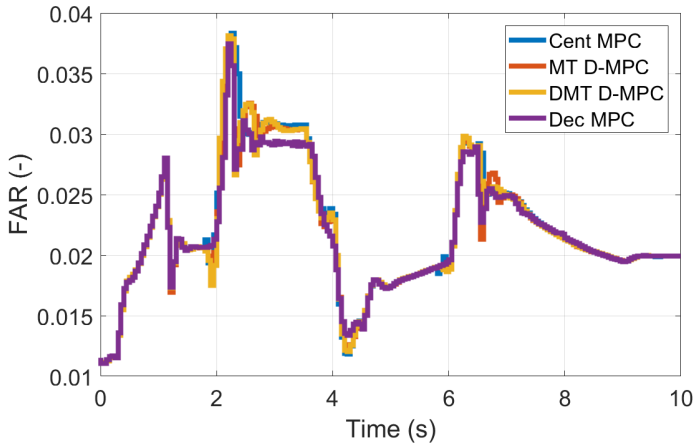

Figure 4.25: The FAR commands from the four MPC strategies on the Detailed model.

The key inputs affecting the engine dynamics in Figure 4.26, u_{FAR} from the engine controller and u_{sp} from the power controller, give similar results where the FAR gives the same grouping by coordination while the split factor gives a larger spread in the inputs.

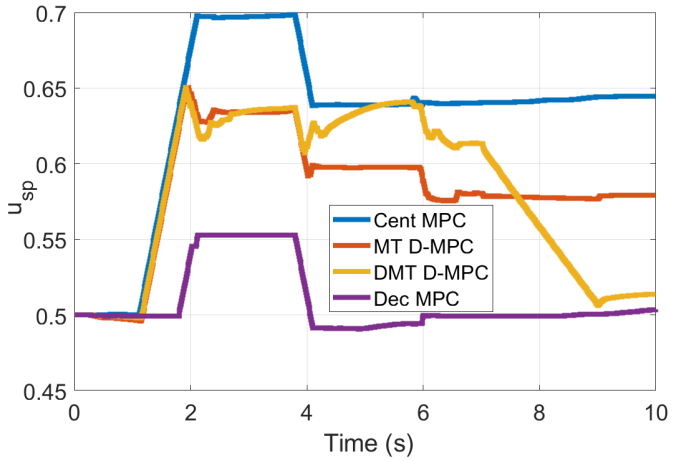

Figure 4.26: The split factor commands from the four MPC strategies on the Detailed model.

The power subsystem outputs, in Figure 4.27, show only minor variations between the controllers. The DMT does engage the battery pack more than the other controllers at 6 seconds, in Figure 4.28, but the reason is not clear.

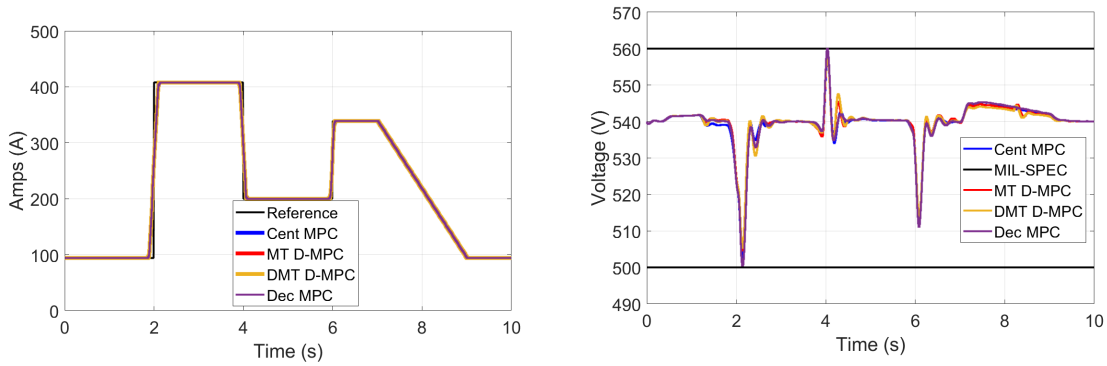

Figure 4.27: The power load current and HVDC voltage responses from the four control strategies. The MIL-SPEC voltage constraints are given in black.

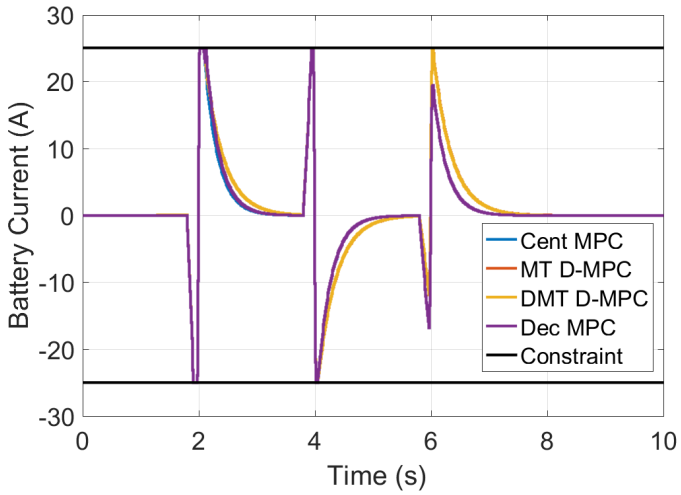

Figure 4.28: The battery commands from the four MPC strategies on the Detailed model.

Comparisons of the timings and iterations for the D-MPC strategies was done with the same methodology as in Section 4.4 for the Detailed scenario. The iterations in Figure 4.29 show that the DMT converges in fewer iterations across the board than the MT D-MPC, particularly visible from the 7 to 9 second range. The histogram shows that the DMT D-MPC has a lower computational time than the MT D-MPC, with no second peak unlike the DMT D-MPC results from the Simplified model. The statistical data presented in Table 4.8 supports this as well.

Table 4.8: Statistical information of the timing studies done on the distributed architectures for the Detailed model.

Architecture	**Mean Time**	**Min**	**Max**
MT D-MPC	0.7285 s	0.0717 s	4.649 s
DMT D-MPC	0.3129 s	0.0641 s	3.129 s

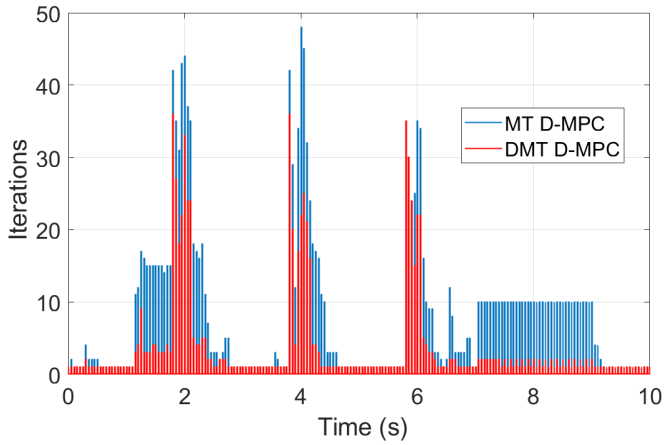

Figure 4.29: Time history for the iterations required for convergence of the distributed algorithms applied to the Detailed model.

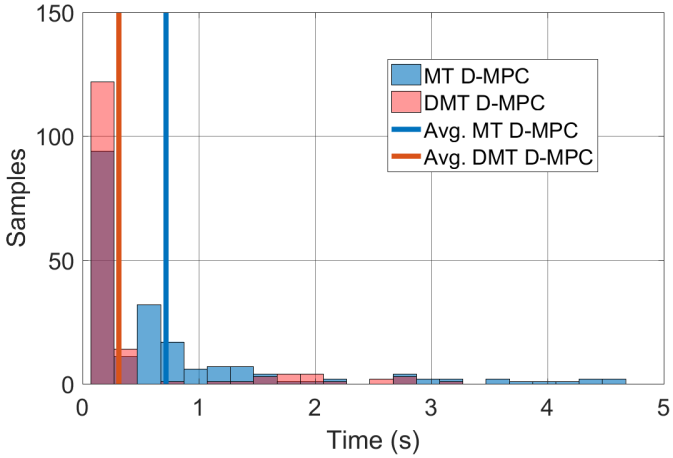

Figure 4.30: Histogram of the ADMM coordinating computation times over the simulation with average computation times for both algorithms shown as a vertical line.

4.5.1 Robustness to Un-coordinated Reference Changes

A case study for the robustness of the algorithms in response to unforeseen changes in the references was performed. The power load and thrust references are unexpectedly shifted back to their initial set points at $t = 2.11\ s$. This requires the power controller to react for a period of $0.04\ s$ before the next chance to coordinate with the engine controller. The power load responses in Figure 4.31 were all identical due to the high penalty on tracking it. The voltage bus responses in Figure 4.32 shows that the three coordinating controllers have little problem in holding the Mil-Spec constraint while the Decentralized MPC violates it at roughly 2.25 seconds.

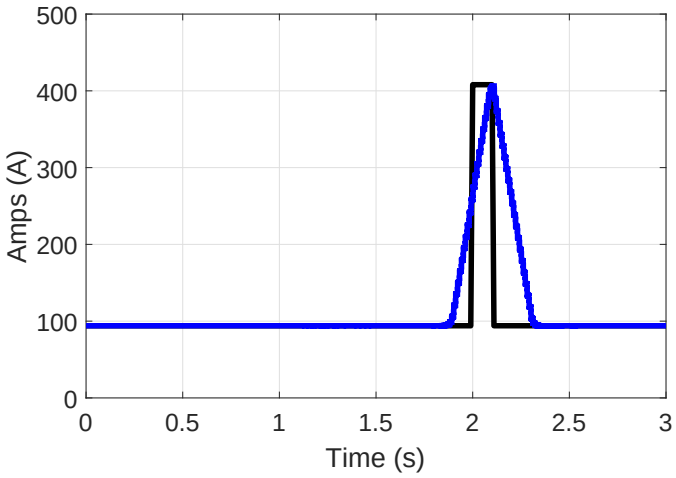

Figure 4.31: Time histories of the CPL of the four controllers on the Detailed model with an unexpected reference drop. The results all coincide thus appear as one signal.

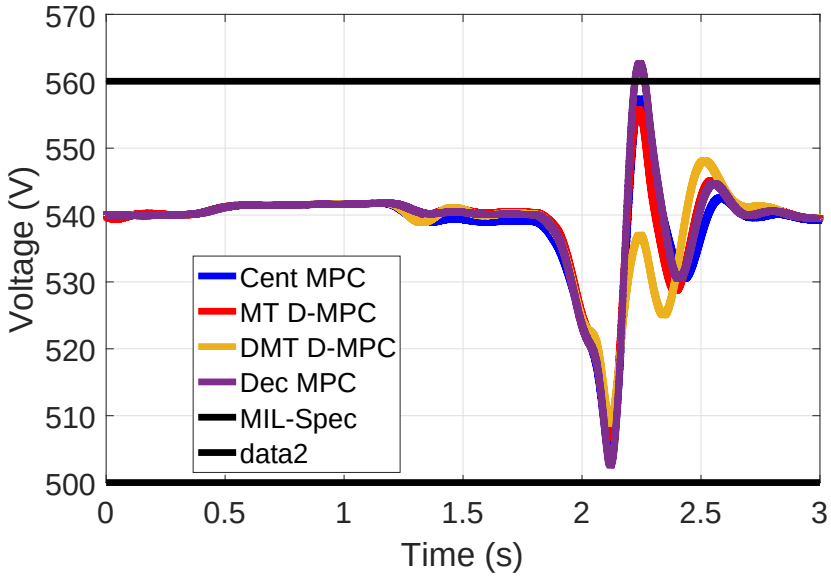

Figure 4.32: Voltage responses of the four controllers on the Detailed model with an unexpected reference drop.

The battery and split factor commands in Figure 4.33 illustrate a similar spread in the distribution of the generator power draw that was present in the nominal case in Figure 4.26.

The engine thrust and HP compressor surge margins, plotted in Figure 4.34, demonstrates that all control architectures are able to maintain stability after the drop. The Decentralized MPC has the smallest violation of the surge margin at 2.25 seconds; this is possibly

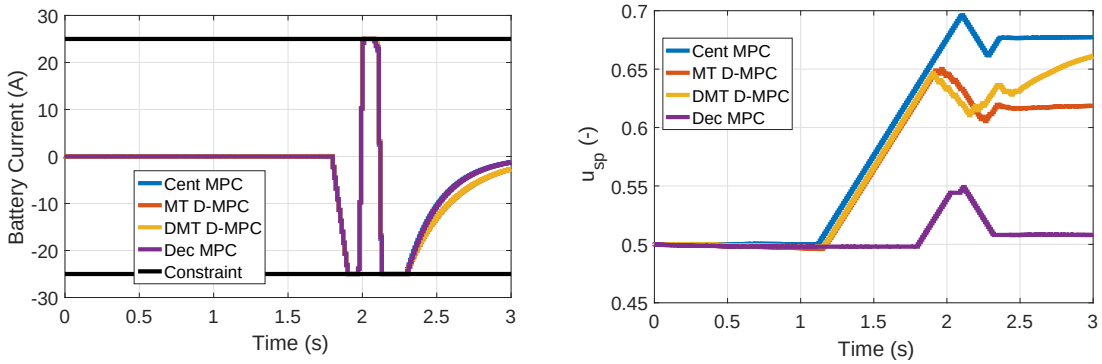

Figure 4.33: Battery current (Left) and generator power split factor (Right) commands from the four architectures during the reference drop case on the Detailed model.

due to the engine not having as much reliance on the power draw on the HP shaft to maintain the constraint. This is shown by the Centralized MPC having the largest constraint violation and a split factor close to 0.7, 70% of the generator power came from the HP shaft while the Decentralized was near a 50% draw, thus the sudden drop in power drawn had a smaller impact. This is supported by the FAR commands in Figure 4.35, where at 2.25 the Decentralized MP has the lowest fuel flow. The iterations required by the D-MPC strategies in Figure 4.36 show that the DMT still requires fewer iterations than the MT, but the sudden change in references does not increase the overall iterations required.

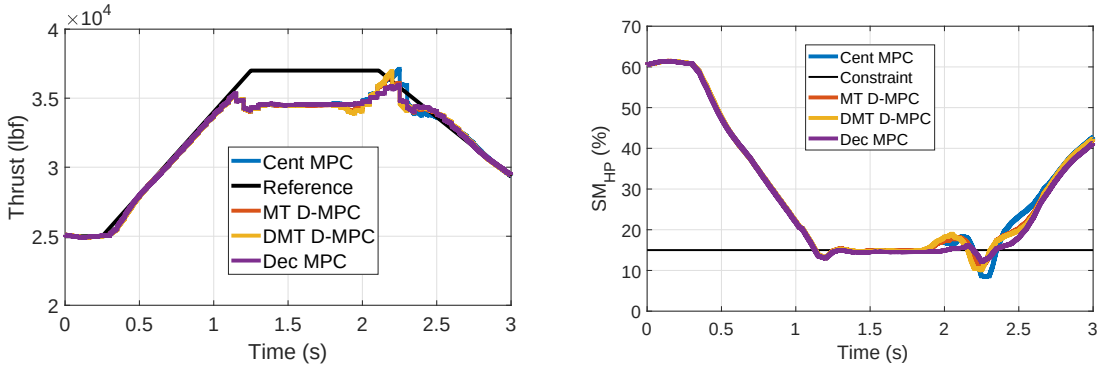

Figure 4.34: Reference drop case responses on the engine thrust and high pressure compressor surge margin by the four controllers on the Detailed model.

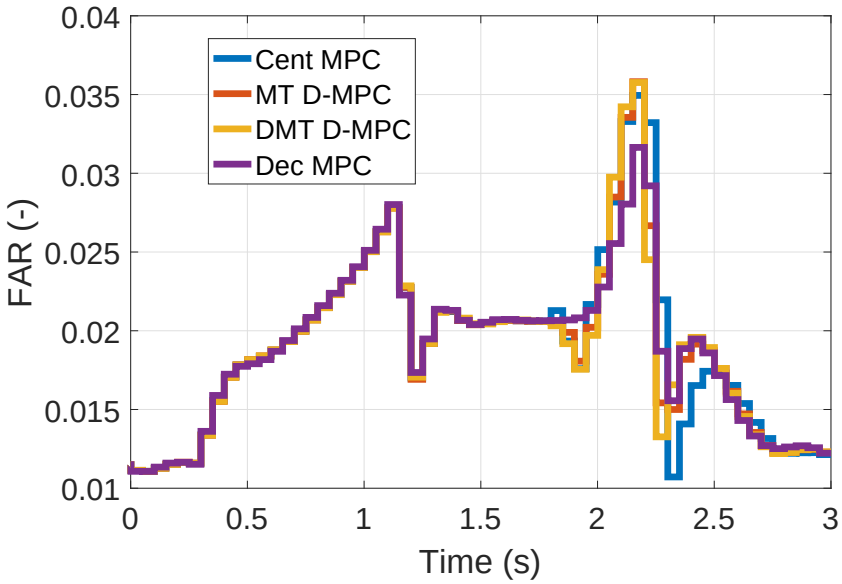

Figure 4.35: Fuel-to-air ratio inputs from all architectures on the Detailed model with reference drop.

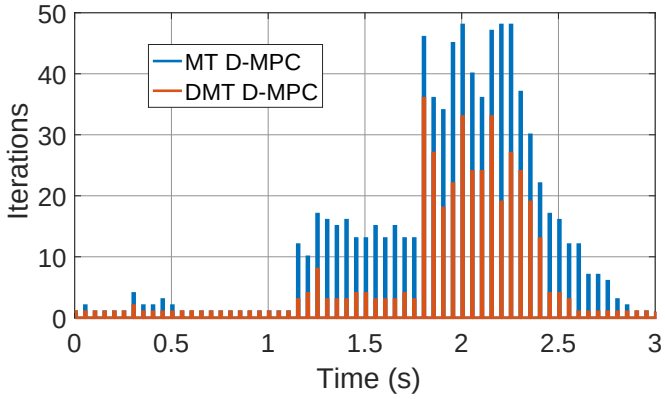

Figure 4.36: Iterations required for convergence of the D-MPC algorithms during the Detailed model reference drop case.

4.6 Discussion

This chapter presented the MT and DMT D-MPC architectures for coordination of a MEA turbojet and microgrid controllers. Simulations demonstrated the ability of the control schemes to closely match the performance of the Centralized MPC, despite the imposition of privacy requirements and multiple time-scale considerations. The two distributed architectures were successful in coordinating the power draw from the generators in order to improve the ability of the engine to track given thrust references while enforcing compressor surge margin constraints, despite the added challenges.

Down-sampling the interactions to the engine time-scale reduced the communication volume by reducing the size of the vectors that needed to be broadcast. This makes the strategy more robust to communication bandwidth constraints while the simulations show that the performance was not greatly effected. For the Detailed case, this reduced both the computation time and the iterations required by the controller. However, the Simplified case had the opposite result, although this is possibly being due to the DMT D-MPC not being fully optimized for that case as a bimodal response can be seen in the calculation times. Applications of the algorithms may need to limit the number of iterations or the computation time of the algorithm, producing a sub-optimal solution but one that can guarantee a control solution at each update without computational overruns.

The D-MPC control strategies presented were designed for tracking and constraint handling through coordination and have not been optimized with respect to computations. For instance, the optimization steps are based on forming and numerically solving the underlying quadratic programming problem using `quadprog.m` rather than explicitly using quadratic programming solvers tailored for MPC. Techniques such as code optimization, compiling the controller as a mex function, leveraging a solver designed for predictive controllers, and computing a fixed number of iterations at each joint update would likely enable real-time implementation of the controller; see [105] for more details on these techniques.

CHAPTER 5

Markov Chain Mission Paths and Stochastic MPC

This chapter proposes a model predictive control (MPC) strategy for managing stochastic reference profiles in the More Electric Aircraft (MEA) engine-power system. A Markov chain is used to represent the MEA mission profile with each state covering a stage in the mission and the probabilistic transitions between states representing the mission progression. Scenario Trees of future thrust and power load references with associated probabilities are constructed based on future pathways of the Markov chain and passed to a Stochastic Model Predictive Controller (S-MPC). The S-MPC uses a scenario based formulation for optimize over a probability weighted average of the cost function while constraints are enforced over all possibilities. The tight couplings in the subsystem dynamics and the uncertainty in the references over the horizon require careful consideration for safe and acceptable performance from the MEA control strategy. Simulations on the Detailed model of the MEA demonstrate the ability of the Scenario Based S-MPC to closely match the performance of an MPC with perfect preview of the future reference profiles and outperforms an MPC given no preview.

Statistical information is leveraged by S-MPC methods to provide predictive feedback control that provides some guarantee of stability, reliability, and performance in the presence of uncertainty or random disturbances. Surveys of S-MPC strategies can be found in [106, 107]. Early attempts to incorporate robustness to disturbances in MPC included the Min-Max MPC, where the controller minimizes the cost function while accounting for the worst-case disturbance scenario [108]. This basic strategy requires optimization over a only single scenario, but produces a very conservative solution that does not account for the actual probability of the worst case scenario. If the disturbances have well characterized statistical properties, chance constrained S-MPC can be applied [109]. Instead of requiring output constraints to be enforced as $y \leq \bar{y}$, they are instead formulated to enforce a probability that the constraint is met, $Pr(y \leq \bar{y}) \geq a$, where $a \in (0, 1)$ is a

design parameter for how strictly the constraint should be enforced. Stochastic problems are not always tractable and sampling methods may be required in order to reach a control solution [110]. One approximation is the Scenario Based S-MPC that samples possible realizations of a continuous distribution of potential futures and optimizes for those cases [111, 112]. Typically, Scenario Based S-MPC minimizes the probability weighted cost of the sampled scenarios and enforces constraints over all of them. The Scenario Tree variant of Scenario Based S-MPC used in the work presented in this chapter was proposed in [113] and further refined for application to transmission control in [114]. In this method, discrete stochastic models of the disturbance are incorporated in the controller optimization as a Scenario Tree originating from the current system state and branching out to cover the possible future states of the system. See Figure 5.1 for a diagram of the control strategy.

This chapter is laid out as follows. In Section 5.1, the Scenario Based S-MPC applied to the MEA system is presented. Section 5.2 describes the assumed mission profile including the Markov chain states, their transition properties, and how the reference Scenario Trees for optimization are generated. The control formulation for handling stochastic references on the MEA system is then demonstrated through Simulations on the Detailed model, including comparisons with a MPC with no trajectory information and one with perfect knowledge of the future. Additionally, a basic statistical analysis of all three controllers is performed with regards to tracking capability and constraint enforcement. The chapter is then concluded with a discussion of the results.

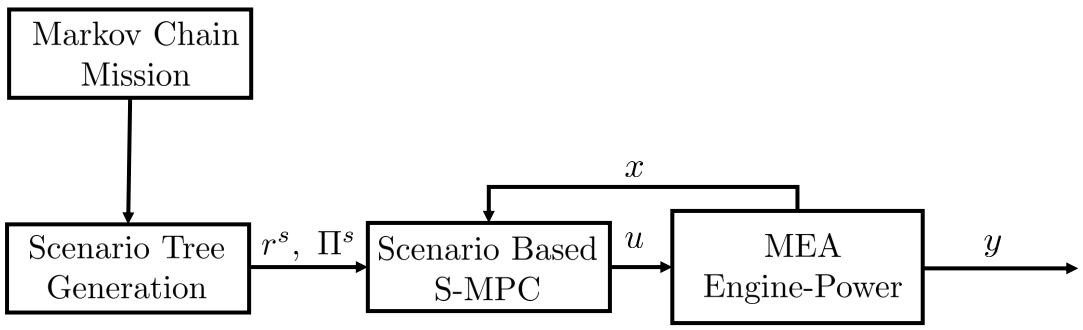

Figure 5.1: Control strategy presented in this chapter. Scenario trees are generated from the Markov chain mission model as a set of references, r^s, with associated probabilities, Π^s. The Scenario Based S-MPC optimizes for the control input, u, while accounting for the current system state, x, and the potential mission pathways.

5.1 Scenario Based S-MPC

The Scenario Based S-MPC considers a set of scenarios, S, to compute a control solution minimizing the expected value of the cost functions for each scenario over the horizon while enforcing constraints for every case, regardless of their likelihood. The control action at the root node of the Scenario Tree is then applied to the input of the system. A review of the key variables for the rate-based MPC formulation and key terms for the Scenario Based S-MPC are given in Table 5.1. Note that a centralized formulation is given, so the subsystem subscripts from the previous Chapters are dropped.

Table 5.1: Key variables for Chapter 5.

Variable	Description
$x^s,\ \Delta x^s$	States and change in states for scenario s
$\bar{x}^s$	Extended states for scenario s for rate-based MPC
$u^s,\ \Delta u^s$	Inputs and change in inputs of scenario s
y^s	Outputs for scenario s
r^s	References for scenario s
Π^s	Probability of scenario s

The Scenario Based S-MPC is formulated as a dynamic optimization problem over a horizon of length n_h as

$$\min_{\Delta u^s} \sum_{s\in\mathcal{S}} \Pi^s J(\Delta u^s, \bar{x}^s), \tag{5.1a}$$

$$\text{subject to } \bar{x}^s(k+1) = \bar{A}\bar{x}^s(k) + \bar{B}\Delta u^s(k) + \bar{R}\Delta r^s(k), \tag{5.1b}$$

$$\Delta u^s(k) \in \mathcal{D},\ k = 0, \cdots, n_h - 1, \tag{5.1c}$$

$$\Delta u^s_e(k) = 0,\ \text{if } k \notin K_e, \tag{5.1d}$$

$$u^s(k) \in \mathcal{U},\ k = 0, \cdots, n_h - 1, \tag{5.1e}$$

$$y^s(k) \in \mathcal{Y},\ k = 1, \cdots, n_h, \tag{5.1f}$$

$$\text{given } x^s(0),\ u^s(-1) \tag{5.1g}$$

$$u^s(k) = u^l(k),\ \text{for } s, l \in \mathcal{S},\ \text{if } r^s(i) = r^l(i),\ i = 0, ..., k. \tag{5.1h}$$

The cost function, in (5.1a), is a probability weighted variant of the penalty functions from

previous chapters,

$$J(\Delta u, \bar{x}) = \sum_{k=0}^{n_h-1} [\bar{x}^T(k)Q\bar{x}(k) + \Delta u^T(k)R\Delta u(k)] + \bar{x}^T(n_h)P\bar{x}(n_h), \tag{5.2}$$

where Q is a semi-positive definite matrix that penalizes for tracking error on certain inputs and outputs, R is a positive definite matrix penalizing for input changes, and P is the terminal penalty cost, constructed by the DARE solution as discussed in Section 3.2. The input, input rate, and output constraints from lines (5.1c) to (5.1f) are imposed across all scenarios with no considerations for probability. The condition in (5.1d) represents move blocking of the engine inputs, accounting for the engine control actions updating at a slower rate than the power control actions, 100 msec to 10 msec respectively. Finally, the consistency constraint in (5.1h) enforces causality by ensuring that control trajectories are equivalent across the scenarios until their mission states diverge.

5.2 Mission Profile

For stochastic MEA control, the scenarios are predicted using a Markov chain model of a reconnaissance flight, a diagram of which is given in Figure 5.2, the states of which represent stages in the mission and are associated with desired thrust and electrical power values. The stages are based on the suggested military aircraft mission profile from [115]. The mission begins at take-off from a home base and is followed by a climb to cruise altitude. Cruise flight is maintained until approaching the targeted air space. The aircraft then dashes into the area by accelerating in order to increase speed and reduce the likelihood of any effective response from the opposition. Once near points of interest for the mission, the aircraft enters a standby phase where thrust rises slightly and the power load increases due to mission critical loads, such as imaging and radar instruments. During this phase, there is a possibility that threats, such as an anti-air missile, will imperil the MEA. In such an event, the MEA must enact countermeasures such as rapid turns, sensor jamming, or energy weapon shots, leading to large bursts of both thrust and power loads. After the threat is dispatched, the aircraft returns to the standby phase. After sufficient data has been collected, the aircraft dashes out and finally cruises back to the home base. As the interest of this work is in the stochastic portions of the mission, only the states during target engagement are considered, that is, from Cruise In just until after a few seconds into Return Cruise.

The mission state, m, is assigned a numerical value from the possible set of states of

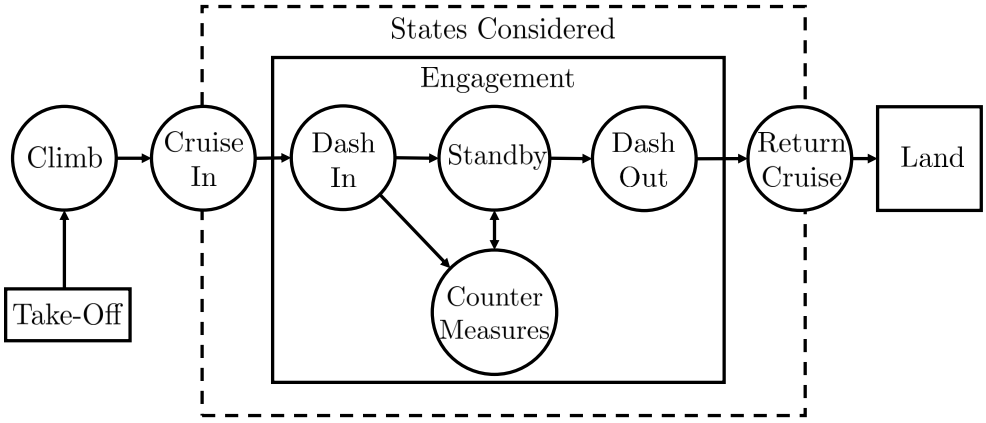

Figure 5.2: The Markov chain representation of the MEA mission with states labeled and transitions shown. States within the dotted square are considered in this work and those within the solid square occur during engagement with a hostile area.

$\mathcal{M} = \{1,\ 2,\ 3,\ 4,\ 5,\ 6\}$, where the states in order are Cruise In, Dash In, Standby, Counter Measures, Dash Out, and Return Cruise. The probabilities of transitioning between states is $\pi^{i,j};\ i,\ j \in \mathcal{M}$ and are given in Table 5.2, where i is the row and current state while j is the column and potential next state. Dwell times are enforced after transitions between certain states in order to allow for the references to settle to their desired values, shown in Table 5.3, meaning that the Markov chain incorporates memory in it's transitions. During these dwell times, the transition probability matrix is an identity matrix, that is $\pi^{i,i} = 1$ and $\pi^{i,j} = 0, \forall i,\ j \in \mathcal{M},\ j \neq i$. Once the Cruise Out state has been reached, that is $m = 6$, and two seconds have passed, the mission is considered complete. The mission state is updated at a time-steps of T_{miss}. In this work, the mission state transitions are treated as static probabilities. In a real world application, the states would transition due to internal logic and external stimuli. For example, Cruise in to Dash in would occur once a GPS navigational computer has determined that the aircraft has reached a predetermined threshold.

5.2.1 Reference Trajectory Generation

Each mission state is associated with a desired reference, $\hat{r}^m$, and a rate limit, $\Delta\bar{r}^m$ which are used to generate scenario reference profiles. The scenario generation is performed periodically every T_{miss} sec and over the time window of length of $T_{miss}+n_hT_{MPC}$ sec into the future, where $T_{miss} \geq n_hT_{MPC}$ is the time period between mission state updates, T_{MPC} is the update period of the MPC controller (**??**) and an integer fraction of T_{miss}. Let $\hat{r}^{cur}$ and $\Delta\bar{r}^{cur}$ correspond to the current state of the mission and $\hat{r}^s$ and $\Delta\bar{r}^s$ correspond to the

Table 5.2: Transition probabilities from current state (row) to next state (column) at transition step.

Name	**State**	1	2	3	4	5	6
Cruise In	1	0	1	0	0	0	0
Dash In	2	0	0.4	0.5	0.1	0	0
Standby	3	0	0	0.4	0.4	0.2	0
Countermeasures	4	0	0	0.7	0.3	0	0
Dash Out	5	0	0	0	0	0	1
Cruise Out	6	0	0	0	0	0	1

Table 5.3: Dwell times enforced for transitions from previous state (row) to current state (column), in seconds.

Name	**State**	1	2	3	4	5	6
Cruise In	1	0	1.5	0	0	0	0
Dash In	2	0	0	0	0	0	0
Standby	3	0	0	0	0	1.5	0
Countermeasures	4	0	0	1	0	0	0
Dash Out	5	0	0	0	0	0	1.5
Cruise Out	6	0	0	0	0	0	0

potential next state of the mission $s \in S$, determined according to the possible transitions of the Markov Chain. The reference scenarios, $r^s, s \in S$ are generated according to the following procedure:

$$r^s(i) = \begin{cases} r^s(i-1) + \Delta\bar{r}^{cur}, \text{ if } r^s(i-1) < \hat{r}^{cur} - \Delta\bar{r}^{cur}, \\ r^s(i-1) - \Delta\bar{r}^{cur}, \text{ if } r^s(i-1) > \hat{r}^{cur} + \Delta\bar{r}^{cur}, \\ \hat{r}^{cur}, \text{ otherwise,} \end{cases} \tag{5.3}$$

for $i = 1, \ldots, (T_{miss}/T_{MPC})$ and

$$r^s(i) = \begin{cases} r^s(i-1) + \Delta\bar{r}^{s}, \text{ if } r^s(i-1) < \hat{r}^{s} - \Delta\bar{r}^{s}, \\ r^s(i-1) - \Delta\bar{r}^{s}, \text{ if } r^s(i-1) > \hat{r}^{s} + \Delta\bar{r}^{s}, \\ r^s(i-1) = \hat{r}^{s}, \text{ otherwise,} \end{cases} \tag{5.4}$$

for $i = (T_{miss}/T_{MPC}+1), \ldots, (T_{miss}/T_{MPC}+n_h)$ and $s \in \mathcal{S}$. Here $i \in \{0, \cdots, T_{miss}/T_{MPC}\}$ refers to the time instant along the reference scenario generation window (that is different than the MPC horizon). At $i = 0$, $r^s(0)$ is set to the actual reference at the time instant

scenario generation is performed as computed in the previous reference scenario generation window. As there could be at most a single transition over the MPC horizon, the probability of each trajectory is

$$\Pi^s = \pi^{cur,s}. \tag{5.5}$$

The above scenario generation process can be extended to include more mission states, e.g., Dash In at different thrust and electrical powers levels. Such extensions are left to future research.

An illustration of the reference scenario generation and usage by the S-MPC is given in Figure 5.3 for three possible pathways. Once the scenarios are constructed, they can be used for control trajectory optimization by the Scenario Based S-MPC.

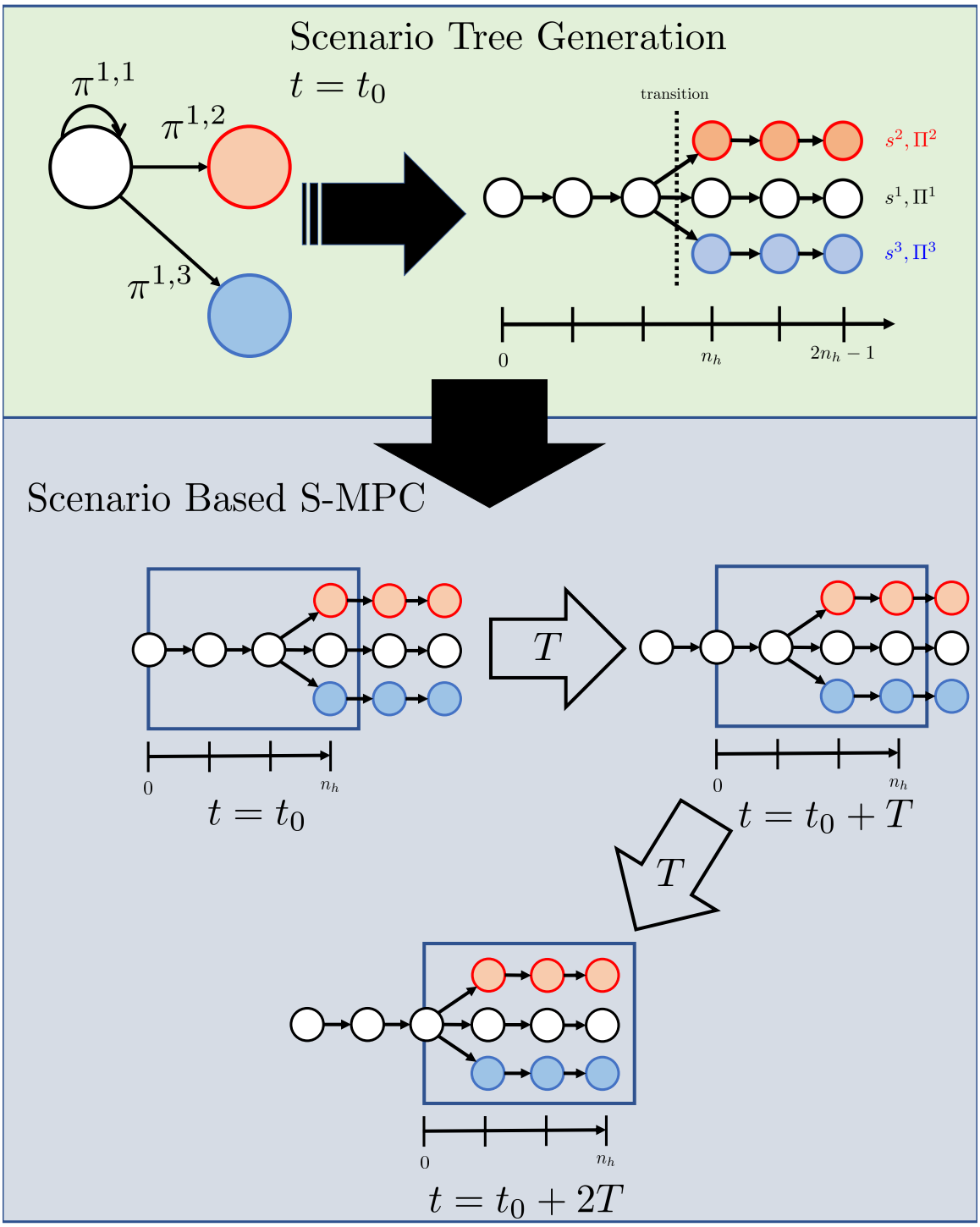

Figure 5.3: Illustration of a Scenario Tree generated from a discrete Markov chain with three potential transitions at the current state. The tree is then passed to the S-MPC where portions of it are considered over the horizon of the optimization problem at each time step, displayed as a box on the tree. The horizon advances one node of the tree at each controller update.

5.3 Simulations

In this section, the Markov chain mission representation with Scenario Based S-MPC strategy is demonstrated through simulation on the Detailed model. Twenty seeds were randomly chosen in order to cover a wide range of possible realizations of the discrete Markov model of the mission in Section 5.2. The state trajectories from these seeds are in Figure 5.4 and the resulting thrust and load reference trajectories are given in Figures 5.5 and 5.6, respectively.

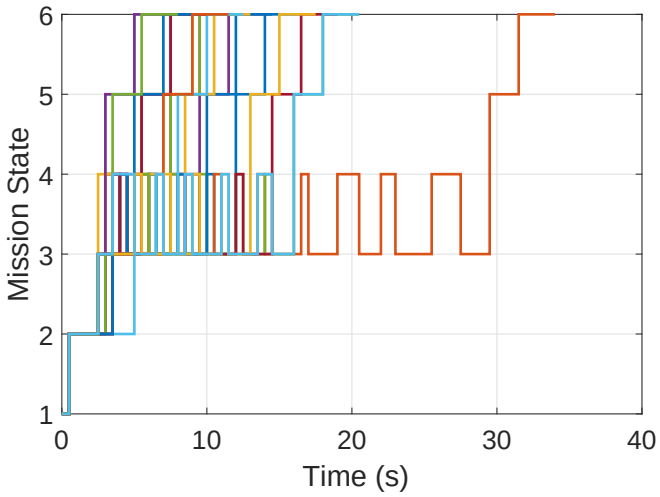

Figure 5.4: Mission states for the twenty seeded runs starting from state 1 (Cruise in) until having reach state 6 (Cruise Out) for two seconds.

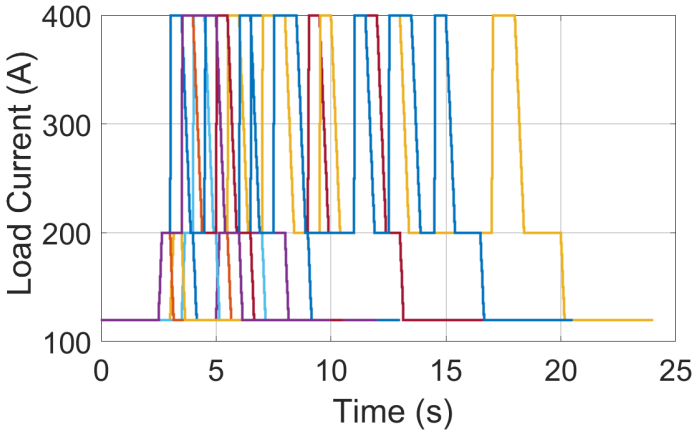

Figure 5.5: Power load reference time histories from the twenty seeded mission trajectories.

The performance of the proposed strategy is compared against that of a simple rate-based MPC given no preview of the references and that of a rate-based MPC with perfect

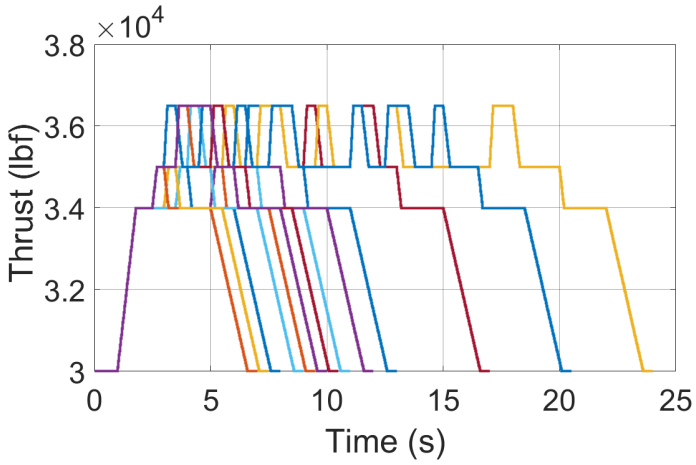

Figure 5.6: Thrust reference realization traces from the twenty seeded mission trajectories.

knowledge of the future mission state over the prediction horizon. The no-preview MPC is expected to have the worst performance due to the lack of information, but is computationally simpler to solve than the Scenario Based S-MPC as it only considers a single scenario. The perfect preview MPC is given exact knowledge of the reference trajectories and also only requires a single scenario. However, it is non-causal and simply represents the theoretical upper limit on how well a predictive control strategy could perform one this problem with respect to the given tunings and control models. The controllers share the same parameters, presented in Table 5.4. The simulation ends two seconds after reaching Cruise Out flight. The problem solutions are computed using Matlab's `quadprog.m` solver.

The ability of the controllers to track the given references is measured through the root mean square (RMS) of the tracking error. Samples of the error are taken every hundredth of a second and the error of the RMS is calculated as

$$e_{RMS} = \sqrt{\frac{e(1)^2 + e(2)^2 + \cdots + e(n_{samples})^2}{n_{samples}}}, \tag{5.6}$$

where $n_{samples}$ is the total number of samples taken over the simulation. The RMS value after each run is recorded, the average and maximum values for each over the twenty seeded cases are given in Table 5.5. The MPC without preview is outperformed by the other two controllers in tracking of both references. The S-MPC is able to slightly outperform the Perfect Preview MPC in thrust tracking, with an average RMS of 7.18 to 8.02; but is surpassed in power load tracking. This is further examined below.

Parameter	Symbol	Value
Mission Stages		
Mission Update Rate	T_{miss}	0.5 s
Desired References	$\hat{r}^1$	$3 \cdot 10^4$ lbf, 120 A
(Thrust, Power Load)	$\hat{r}^2$	$3.4 \cdot 10^4$ lbf, 120 A
	$\hat{r}^3$	$3.5 \cdot 10^4$ lbf, 200 A
	$\hat{r}^4$	$3.65 \cdot 10^4$ lbf, 400 A
	$\hat{r}^5$	$3.4 \cdot 10^4$ lbf, 120 A
	$\hat{r}^6$	$3 \cdot 10^4$ lbf, 120 A
Ref Change Rates	$\Delta\bar{r}_{1,\ 2,\ 3,\ 5,\ 6}$	$5 \cdot 10^3$ lbf/s, 5 A/s
(Thrust, Power Load)	$\Delta\bar{r}_4$	$1 \cdot 10^4$ lbf/s, 50 A/s
S-MPC		
MPC Update Rate	T_{MPC}	0.01 s
MPC Horizon	n	30 steps
Error Penalty	Q_e	diag$(10^{-6},\ 1,\ 10^{-6})$ (Thrust, Load, Bus Voltage)
Control Penalty (Only on Batt)	Q_{Batt}	10^{-4}
Control Penalty	R	diag$(0.25,\ 10,\ 10,\ 10,\ 1)$ (Δu_{FAR}, Δu_{HVDC}, Δu_{sp}, Δu_{Batt}, Δu_{PL})
FAR Constraint	$\mathbb{U}_{FAR}$	$0.01 \leq u_{FAR} \leq 0.05$
Battery Current Constraint	$\mathbb{U}_{Batt}$	$-30\ A \leq u_{Batt} \leq 30\ A$
Generator Split Constraint	$\mathbb{U}_{sp}$	$0.1 \leq u_{sp} \leq 0.9$
Nominal Bus Voltage	r_{HVDC}	540 V
HP Surge Constraint	$c_{SM,HP}$	15 %
LP Surge Constraint	$c_{SM,HP}$	20 %
Bus Constraints	$\mathbb{Y}_{HVDC}$	$500\ V \leq y_{HVDC} \leq 560\ V$

Table 5.4: Key parameters and tunings for the mission stages and the S-MPC .

Table 5.5: Statistical data on the tracking error RMS for the three controllers over the twenty seeded simulations.

Controller	Thrust (lbf)		Power Load (A)	
	Avg	Max	Avg	Max
S-MPC	7.18	11.76	0.15	0.18
No-Preview MPC	11.26	18.00	0.17	0.30
Perf-Preview MPC	8.02	13.16	0.10	0.16

Maintaining the imposed output constraints on the surge margins and bus voltage is critical for the operation of the MEA engine-power system. Constraint enforcement performance is measured by the largest deviation of the high pressure compressor surge margin (HP SM) and bus voltage constraints during the course of the simulation. The low pressure compressor surge margin is not violated in any of the seeded cases. The maximum deviation after each run was recorded, the average and maximum values over the twenty simulations are presented in Table 5.6. As expected, without preview the MPC has greatly increased violations of the HP SM constraint compared to the other controllers and, in one case, is within 3% of stalling the compressor. All controllers are able enforce the Mil-Spec required constraints; recall from Section 2.1.2 that the extrapolation allows short deviations to the larger range of 400-660 V, and these results are well within.

Table 5.6: Statistical data on the largest violation in response to the three controllers over the twenty seeded simulations.

Controller	HP Surge Margin (%)		Voltage (V)	
	Avg	Max	Avg	Max
S-MPC	1.8	2.02	0.86	3.22
No-Preview MPC	6.19	12.46	1.57	8.02
Perf-Preview MPC	1.64	1.73	1.57	4.38

A deeper examination of one of these twenty cases is performed. This case was chosen as it had multiple countermeasure steps of varying time length, but not so many as to compress the plots and reduce readability. The CPL traces in Figure 5.7 displays an interesting spiking behavior from the Scenario Based S-MPC just before each potential change in the power load request. This is interpreted as being due to the relatively large penalty on tracking the power load requests and the possibility of dramatic increases at each mission state update. The detail blow-up in Figure 5.7 illustrates how this allows the S-MPC to nearly keep up with the perfect preview MPC while the MPC with no preview lags behind.

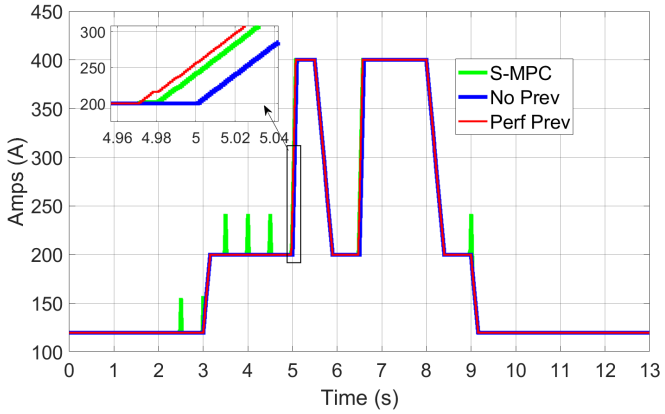

Figure 5.7: Time histories for the CPL current for all three controllers for the examined seed on the Detailed model.

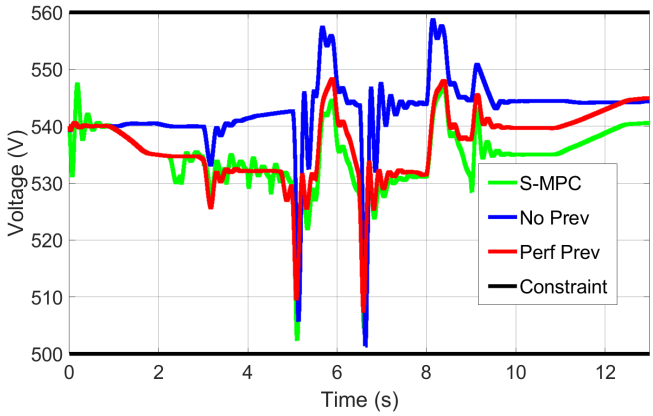

Figure 5.8: Bus voltage responses from all three controllers during the examined scenario on the Detailed model.

The bus voltage responses in Figure 5.8 show that, in this case, all controllers are able to maintain the constraints, while the S-MPC and Perfect Preview MPC share characteristics of their responses such as the ramp from 10 to 12 seconds. Note that the power load references are ramped and do not increase or decrease as dramatically as in the previous chapters, reducing the voltage deviations.

The thrust results in Figure 5.9 shows that the MPC without preview struggles to track the reference, with spikes near the transitions at 5 and 6.5 seconds as well as lagging behind the other controllers during ramps in the reference.

The MPC given perfect preview struggles to track the thrust reference profile from 3 to 5 seconds while the S-MPC is able to. The cause can be seen in the HP SM trace in Figure 5.11, where the perfect preview and no preview cases are up against the soft safety constraint. This is interpreted as being caused by the modeling mismatch disturbances

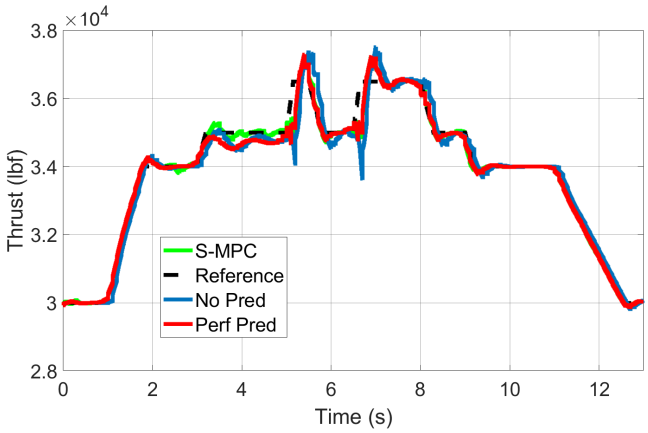

Figure 5.9: The thrust responses of the considered controllers during the examined seed on the Detailed model. The reference trajectory is shown as a dashed black line.

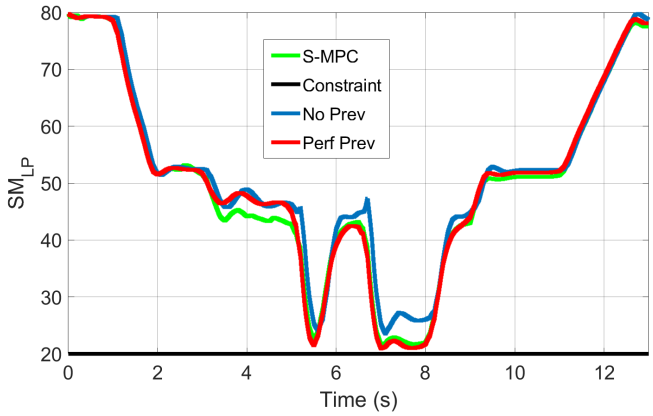

Figure 5.10: Low Pressure compressor surge margin response from the three controllers during the examined scenario.

impacting those two cases while the added conservatism of the Scenario Based S-MPC allows for that constraint to become inactive faster. The split factor in Figure 5.12 shows that having preview causes the controllers to adjust the balancing of the generator power extraction from the shafts earlier and to a larger degree than the reactive MPC with no preview.

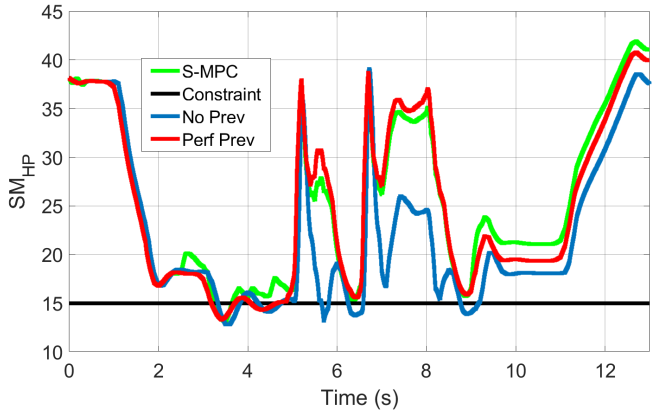

Figure 5.11: High Pressure compressor surge margin response from the three controllers during the examined scenario.

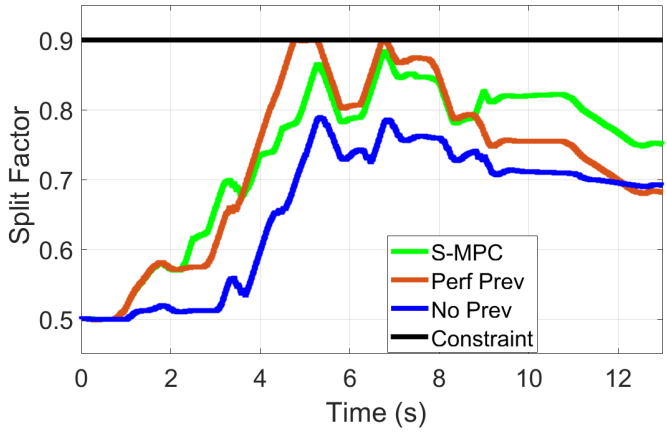

Figure 5.12: Time histories of the split factor commands from the controllers during the examined scenario on the Detailed model.

The battery power and state of charge traces in Figure 5.13, shows that at the times that the MPC with exact preview struggles with tracking the thrust reference, between 2.5 and 5 seconds, it is discharging the battery while the Scenario Based S-MPC is charging it. The impact of that change is on display in Figure 5.14,where the time histories of the generator torques are displayed. The Scenario Based S-MPC achieves a greater HP torque load than the other two controllers at that point in time by charging the battery; this slows down the HP shaft and allows the compressor surge to rise.

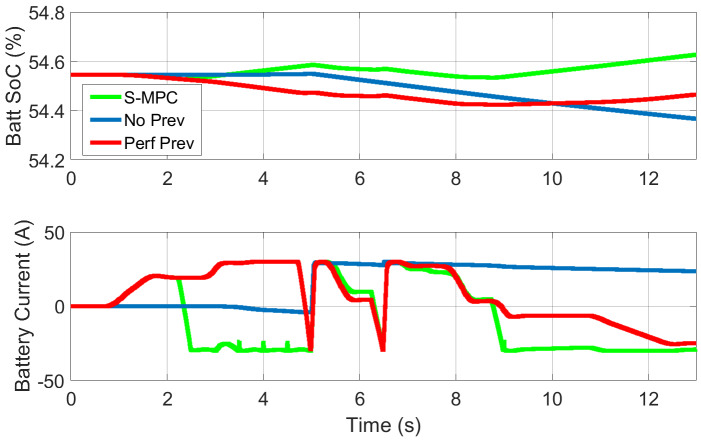

Figure 5.13: Time histories for the battery responses from the three controllers throughout the examined case.

5.4 Discussion

This chapter presented the application of a Scenario Based Stochastic MPC (S-MPC) to the constrained coordinated control of the propulsion and electrical power subsystems in a More Electric Aircraft (MEA) equipped with a dual core gas turbine engine and an electrical microgrid with two generators, a battery pack, a voltage bus and power loads. An approach based on representing the MEA mission using a Markov Chain has been proposed to generate scenarios of engine thrust and power load which are used by the S-MPC for control optimization. The simulation results on the nonlinear MEA model suggest that Scenario Based S-MPC is able to closely match responses of an MPC with perfect preview and outperform an MPC with no preview. More elaborate approaches to scenario generation and removal to avoid unnecessary conservatism will be pursued in future research.

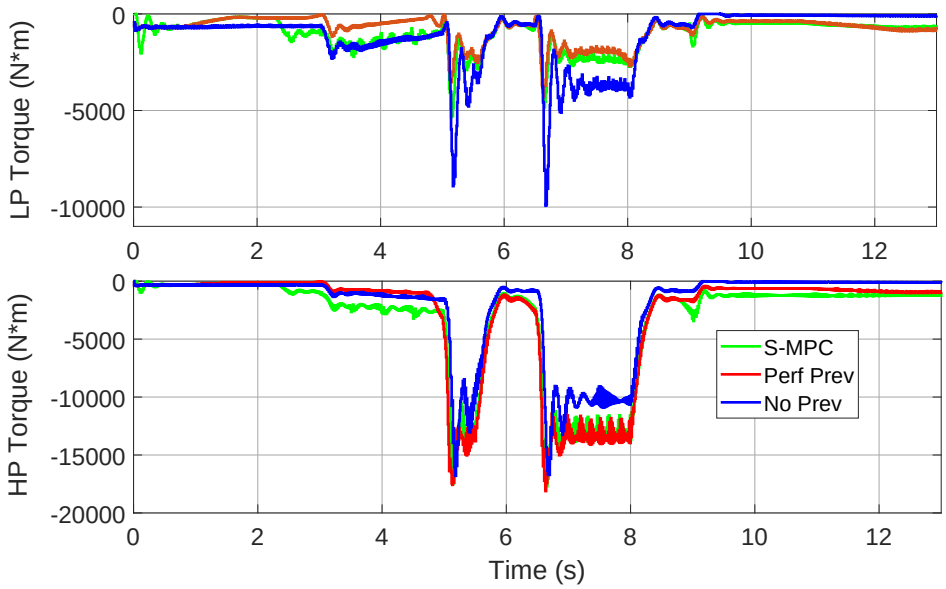

Figure 5.14: The torques applied to the shafts by the generators in response to the three controllers during the examined seed.

CHAPTER 6

Conclusions and Future Work

6.1 Conclusions

Improvements in power electronics and industry pressures are driving aircraft designs to become more electrified [4]. These More Electric Aircraft (MEA) designs include more extensive and complex electrical power distributions in order to address larger and faster power demands [5]. The engine and power subsystems of an MEA design require coordination of their interactions to achieve greater efficiency and reliability compared to modern designs. This thesis presented key developments in the pursuit of advanced predictive control strategies of an MEA to achieve improved performance while enforcing key constraints on inputs and states.

Chapter 2 defined the models for the MEA engine and power subsystems motivating the work. Fuel is burned in the engine to generate thrust and mechanical power in the aircraft. Electrical generators draw some of that power and supply energy to power loads through a voltage bus. A battery pack is used to help smooth transients in the bus voltage from changes in the power loads that are too fast for the generators. Two simulation models were synthesized for demonstrations of the control strategies. The Simplified model combined the AGTF30 concept engine developed by NASA [69] with a power flow representation of the microgrid for a high-level representation of the electrical dynamics for rapid testing of controllers and demonstration of concepts. The well studied Pratt and Whitney JT9D engine and circuitry based modeling of the electrical distribution composed the Detailed model for higher fidelity testing of the controllers. Both models share the objective of managing the engine and power subsystems in order to track references on thrust and electrical power while enforcing constraints on compressor surge and bus voltage excursions to ensure the safety of the aircraft and its components.

Chapter 3 determined that effective MEA control could be achieved with disturbance rejection, coordination of the subsystems, and anticipation of changes in the power load.

Rate-based MPC was able to overcome model mismatch between the linear control models and the nonlinear system to achieve offset free tracking of the references. Coordination of the subsystems assisted the engine in tracking thrust commands in the presence of compressor surge constraints by balancing the power drawn by the generators from the high or low pressure shafts of the engine. Anticipation of power load changes was demonstrated to be beneficial in maintaining bus voltage constraints by giving the controllers time to ramp up the generators of the microgrid.

Chapter 4 developed a distributed control scheme to accommodate subsystem privacy and controllers operating at differing time scales. Consensus on the interactions between the subsystems over a horizon was achieved using the Alternating Direction Method of Multipliers on instances when both controllers were updating. The resulting terms inform the power subsystem optimization to retain considerations for the engine subsystem. Down-sampling of the interactions to the engine time-scale was considered in an extension that reduced the communication volume between the controllers. Simulations demonstrated that the strategies performed similarly to a centralized controller given full knowledge of the states and authority over the inputs of the subsystems while outperforming a decentralized solution.

Chapter 5 considered stochastic preview of the references in the controller prediction. The scenario trees of the references are based on a Markov chain representation of a military aircraft flight. A Scenario Based S-MPC leverages the scenario trees to optimize the expected value of the cost function while enforcing constraints over all potential pathways. This strategy was demonstrated through simulation perform comparably to an MPC given exact knowledge of the future references and outperform an MPC given no preview.

To conclude, this dissertation developed advanced predictive control strategies for the engine and power subsystems of an MEA. In the process of this work, the following key contributions were made: 1) Development of models for simulation of the engine and electrical distribution of an MEA. 2) Rate-based MPC is able to achieve offset free tracking of references in the MEA with a linear prediction model. 3) Coordination of the subsystems, even when distributed, is able to improve engine thrust tracking. 4) Preview of changes in the power load dampens the voltage deviations from fast power transients in the MEA.

6.2 Future Work

There are many potential avenues for expanding upon control strategies for MEA systems, some thoughts are given below.

6.2.1 Distributed Control

This work considered control for two subsystems, adding additional subsystems to the MT and DMT D-MPCs would be of interest. One potential subsystem would be thermal management which would increase the spread in the system dynamics time constants. Additionally, filtering the interacting variables to the engine time scale was able to reduce the communication volume required to reach a consensus however, more formal considerations for impediments to coordination such as delays or dropped packets in communications may be necessary for hardware implementation.

6.2.2 Stochastic Control

A path planner considering long-term dynamics over a mission such as fuel or battery level would enable greater flexibility in how many many targets could be approached by an MEA. The assumption of static transitions during each target encounter should be replaced with a transition map that evolves in response to the progression of the mission. Additionally, distributing control of the MEA with stochastic reference scenarios could be done using contract based methods to avoid forcing the subsystems to consider the same number of scenarios.

6.2.3 Alternative Power Architectures

The microgrid architecture considered was hybrid source by the generators and the battery pack. Explorations of the impact in variations of the subsystem architecture and how it can be managed would be of interest. For example, using ultra capacitors in the place of the battery back would provide faster reacting energy storage at the cost of lower capacity. Management of multiple cascading voltage buses would add in additionally complexity to the electrical subsystem and how it must be managed.

6.2.4 Alternative Propulsion Architectures

Concept aircraft propulsion architectures such as gas and electric hybrid designs have been proposed for improving fuel efficiency in commercial aviation [51, 48, 49]. Such an architecture would require another point of coordination between the engine and power subsystems as thrust satisfaction can be distributed, possibly the gas and electric thrusters operate at differing time constants and could be used similarly to how the generators and energy storage are used to satisfy power demands..

6.2.5 Hardware Testing

These control methods were all tested on simulated representations of the MEA. Applying these methods to hardware test beds or small UAVs would be the next step in progressing these controllers into real-world applications. This would require further studies on the computational effort required for the strategies and how that could be reduced without impacting performance, such as with MPC specific solvers.

APPENDIX A

MEA Model Parameters

A.1 Detailed Model

A.1.1 JT9D Parameters

The JT9D engine was simulated using NASA's T-MATS example [61]. The Simulink toolbox is open source and the parameters of the engine can be found there.

Table A.1: Parameters for the Engine Subsystem.

Variable	Description	Value	Variable	Description	Value
h_{alt}	Altitude	22,000 ft	MN	Mach Number	0.5
$\Delta\bar{u}_{FAR}$	FAR Step constraint	0.225/s	$\Delta\underline{u}_{FAR}$	FAR Step constraint	-0.225/s
$c_{HP,SM}$	HP Surge Constraint	15%	$c_{LP,SM}$	LP Surge Constraint	20%

A.1.2 Microgrid Parameters

The battery pack of the electrical micro grid is modeled off the XALT Energy's 63 Ah High Power Superior Lithium Ion Cells, information can be found at [63].

Table A.2: Parameters for the Electrical Subsystem.

Variable	Description	Value	Variable	Description	Value
Ω_L	CPL Resistance	0.8 Ohms	N_{Batt}	# of Battery Cells	1
$\Delta\bar{u}_{PL}$	CPL Step Lim	$\pm$1,500 A/s	$\Delta\bar{u}_{Batt}$	Batt Step Lim	-0.225/s
$\Delta\bar{u}_{sp}$	Split Step Lim	$\pm$ 20/s	$\Delta\bar{u}_{V}$	Bus Step Lim	25,00 V/s
$\bar{u}_{sp}$	Split Upper-Lim	0.8	$\underline{u}_{sp}$	Split Lower-Lim	0.2
$\bar{u}_{Batt}$	Batt Upper-Lim	25 A	$\underline{u}_{Batt}$	Batt Lower-Lim	-25 A

A.2 Simple Model

A.2.1 AGTF30 Parameters

The AGTF30 model is as was presented in [69], more specific details on the engine can be found there.

Table A.3: Parameters for the Engine Subsystem.

Variable	Description	Value	Variable	Description	Value
h_{alt}	Altitude	15,000 ft	MN	Mach Number	0.6
$\Delta\bar{u}_{Wf}$	Wf Step Lim	$\pm$ 0.04 lb/s^2	$\Delta\bar{u}_{VAFN}$	VAFN Step Lim	$\pm$ 100ft^2/s
$\Delta\bar{u}_{VBV}$	VBV Step Lim	$\pm$ 10%/s	$\bar{u}_{WF}$	WF Upper	0.8 pps
$\underline{u}_{Wf}$	Wf Lower	0.1 pps	$\bar{u}_{VBV}$	VBV Upper	100%
$\underline{u}_{VBV}$	VBV Lower	0%			
$c_{HP,SM}$	HP SM Cons	10%	$c_{LP,SM}$	LP SM Cons	15%

A.2.2 Electrical Powerflow Parameters

Table A.4: Parameters for the Electrical Subsystem.

Variable	Description	Value	Variable	Description	Value
Ω_L	CPL Resistance	0.25 Ohms	C_{Bus}	Bus Capacitance	0.01 W/V
α_{Gen}	Power Flow	25W/V	β_{Gen}	Power Flow	-22W/V
η_{Gen}	Gen Eff	0.8	β_{Gen}	Power Flow	-22W/V
$\Delta\bar{u}_{PL}$	CPL Step Lim	$\pm$1000 kW/s	$\Delta\bar{u}_{V}$	Bus Step Lim	5 V/s
$\Delta\bar{u}_{sp}$	Split Step Lim	$\pm$ 0.1/s			
$\bar{u}_{sp}$	Split Upper-Lim	0.9	$\underline{u}_{sp}$	Split Lower-Lim	0.1
$\bar{u}_{Batt}$	Batt Upper-Lim	25 A	$\underline{u}_{Batt}$	Batt Lower-Lim	-25 A

APPENDIX B

Linear Models

B.1 Simplified Model

The linearization of the Simplified model was found by a combination of a perturbation method of the engine done by a T-MATS tool [61], filter fittings of the electrical dynamics, and analytical differentiation for the torques.

The linearized engine model state dynamics, discretized at time-steps of 0.1 seconds, is found to be

$$A_e = \begin{bmatrix} 0.7774 & 0.0956 \\ 0.0832 & 0.7435 \end{bmatrix}, \; B_e = \begin{bmatrix} 397.70 & 0.04 & 17.24 \\ 693.69 & -0.005 & -154.43 \end{bmatrix}, \; W_{ep} = \begin{bmatrix} -0.02 & -0.04 \\ -0.33 & 0 \end{bmatrix}, \tag{B.1}$$

where the states are ordered as $x_e = [\omega_{LP},\ \omega_{HP}]^T$, the inputs as $u_e = [u_{Wf},\ u_{VAFN},\ u_{VBV}]^T$, and the interactions as $x_{ep} = [\tau_{HP},\ \tau_{LP}]^T$. The output matrices are

$$C_e = \begin{bmatrix} 2.94 & 0.02 \\ -0.017 & 0.025 \\ 0.008 & 0.005 \end{bmatrix}, \quad D_e = \begin{bmatrix} 611 & -1 & -5 \\ -1.48 & 0 & 63.6 \\ -55.7 & 0 & -7.8 \end{bmatrix}, \tag{B.2}$$

where the outputs are $y_e = [y_{thr},\ y_{SM,LP},\ y_{SM,HP}]^T$. The interactions out are $x_{pe} = [\omega_{LP},\ \omega_{HP}]^T$ and the associated matrices are

$$E_{pe} = \begin{bmatrix} 1 & 0 \\ 0 & 1 \end{bmatrix}, \quad F_{pe} = \mathbf{0}. \tag{B.3}$$

The continuous linearized dynamics

$$A_p = \begin{bmatrix} 0 & 1 & 0 & -1 \\ -260 & -260 & 1 & 0 \\ 0 & 0 & -10 & 0 \\ 0 & 0 & 0 & -2500 \end{bmatrix}, \; B_p = \begin{bmatrix} 0 & 0 & 0 & 0 \\ -1 & 0 & 0 & 0 \\ 10 & 0 & 0 & 0 \\ 0 & 0 & 0 & 1 \end{bmatrix}, \; W_{pe} = \begin{bmatrix} 0 & 0 \\ 0 & 0 \\ 0 & 0 \\ 2 & 0.5 \end{bmatrix}, \tag{B.4}$$

where the states in order are the deviation of the voltage from the reference, a filter state for the voltage impact by the power load, the power load, and a filter state for the voltage impact by the batteries and shaft speeds, $x_p = [x_V,\ x_{V,PL},\ x_{PL},\ x_{V,Other}]^T$. The inputs in order are $u_p = [u_{pl},\ u_V,\ u_{sp},\ u_{Batt}]$. The outputs in order are $y_p = [y_{HVDC},\ y_{PL}]^T$, and are found with the output matrices

$$C_p = \begin{bmatrix} 1 & 0 & 0 & 1 \\ 0 & 0 & 1 & 0 \end{bmatrix}, \quad D_p = \begin{bmatrix} 0 & 1 & 0 & 0 \\ 0 & 0 & 0 & 0 \end{bmatrix}. \tag{B.5}$$

The interactions out are found with the following matrices

$$E_{ep} = \begin{bmatrix} 0 & 0 & u^*_{sp}/(\eta_{gen}\omega^*_{HP}) & 0 & 0 \\ 0 & 0 & (1-u^*_{sp})/(\eta_{gen}\omega^*_{LP}) & 0 & 0 \end{bmatrix}, \tag{B.6}$$

$$F_{ep} = \begin{bmatrix} 0 & -u^*_{sp}/(\eta_{gen}\omega^*_{HP}) & (u^*_{PL}-u^*_{Batt})/(\eta_{gen}\omega^*_{HP}) & -u^*_{sp}/(\eta_{gen}\omega^*_{HP}) \\ 0 & -(1-u^*_{sp})/(\eta_{gen}\omega^*_{LP}) & -(u^*_{PL}-u^*_{Batt})/(\eta_{gen}\omega^*_{LP}) & -(1-u^*_{sp})/(\eta_{gen}\omega^*_{LP}) \end{bmatrix}.$$

The states and inputs with the '*' superscript are initialized as current value at each controller initialization and held constant over the horizon.

B.2 Detailed Model

The dynamics for the Detailed model were found using the system identification toolbox in Matlab. As a result, the states have no physical meaning. The engine input is $u_e = u_{FAR}$, the outputs are $y_e = [y_{SM,HP}\ y_{SM,LP}\ y_{thr}]^T$, the interactions in are $x_{ep} = [\tau_{HP}\ \tau_{LP}]^T$, and the interactions out are $x_{pe} = [\omega_{HP}\ \omega_{LP}]^T$. The discrete-time engine matrices are

$$A_e = \begin{bmatrix} 0.6680 & 0.0033 & 0.0012 & 0.0009 \\ 0.0062 & 0.6728 & 0.0080 & -0.0070 \\ 0.0034 & -0.0499 & 0.5654 & 0.0303 \\ 0.0008 & -0.0051 & 0.2005 & 0.6296 \end{bmatrix}, \; B_e = \begin{bmatrix} -0.0142 \\ -0.1515 \\ 1.1447 \\ -0.7152 \end{bmatrix}, \tag{B.7}$$

$$W_{ep} = \begin{bmatrix} 0.0000 & -0.0000 \\ -0.0001 & -0.0000 \\ 0.0015 & 0.0001 \\ -0.0014 & -0.0001 \end{bmatrix}, \tag{B.8}$$

the output matrices for the engine are

$$C_e = \begin{bmatrix} 4.7050 & 3.7905 & 0.1250 & -0.0662 \\ -3.3874 & 7.5683 & 0.3089 & -0.0031 \\ -177.4216 & -681.3870 & 4.5136 & 15.2496 \end{bmatrix}, \; D_e = \begin{bmatrix} -0.5491 \\ 0.6863 \\ 556.3 \end{bmatrix}, \tag{B.9}$$

and interaction matrices out are,

$$E_{pe} = \begin{bmatrix} 15.7277 & -72.0692 & -3.0642 & 0.2990 \\ -40.0239 & -31.9874 & -1.0237 & 0.1156 \end{bmatrix}, \; F_{pe} = \begin{bmatrix} -4.2572 \\ 4.7706 \end{bmatrix}. \tag{B.10}$$

The inputs for the power model are $u_p = [u_V \; u_{sp} \; u_{Batt} \; u_P L]^T$ and the outputs are $y_p = [y_{PL} \; y_{HVDC}]^T$. The linear matrices for the power model are

$$A_p = \begin{bmatrix} 0.8332 & -0.3126 & -0.1289 & -0.0228 & 0.2213 \\ 0.1393 & 0.8114 & -0.2443 & -0.0127 & 0.1519 \\ -0.2796 & -0.1459 & 0.2447 & 0.0176 & 0.0519 \\ 0.0281 & 1.1809 & -0.2042 & 0.5571 & -0.7273 \\ -0.0875 & -0.0937 & -0.4931 & 0.0574 & 0.1336 \end{bmatrix}, \tag{B.11}$$

$$B_p = \begin{bmatrix} -0.0987 & -0.1682 & -0.0017 & 0.0303 \\ -0.0663 & -0.1999 & 0.0021 & -0.0321 \\ -0.0736 & -1.5712 & -0.0024 & -0.0271 \\ -0.7975 & -2.5134 & -0.0070 & 1.0411 \\ 0.4574 & -1.8154 & 0.0065 & -0.0975 \end{bmatrix}, \tag{B.12}$$

$$W_{pe} = \begin{bmatrix} 0.0524 & -0.0936 \\ 0.0177 & -0.0319 \\ -0.0409 & 0.0732 \\ -0.3103 & 0.5586 \\ -0.2812 & 0.5035 \end{bmatrix}, \tag{B.13}$$

$$C_p = \begin{bmatrix} 0 & 0 & 0 & 0 & 0 \\ -4.0991 & 15.4287 & -2.6614 & 0.3093 & 0.4798 \end{bmatrix}, \tag{B.14}$$

$$D_p = \begin{bmatrix} 0 & 0 & 0 & 10 \\ 0 & 0 & 0 & 0 \end{bmatrix}, \tag{B.15}$$

$$E_{ep} = 1000 * \begin{bmatrix} 1.2649 & -0.8672 & -1.2231 & 0.0563 & 0.3982 \\ 4.5726 & -0.6001 & -0.3866 & 0.0641 & 0.5901 \end{bmatrix}, \; F_{ep} = \mathbf{0}. \tag{B.16}$$

BIBLIOGRAPHY

[1] ANSYS, "Electrifying the Aviation Industry," *Dimensions Magazine*, 2018.

[2] Roboam, X., Sareni, B., and De Andrade, A., "More electricity in the air: Toward optimized electrical networks embedded in more-electrical aircraft," *IEEE industrial electronics magazine*, Vol. 6, No. 4, 2012, pp. 6–17.

[3] Behrendt, M., "A basic working principle of Model Predictive Control," Creative Commons License.

[4] Maldonado, M. A., Shah, N. M., Cleek, K. J., Walia, P. S., and Korba, G., "Power management and distribution system for a more-electric aircraft (MADMEL)-program status," *Energy Conversion Engineering Conference, 1996. IECEC 96., Proceedings of the 31st Intersociety*, Vol. 1, IEEE, 1996, pp. 148–153.

[5] Rosero, J., Ortega, J., Aldabas, E., and Romeral, L., "Moving towards a more electric aircraft," *IEEE Aerospace and Electronic Systems Magazine*, Vol. 22, No. 3, 2007, pp. 3–9.

[6] Emadi, K. and Ehsani, M., "Aircraft power systems: technology, state of the art, and future trends," *IEEE Aerospace and Electronic Systems Magazine*, Vol. 15, No. 1, 2000, pp. 28–32.

[7] Iden, S. M., Sehmbey, M. S., and Borger, D. P., "MW class power system integration in aircraft," Tech. rep., SAE Technical Paper, 2004.

[8] Stills, D., "AFRL Commander Describes Air Force's Technology Vision," *Air Force News*, 2014.

[9] Leuschen, C. J., Swift, R. N., Comiso, J. C., Raney, R. K., Chapman, R. D., Krabill, W. B., and Sonntag, J. G., "Combination of laser and radar altimeter height measurements to estimate snow depth during the 2004 Antarctic AMSR-E Sea Ice field campaign," *Journal of Geophysical Research: Oceans*, Vol. 113, No. C4, 2008.

[10] Cook, J. C., "Proposed monocycle-pulse very-high-frequency radar for air-borne ice and snow measurement," *Transactions of the American Institute of Electrical Engineers, Part I: Communication and Electronics*, Vol. 79, No. 5, 1960, pp. 588–594.

[11] Croke, S. and Herrenschmidt, J., "More electric initiative-power-by-wire actuation alternatives," *Aerospace and Electronics Conference, 1994. NAECON 1994., Proceedings of the IEEE 1994 National*, IEEE, 1994, pp. 1338–1346.

[12] Quigley, R., "More electric aircraft," *Applied Power Electronics Conference and Exposition, 1993. APEC'93. Conference Proceedings 1993., Eighth Annual*, IEEE, 1993, pp. 906–911.

[13] Dunham, W., Hencey, B., Kolmanovsky, I., and Girard, A., "Predictive propulsion and power control for large transient power loads in a More Electric Aircraft," *American Control Conference (ACC), 2017*, IEEE, 2017, pp. 4055–4061.

[14] Corbett, M., Lamm, P., McNichols, J., Boyd, M., and Wolff, M., "Effects of transient power extraction on an integrated hardware-in-the-loop aircraft/propulsion/power system," Tech. rep., SAE Technical Paper, 2008.

[15] Sarlioglu, B. and Morris, C. T., "More electric aircraft: Review, challenges, and opportunities for commercial transport aircraft," *IEEE Transactions on Transportation Electrification*, Vol. 1, No. 1, 2015, pp. 54–64.

[16] Belkhayat, M., Cooley, R., and Witulski, A., "Large signal stability criteria for distributed systems with constant power loads," *Power Electronics Specialists Conference, 1995. PESC'95 Record., 26th Annual IEEE*, Vol. 2, IEEE, 1995, pp. 1333–1338.

[17] Sudhoff, S. D., Glover, S. F., Lamm, P. T., Schmucker, D. H., and Delisle, D., "Admittance space stability analysis of power electronic systems," *IEEE Transactions on Aerospace and Electronic Systems*, Vol. 36, No. 3, 2000, pp. 965–973.

[18] Larky, A., "Negative-impedance converters," *IRE Transactions on Circuit Theory*, Vol. 4, No. 3, 1957, pp. 124–131.

[19] Gries, M., Wasynczuk, O., Selby, B., and Lamm, P. T., "Designing for large-displacement stability in aircraft power systems," *SAE International Journal of Aerospace*, Vol. 1, No. 2008-01-2867, 2008, pp. 894–902.

[20] Herrera, L. C. and Tsao, B.-H., "Analysis and control of energy storage in aircraft power systems with pulsed power loads," *SAE International Journal of Aerospace*, Vol. 9, No. 2016-01-1981, 2016, pp. 8–13.

[21] Emadi, A., Khaligh, A., Rivetta, C. H., and Williamson, G. A., "Constant power loads and negative impedance instability in automotive systems: definition, modeling, stability, and control of power electronic converters and motor drives," *IEEE Transactions on vehicular technology*, Vol. 55, No. 4, 2006, pp. 1112–1125.

[22] Walters, E., Amrhein, M., O'Connell, T., Iden, S., Lamm, P., Yerkes, K., Wolff, M., McCarthy, K., Raczkowski, B., Wells, J., et al., "INVENT modeling, simulation, analysis and optimization," *48th AIAA Aerospace Sciences Meeting Including the New Horizons Forum and Aerospace Exposition*, 2010, p. 287.

[23] Doerry, N. H. and Davis, J. C., "Integrated power system for marine applications," *Naval Engineers Journal*, Vol. 106, No. 3, 1994, pp. 77–90.

[24] McCoy, T. J., "Trends in ship electric propulsion," *Power Engineering Society Summer Meeting, 2002 IEEE*, Vol. 1, IEEE, 2002, pp. 343–346.

[25] Seenumani, G., Sun, J., and Peng, H., "Real-time power management of integrated power systems in all electric ships leveraging multi time scale property," *IEEE Transactions on Control Systems Technology*, Vol. 20, No. 1, 2012, pp. 232–240.

[26] Cupelli, M., Ponci, F., Sulligoi, G., Vicenzutti, A., Edrington, C. S., El-Mezyani, T., and Monti, A., "Power flow control and network stability in an all-electric ship," *Proceedings of the IEEE*, Vol. 103, No. 12, 2015, pp. 2355–2380.

[27] Geertsma, R., Negenborn, R., Visser, K., and Hopman, J., "Design and control of hybrid power and propulsion systems for smart ships: A review of developments," *Applied Energy*, Vol. 194, 2017, pp. 30–54.

[28] Khaligh, A., Li, Z., et al., "Battery, ultracapacitor, fuel cell, and hybrid energy storage systems for electric, hybrid electric, fuel cell, and plug-in hybrid electric vehicles: State of the art," *IEEE transactions on Vehicular Technology*, Vol. 59, No. 6, 2010, pp. 2806–2814.

[29] Boulanger, A. G., Chu, A. C., Maxx, S., and Waltz, D. L., "Vehicle electrification: Status and issues," *Proceedings of the IEEE*, Vol. 99, No. 6, 2011, pp. 1116–1138.

[30] Bilgin, B., Magne, P., Malysz, P., Yang, Y., Pantelic, V., Preindl, M., Korobkine, A., Jiang, W., Lawford, M., and Emadi, A., "Making the case for electrified transportation," *IEEE Transactions on Transportation Electrification*, Vol. 1, No. 1, 2015, pp. 4–17.

[31] Koeln, J. P. and Alleyne, A. G., "Stability of decentralized model predictive control of graph-based power flow systems via passivity," *Automatica*, Vol. 82, 2017, pp. 29–34.

[32] Pangborn, H. C., Koeln, J. P., and Alleyne, A. G., "Passivity and Decentralized MPC of Switched Graph-Based Power Flow Systems," *2018 Annual American Control Conference (ACC)*, IEEE, 2018, pp. 198–203.

[33] Koeln, J. P., Williams, M. A., and Alleyne, A. G., "Hierarchical Control of Multi-Domain Power Flow in Mobile Systems: Part IFramework Development and Demonstration," *ASME 2015 Dynamic Systems and Control Conference*, American Society of Mechanical Engineers, 2015, pp. V001T08A006–V001T08A006.

[34] Williams, M. A., Koeln, J. P., and Alleyne, A. G., "Hierarchical Control of Multi-Domain Power Flow in Mobile Systems: Part IIAircraft Application," *ASME 2015 Dynamic Systems and Control Conference*, American Society of Mechanical Engineers, 2015, pp. V001T08A005–V001T08A005.

[35] Seok, J., Kolmanovsky, I., and Girard, A., "Coordinated model predictive control of aircraft gas turbine engine and power system," *Journal of Guidance, Control, and Dynamics*, Vol. 40, No. 10, 2017, pp. 2538–2555.

[36] Griggs, S. C., Iden, S. M., and Lamm, P. T., "Energy Optimized Aircraft: What is it and how do we make one?" *SAE International Journal of Aerospace*, Vol. 5, No. 2012-01-2179, 2012, pp. 415–424.

[37] United States Air Force, *U.S. Air Force Energy Flight Plan 2017-2036*, 2017.

[38] O'Connell, T. C., McCarthy, K., Yeu, R., Pigg, P., Bowman, T., and Lamm, P., "Software tools for efficient model-based design of energy optimized aircraft," *SAE International Journal of Aerospace*, Vol. 5, No. 2012-01-2176, 2012, pp. 386–397.

[39] O'Connell, T. C., McCarthy, K., Paquette, A., McCormick, D., Pigg, P., and Lamm, P. T., "Enhancements to Software Tools and Progress in Model-Based Design of EOA on the INVENT Program," Tech. rep., SAE Technical Paper, 2014.

[40] Geiss, I. and John, P., "Directed Energy Weapons on the Battlefield: A new vision for 2025," Tech. rep., AIR WAR COLL MAXWELL AFB AL, 2003.

[41] Doman, D. B., "Optimal Cruise Altitude for Aircraft Thermal Management," *Journal of Guidance, Control, and Dynamics*, Vol. 38, No. 11, 2015, pp. 2084–2095.

[42] Doman, D. B., "Fuel Flow Topology and Control for Extending Aircraft Thermal Endurance," *Journal of Thermophysics and Heat Transfer*, Vol. 32, No. 1, 2017, pp. 35–50.

[43] Herrera, L., Palmer, B., Yao, X., and Tsao, B.-H., "Controller design of DC microgrids with multiple sources and constant power loads," *Energy Conversion Congress and Exposition (ECCE), 2017 IEEE*, IEEE, 2017, pp. 2625–2630.

[44] Behbahani, A., Culley, D., Carpenter, S., Mailander, B., Hegwood, B., Smith, B., Darouse, C., Mahoney, T., Quinn, R., Battestin, G., et al., "Status, vision, and challenges of an intelligent distributed engine control architecture," Tech. rep., SAE Technical Paper, 2007.

[45] Yedavalli, R. K., Belapurkar, R. K., and Behbahani, A., "Design of distributed engine control systems for stability under communication packet dropouts," *Journal of guidance, control, and dynamics*, Vol. 32, No. 5, 2009, pp. 1544–1549.

[46] Raczkowski, B. C., Loop, B., Amrhein, M., Wells, J., Walters, E., Wasynczuk, O., Field, S., and Lamm, P., "Large Displacement Stability by Design for Robust Aircraft Electric Power Systems," Tech. rep., SAE Technical Paper, 2012.

[47] Shin, J., "NASA Aeronautics: Strategic Implementation Plan," , No. NASA NP-2017-01-2352-HQ, 2017. doi:10.1057/9781137294678. 0652.

[48] Papathakis, K. V., Kloesel, K. J., Lin, Y., Clarke, S., Ediger, J. J., and Ginn, S., "Design and development of a 200-kw turbo-electric distributed propulsion testbed," 2016.

[49] Stoll, A. M. and Veble Mikic, G., "Design studies of thin-haul commuter aircraft with distributed electric propulsion," *16th AIAA Aviation Technology, Integration, and Operations Conference*, 2016, p. 3765.

[50] Welstead, J. and Felder, J. L., "Conceptual design of a single-aisle turboelectric commercial transport with fuselage boundary layer ingestion," *54th AIAA Aerospace Sciences Meeting*, 2016, p. 1027.

[51] Connolly, J. W., Chapman, J. W., Stalcup, E. J., Chicatelli, A., and Hunker, K. R., "Modeling and Control Design for a Turboelectric Single Aisle Aircraft Propulsion System," *2018 AIAA/IEEE Electric Aircraft Technologies Symposium*, 2018, p. 5010.

[52] Dyson, R. W., "NASA Electric Aircraft Test Bed (NEAT) Development Plan-Design, Fabrication, Installation," 2016.

[53] Madavan, N., Heidmann, J., Bowman, C., Kascak, P., Jankovsky, A., and Jansen, R., "A NASAperspective on electric propulsion technologies for commercial aviation," *Proceedings of the Workshop on Technology Roadmap for Large Electric Machines, Urbana-Champaign, IL, USA*, 2016, pp. 5–6.

[54] Wells, J. R., Amrhein, M., Walters, E., Iden, S., Page, A., Lamm, P., and Matasso, A., "Electrical accumulator unit for the energy optimized aircraft," *SAE International Journal of Aerospace*, Vol. 1, No. 2008-01-2927, 2008, pp. 1071–1077.

[55] Motapon, S. N., Dessaint, L.-A., and Al-Haddad, K., "A comparative study of energy management schemes for a fuel-cell hybrid emergency power system of more-electric aircraft," *IEEE Transactions on Industrial Electronics*, Vol. 61, No. 3, 2014, pp. 1320–1334.

[56] Todd, R., Wu, D., dos Santos Girio, J., Poucand, M., and Forsyth, A., "Supercapacitor-based energy management for future aircraft systems," *Applied Power Electronics Conference and Exposition (APEC), 2010 Twenty-Fifth Annual IEEE*, IEEE, 2010, pp. 1306–1312.

[57] Dunham, W., Hencey, B., Girard, A., and Kolmanovsky, I., "Distributed MPC via ADMM for Coordination and Control of More Electric Aircraft Subsystems," *ASME 2017 Dynamic Systems and Control Conference*, American Society of Mechanical Engineers, 2017, pp. V002T14A007–V002T14A007.

[58] Dunham, W., Hencey, B., Kolmanovsky, I., and Girard, A., "Distributed Model Predictive Control for More Electric Aircraft Subsystems Operating at Multiple Time Scales," *IEEE Transactions on Control Systems Technology*, Submitted June 2018.

[59] Pratt & Whitney, "Pratt & Whitney's JT9D," http://www.pw.utc.com/products-and-services/products/commercial-engines/JT9D-Engine/. Retrieved December 2018.

[60] Chapman, J. W., Lavelle, T. M., Litt, J. S., and Guo, T.-H., "A Process for the Creation of T-MATS Propulsion System Models from NPSS data," *50th AIAA/ASME/SAE/ASEE Joint Propulsion Conference*, 2014, p. 3931.

[61] Chapman, J. W., Lavelle, T. M., May, R. D., Litt, J. S., and Guo, T.-H., "Toolbox for the Modeling and Analysis of Thermodynamic Systems (T-MATS) User's Guide," 2014.

[62] Jones, S. M., "An Introduction to Thermodynamic Performance Analysis of Aircraft Gas Turbine Engine Cycles Using the Numerical Propulsion System Simulation Code," 2007.

[63] XALT Energy, *XALT 63 Ah High Power (HP) Superior Lithium Ion Cell*, 1 2015, Ver. 3.

[64] Davoudi, A., Jatskevich, J., and Rybel, T., "Numerical state-space average-value modeling of PWM DC-DC converters operating in DCM and CCM," *IEEE TRANSACTIONS ON POWER ELECTRONICS PE*, Vol. 21, No. 4, 2006, pp. 1003.

[65] Krause, P. and Associates, I., "ASMG for Simulink Release Notes," 2015.

[66] Johnson, V. H., Pesaran, A. A., and Sack, T., *Temperature-dependent battery models for high-power lithium-ion batteries*, National Renewable Energy Laboratory City of Golden, 2001.

[67] Krause, P. C., Wasynczuk, O., Sudhoff, S. D., and Pekarek, S., *Analysis of electric machinery and drive systems*, Vol. 75, John Wiley & Sons, 2013.

[68] United States Armed Forces, *MIL-STD-704F Aircraft Electric Power Characteristics*, 10 2013, Ver. F.

[69] Chapman, J. W. and Litt, J. S., "Control Design for an Advanced Geared Turbofan Engine," *53rd AIAA/SAE/ASEE Joint Propulsion Conference*, 2017, p. 4820.

[70] Andersson, G., "Dynamics and control of electric power systems," *Lecture notes*, 2012, pp. 227–0528.

[71] Williams, M. A., Koeln, J. P., Pangborn, H. C., and Alleyne, A. G., "Dynamical Graph Models of Aircraft Electrical, Thermal, and Turbomachinery Components," *Journal of Dynamic Systems, Measurement, and Control*, Vol. 140, No. 4, 2018, pp. 041013.

[72] Perez, H. E., Siegel, J. B., Lin, X., Stefanopoulou, A. G., Ding, Y., and Castanier, M. P., "Parameterization and validation of an integrated electro-thermal cylindrical lfp battery model," *ASME 2012 5th Annual Dynamic Systems and Control Conference joint with the JSME 2012 11th Motion and Vibration Conference*, American Society of Mechanical Engineers, 2012, pp. 41–50.

[73] Rawlings, J. B. and Mayne, D. Q., "Model predictive control: Theory and design," 2009.

[74] Pannocchia, G., Gabiccini, M., and Artoni, A., "Offset-free MPC explained: novelties, subtleties, and applications," *IFAC-PapersOnLine*, Vol. 48, No. 23, 2015, pp. 342–351.

[75] Morari, M. and Maeder, U., "Nonlinear offset-free model predictive control," *Automatica*, Vol. 48, No. 9, 2012, pp. 2059–2067.

[76] Maeder, U. and Morari, M., "Offset-free reference tracking with model predictive control," *Automatica*, Vol. 46, No. 9, 2010, pp. 1469–1476.

[77] Pannocchia, G., "Offset-free tracking MPC: A tutorial review and comparison of different formulations," *Control Conference (ECC), 2015 European*, IEEE, 2015, pp. 527–532.

[78] Pannocchia, G. and Bemporad, A., "Combined design of disturbance model and observer for offset-free model predictive control," *IEEE Transactions on Automatic Control*, Vol. 52, No. 6, 2007, pp. 1048–1053.

[79] Pannocchia, G. and Rawlings, J. B., "Disturbance models for offset-free model-predictive control," *AIChE journal*, Vol. 49, No. 2, 2003, pp. 426–437.

[80] Mayne, D. Q., Rawlings, J. B., Rao, C. V., and Scokaert, P. O., "Constrained model predictive control: Stability and optimality," *Automatica*, Vol. 36, No. 6, 2000, pp. 789–814.

[81] Huang, M., "Low Complexity Model Predictive Control of a Diesel Engine Airpath." *The University of Michigan*, 2016, Thesis.

[82] Huang, M., Zaseck, K., Butts, K., and Kolmanovsky, I., "Rate-based model predictive controller for diesel engine air path: Design and experimental evaluation," *IEEE Transactions on Control Systems Technology*, Vol. 24, No. 6, 2016, pp. 1922–1935.

[83] Seok, J., Kolmanovsky, I., and Girard, A., "Integrated/coordinated control of aircraft gas turbine engine and electrical power system: Towards large electrical load handling," *Decision and Control (CDC), 2016 IEEE 55th Conference on*, IEEE, 2016, pp. 3183–3189.

[84] Grimm, G., Messina, M. J., Tuna, S. E., and Teel, A. R., "Model predictive control: for want of a local control Lyapunov function, all is not lost," *IEEE Transactions on Automatic Control*, Vol. 50, No. 5, 2005, pp. 546–558.

[85] Scattolini, R., "Architectures for distributed and hierarchical model predictive control–a review," *Journal of Process Control*, Vol. 19, No. 5, 2009, pp. 723–731.

[86] Maestre, J. M., Negenborn, R. R., et al., *Distributed model predictive control made easy*, Vol. 69, Springer, 2014.

[87] Christofides, P. D., Scattolini, R., de la Pena, D. M., and Liu, J., "Distributed model predictive control: A tutorial review and future research directions," *Computers & Chemical Engineering*, Vol. 51, 2013, pp. 21–41.

[88] Venkat, A. N., Hiskens, I. A., Rawlings, J. B., and Wright, S. J., "Distributed MPC strategies with application to power system automatic generation control," *IEEE transactions on control systems technology*, Vol. 16, No. 6, 2008, pp. 1192–1206.

[89] Stewart, B. T., Venkat, A. N., Rawlings, J. B., Wright, S. J., and Pannocchia, G., "Cooperative distributed model predictive control," *Systems & Control Letters*, Vol. 59, No. 8, 2010, pp. 460–469.

[90] Blasi, S., Kögel, M., and Findeisen, R., "Distributed Model Predictive Control Using Cooperative Contract Options," *IFAC-PapersOnLine*, Vol. 51, No. 20, 2018, pp. 448–454.

[91] Culley, D. E. and Behbahani, A., "Communication needs assessment for distributed turbine engine control," *NASA, Technical Manual TM-2008-215419, Glenn Research Center, Cleveland, Ohio*, 2008.

[92] Seitz, T., Yedavalli, R., Macmann, O., and Behbahani, A., "Robust Control of Turbine Engines Using Distributed Networks with Multiple Time Delays," *Journal of Guidance, Control, and Dynamics*, 2017, pp. 1–11.

[93] Kokotovic, P., Khalil, H. K., and O'reilly, J., *Singular perturbation methods in control: analysis and design*, Vol. 25, Siam, 1999.

[94] Zhang, Y., Naidu, D. S., Cai, C., and Zou, Y., "Singular Perturbation and time scales in control theories and applications: an overview 2002–2012," *Int. J. Inf. Syst. Sci*, Vol. 9, No. 1, 2014, pp. 1–36.

[95] Chen, X., Heidarinejad, M., Liu, J., and Christofides, P. D., "Composite fast-slow MPC design for nonlinear singularly perturbed systems," *AIChE Journal*, Vol. 58, No. 6, 2012, pp. 1802–1811.

[96] Wogrin, M. and Glielmo, L., "An MPC scheme with guaranteed stability for linear singularly perturbed systems," *Decision and Control (CDC), 2010 49th IEEE Conference on*, IEEE, 2010, pp. 5289–5295.

[97] Tippett, M. J., Tan, C. K., and Bao, J., "Non-Constant Prediction-Step MPC for Processes with Multi-Scale Dynamics," *IFAC Proceedings Volumes*, Vol. 47, No. 3, 2014, pp. 3068–3073.

[98] Boyd, S., Parikh, N., Chu, E., Peleato, B., and Eckstein, J., "Distributed optimization and statistical learning via the alternating direction method of multipliers," *Foundations and Trends® in Machine Learning*, Vol. 3, No. 1, 2011, pp. 1–122.

[99] Farokhi, F., Shames, I., and Johansson, K. H., "Distributed MPC via dual decomposition and alternative direction method of multipliers," *Distributed Model Predictive Control Made Easy*, Springer, 2014, pp. 115–131.

[100] Le Ny, J. and Pappas, G. J., "Differentially private filtering," *IEEE Transactions on Automatic Control*, Vol. 59, No. 2, 2014, pp. 341–354.

[101] Koponen, T., Casado, M., Gude, N., Stribling, J., Poutievski, L., Zhu, M., Ramanathan, R., Iwata, Y., Inoue, H., Hama, T., et al., "Onix: A distributed control platform for large-scale production networks." *OSDI*, Vol. 10, 2010, pp. 1–6.

[102] Themelis, A., Stella, L., and Patrinos, P., "Douglas-Rachford splitting and ADMM for nonconvex optimization: new convergence results and accelerated versions," *arXiv preprint arXiv:1709.05747*, 2017.

[103] Eckstein, J. and Bertsekas, D. P., "On the DouglasRachford splitting method and the proximal point algorithm for maximal monotone operators," *Mathematical Programming*, Vol. 55, No. 1-3, 1992, pp. 293–318.

[104] Giselsson, P. and Boyd, S., "Linear convergence and metric selection for Douglas-Rachford splitting and ADMM," *IEEE Transactions on Automatic Control*, Vol. 62, No. 2, 2017, pp. 532–544.

[105] Liao-McPherson, D., Huang, M., and Kolmanovsky, I., "A Regularized and Smoothed Fischer-Burmeister Method for Quadratic Programming with Applications to Model Predictive Control," *IEEE Transactions on Automatic Control*, 2018.

[106] Mesbah, A., "Stochastic model predictive control: An overview and perspectives for future research," *IEEE Control Systems*, Vol. 36, No. 6, 2016, pp. 30–44.

[107] Mesbah, A., Kolmanovsky, I. V., and Di Cairano, S., "Stochastic Model Predictive Control," *Handbook of Model Predictive Control*, Springer, 2019, pp. 75–97, edited by Sasa V. Rakovic and William S. Levine. Birkhauser Basel, ISBN 978-3-319-77488-6.

[108] Scokaert, P. O. and Mayne, D., "Min-max feedback model predictive control for constrained linear systems," *IEEE Transactions on Automatic control*, Vol. 43, No. 8, 1998, pp. 1136–1142.

[109] Schwarm, A. T. and Nikolaou, M., "Chance-constrained model predictive control," *AIChE Journal*, Vol. 45, No. 8, 1999, pp. 1743–1752.

[110] Nemirovski, A. and Shapiro, A., "Convex approximations of chance constrained programs," *SIAM Journal on Optimization*, Vol. 17, No. 4, 2006, pp. 969–996.

[111] Prandini, M., Garatti, S., and Lygeros, J., "A randomized approach to stochastic model predictive control," *Decision and Control (CDC), 2012 IEEE 51st Annual Conference on*, IEEE, 2012, pp. 7315–7320.

[112] Blackmore, L., Ono, M., Bektassov, A., and Williams, B. C., "A probabilistic particle-control approximation of chance-constrained stochastic predictive control," *IEEE transactions on Robotics*, Vol. 26, No. 3, 2010, pp. 502–517.

[113] Bernardini, D. and Bemporad, A., "Scenario-based model predictive control of stochastic constrained linear systems," *Decision and Control, 2009 held jointly with the 2009 28th Chinese Control Conference. CDC/CCC 2009. Proceedings of the 48th IEEE Conference on*, IEEE, 2009, pp. 6333–6338.

[114] Di Cairano, S., Bernardini, D., Bemporad, A., and Kolmanovsky, I. V., "Stochastic MPC with learning for driver-predictive vehicle control and its application to HEV energy management." *IEEE Trans. Contr. Sys. Techn.*, Vol. 22, No. 3, 2014, pp. 1018–1031.

[115] Hull, D. G., *Fundamentals of airplane flight mechanics*, Springer, 2007.